

HIGH FIDELITY NUMERICAL SIMULATIONS OF TURBULENT JET IGNITION
AND COMBUSTION

By

AbdoulAhad Validi

A DISSERTATION

Submitted to
Michigan State University
in partial fulfillment of the requirements
for the degree of

Mechanical Engineering - Doctor of Philosophy

2016

ABSTRACT

HIGH FIDELITY NUMERICAL SIMULATIONS OF TURBULENT JET IGNITION AND COMBUSTION

By

AbdoulAhad Validi

Turbulent jet ignition (TJI) is a novel ignition enhancement method, which facilitates the combustion of lean and ultra-lean mixtures in complex propulsion systems and engines. Here, a comprehensive study of TJI in different combustion systems is conducted with direct numerical simulation (DNS) and large eddy simulation (LES) methods.

DNS of TJI-assisted combustion of lean hydrogen-air is performed in a three-dimensional planar jet configuration for various thermo-chemical and flow conditions. Fully compressible gas dynamics and species equations are solved with high order finite difference methods and a detailed chemical kinetics mechanism. Several interesting phenomena involved in TJI-assisted combustion including localized flame extinction/reignition and simultaneous premixed-diffusion flames are investigated by considering flow/combustion variables like the heat release, temperature, species concentrations, vorticity, Baroclinic torque, and a newly defined TJI progress variable.

Numerical simulations of TJI-assisted combustion in a rapid compression machine (RCM) are also conducted by a hybrid Eulerian-Lagrangian LES method based on the filtered mass density function (FMDF) model. An immersed boundary method is developed and used in the LES to facilitate morphing the complex geometries and decrease the Monte Carlo (MC) particle search and locate operations in FMDF. It also helps to properly handle finite difference grids and MC particles at the boundaries while maintaining the high accuracy of the simulator. In the TJI-RCM system, a hot product turbulent jet rapidly propagates

from a pre-chamber (PCh) to a main chamber (MCh). Three main combustion phases of TJI-assisted combustion in a RCM are delineated as i) cold fuel jet, ii) turbulent hot product jet, and iii) reverse fuel-air/product jet. The effects of various parameters on these phases are studied numerically, including the igniter timing and location, lean/rich/ N_2 -diluted mixtures, and adiabatic vs. non-adiabatic walls.

It is found that the turbulent jet characteristics and the MCh combustion are highly affected by the PCh turbulence intensity as well as the ignition parameters. For example, igniting the PCh at the lower locations close to the nozzle forces the PCh charge to fully participate in the PCh ignition/combustion processes and prevents the unburned fuels leaking to the MCh. It also enhances the MCh combustion by generating lower velocity hot product jets for a longer time. The pressure traces predicted by LES/FMDF are found to be in good comparison with the available experimental data. The temperature contours are also well comparable with the experiments.

To my parents
Parvin and Ahmad

ACKNOWLEDGMENTS

I am sincerely grateful to my advisor Professor Farhad Jaber for his invaluable guidance and support. This work would not have been successful without his patience and encouragement. It has been truly an honor and an enlightening experience working for him.

My sincere thanks go to my doctoral committee members Dr. Harold Schock, Dr. Carl Lira, and Dr. Elisa Toulson for their constructive comments. Dr. Toulson's insights on rapid compression machines were very helpful.

This study was conducted with the support of National Science Foundation and Department of Energy under grant number CBET-1258581. I express my gratitude to the Institute for Cyber-Enabled Research High Performance Computing Center staff at Michigan State University for their support in providing the computational facilities for this study. Technical help from Dr. Dirk Colbry, Jim Leikert, and Andrew Keen is greatly appreciated. I would also like to acknowledge the Texas Advanced Computing Center (TACC) at The University of Texas at Austin for providing a part of computational resources for this study through XSEDE program.

Last but not the least, I am ever-indebted to my parents and my two sisters for their unconditional love, support, and sacrifice behind everything I have achieved in life, including this dissertation.

TABLE OF CONTENTS

LIST OF TABLES	viii
LIST OF FIGURES	ix
KEY TO SYMBOLS AND ABBREVIATIONS	xvi
 Chapter 1 Fundamental Study of Turbulent Jet Ignition and Combustion in a Lean Premixed Configuration with DNS	 1
1.1 Chapter summary	1
1.2 Introduction	2
1.3 Governing equations and numerical methodology	6
1.4 Flow configuration	9
1.5 Results and discussions: flow and flame features of TJI-assisted combustion .	14
1.5.1 Flow-flame structure	16
1.5.2 Turbulent flame speed	32
1.5.3 Temporal and spatial variations of turbulent variables	34
1.6 Results and discussions: jet and coflow effects on development of premixed and non-premixed flames including localized extinction in TJI-assisted combustion	48
1.6.1 Flame variable for TJI-assisted	55
1.6.2 Coflow composition effects	59
1.6.3 Incoming jet thermo-chemical effects	74
1.7 Chapter conclusions	79
 Chapter 2 LES/FMDF of Turbulent Jet Ignition assisted Rapid Com- pression Machines	 82
2.1 Chapter summary	82
2.2 Introduction	83
2.3 Governing equations	87
2.3.1 Filtered compressible Navier-Stokes equations	87
2.3.2 Compressible single phase scalar FMDF equations	91
2.3.3 Numerical approach	96
2.3.4 MC particle tracking and parallelization	98
2.3.5 Immersed boundary method for LES/FMDF	99
2.4 TJI-RCM setup and computational domain	100
2.5 Results and discussions	103
2.5.1 Compression stage	103
2.5.2 Combustion phase	108
2.5.2.1 Comparison with experiment and parametric analysis	116
2.6 Chapter conclusions	142

BIBLIOGRAPHY	144
------------------------	-----

LIST OF TABLES

Table 1.1:	Thermo-chemical properties of the incoming jets and coflows.	11
Table 1.2:	The species mass fractions in the incoming jets.	11
Table 1.3:	Detailed chemistry model for H_2/O_2 system.	12
Table 2.1:	Specifications of TJI-assisted RCM computational domain.	102
Table 2.2:	Igniter parameters used in experiment and energy deposition model (EDM).	109
Table 2.3:	Thermo-chemical and physical parameters of simulated TJI-assisted RCM.	116

LIST OF FIGURES

Figure 1.1:	Schematic of turbulent jet ignition of turbulent plane jet, TJI-TPJ, configuration.	10
Figure 1.2:	The grid resolution at the flame front, identified based on ϕ_H , and a magnified view of the flame front by a factor of 26 : 1.	13
Figure 1.3:	Instantaneous contours of the temperature at a middle spanwise plane, ($z = 1.5 \times D$), at different times during flow transition from a non-reacting flow to a reacting one. ($\tau_{ig} = 3\tau_0$)	15
Figure 1.4:	Instantaneous heat release rate contour after $17\tau_0$. (Contours presented in the lower figures are for the $y = 0.5 \times D$ plane (Surf _{xz} in figure 1.1)	17
Figure 1.5:	Various zones in the developed region of the simulated turbulent planar jet with turbulent jet ignition.	19
Figure 1.6:	Marginal PDFs of (a) Temperature and (b) H radical mass fraction. (c) Scatter plot of H radical mass fraction and temperature.	20
Figure 1.7:	Instantaneous Temperature contours for: (a) Non-reacting and (b) Reacting cases after 17 flow through time, τ_0	23
Figure 1.8:	Instantaneous (a) OH and (b) H concentration contours for reacting flow at $t = 17\tau_0$	24
Figure 1.9:	Scatter plots of \dot{Q}_e , ϕ_H , and ϕ_{OH} , an illustration of the spatial correlation between heat release rate and (a) OH mass fraction and (b) H mass fraction	25
Figure 1.10:	Normalized species mass fractions versus ζ at (a) $\xi = 4$ and (b) $\xi = 16$	27
Figure 1.11:	Conditional joint and marginal PDFs. (a) Conditional joint PDF of temperature and ϕ_H , $\mathcal{P}(T, \phi_H \mid 1000 \leq T \leq 1800)$ (b) Conditional marginal PDF of temperature, $\mathcal{P}(T \mid 4 \times 10^{-4} \leq \phi_H \leq 6 \times 10^{-4})$	28
Figure 1.12:	Instantaneous vorticity magnitude, ω , contours for (a) Non-reacting and (b) Reacting cases at $t = 17\tau_0$	29

Figure 1.13:	Instantaneous Baroclinic torque, β contours for: (a) Non-reacting and (b) Reacting cases at $t = 17\tau_0$	31
Figure 1.14:	Marginal PDF of β , $\mathcal{P}(\phi_\beta)$	31
Figure 1.15:	Conditional means and confidence bounds of (a) Baroclinic torque, β , and (b) scalar dissipation rate of H radical.	33
Figure 1.16:	Contours of time and spanwise averaged temperature and the jet span spread rate for (a) Non-reacting and (b) Reacting cases.	35
Figure 1.17:	(a) Turbulent flame speed, S_T , and turbulence intensity, I , at flame front vs. streamwise flow direction, (b) Conditional mean and confidence bounds of turbulence intensity.	35
Figure 1.18:	(a-c) instantaneous variations of u_1 , T_1 , and ϕ_{H_1} in time; (d-f) PDF of u_1 , T_1 , and ϕ_{H_1} ; and (g) associated μ , σ , \mathcal{S} , and \mathcal{K}	37
Figure 1.19:	(a-c) instantaneous variations of u_2 , T_2 , and ϕ_{H_2} in time; (d-f) PDF of u_2 , T_2 , and ϕ_{H_2} ; and (g) associated μ , σ , \mathcal{S} , and \mathcal{K}	38
Figure 1.20:	(a-c) instantaneous variations of u_3 , T_3 , and ϕ_{H_3} in time; (d-f) PDF of u_3 , T_3 , and ϕ_{H_3} ; and (g) associated μ , σ , \mathcal{S} , and \mathcal{K}	39
Figure 1.21:	(a-c) instantaneous variations of u_4 , T_4 , and ϕ_{H_4} in time; (d-f) PDF of u_4 , T_4 , and ϕ_{H_4} ; and (g) associated μ , σ , \mathcal{S} , and \mathcal{K}	41
Figure 1.22:	(a-c) instantaneous variations of u_5 , T_5 , and ϕ_{H_5} in time; (d-f) PDF of u_5 , T_5 , and ϕ_{H_5} ; and (g) associated μ , σ , \mathcal{S} , and \mathcal{K}	42
Figure 1.23:	Streamwise variations of averaged values (a) streamwise velocity component and (b) temperature profiles at different cross-stream locations. ($\langle \cdot \rangle_s$ refers to both time and spanwise averaged value. Thick and thin lines represent the reacting and non-reacting cases, respectively)	44
Figure 1.24:	Cross-stream variations of (a) mean streamwise velocity, (b) rms of streamwise velocity, (c) mean temperature, and (d) rms of temperature. (Thick and thin lines represent the reacting and non-reacting cases, respectively)	46
Figure 1.25:	Instantaneous temperature contours at the middle spanwise plane ($z = 1.5D$) and $t = 17\tau_0$ for (a) Case1, (b) Case2, (c) Case3, (d) Case4, (e) Case5, and (f) Case6.	49

Figure 1.26:	Time and spanwise averaged temperature values, $\langle \overline{T} \rangle_s$, at (a) ξ_1 and (b) ξ_2 versus cross-stream direction, ζ , for all cases represented by (\square) Case1, (\circ) Case2, (\star) Case3, (\diamond) Case4, (\times) Case5, and (\triangleright) Case6.	52
Figure 1.27:	Mean and confidence intervals of $y-z$ plane and time averaged temperature, $\mu(\langle \overline{T} \rangle_{yz}) \pm \sigma(\langle \overline{T} \rangle_{yz})$, in the combustion zones versus streamwise direction, ξ , for all cases represented by (\square) Case1, (\circ) Case2, (\star) Case3, (\diamond) Case4, (\times) Case5, and (\triangleright) Case6.	54
Figure 1.28:	Normalized thermal half width jet by the incoming jet width, D_{half}/D , versus streamwise direction (ξ). (i) Contour of rms of temperature, T_{rms} , at the middle spanwise plane, ($z = 1.5D$), schematically shown for Case3.	55
Figure 1.29:	Mean and confidence intervals of temperature, $\mu(T) \pm \sigma(T)$, in the combustion zones at $t = 17\tau_0$ versus (a) elemental mixture fraction, f and (b) TJI combustion progress variable, \mathcal{R} , for all cases represented by (\square) Case1, (\circ) Case2, (\star) Case3, (\diamond) Case4, (\times) Case5, and (\triangleright) Case6. (i) Scatter plot of temperature, T , in the combustion zones at $t = 17\tau_0$ versus TJI combustion progress variable, \mathcal{R} , for Case6, identifying the simultaneous existence of the premixed and non-premixed combustion regimes.	58
Figure 1.30:	TJI combustion progress variable, \mathcal{R} , versus cross-stream direction at a middle spanwise plane, ($z = 1.5D$), and $t = 17\tau_0$ at (a) ξ_1 and (b) ξ_3 versus cross-stream axis, ζ , for all cases represented by (\square) Case1, (\circ) Case2, (\star) Case3, (\diamond) Case4, (\times) Case5, and (\triangleright) Case6.	59
Figure 1.31:	Instantaneous contours of the H_2O mass fraction, ϕ_{H_2O} , at a middle spanwise plane, $z = 1.5D$, and $t = 17\tau_0$ for (a) Case1, (b) Case2, (c) Case3, and (d) Case4. (Note that the scale limits are set to the available values in each contour and are not the same.)	61
Figure 1.32:	Instantaneous contours of the OH mass fraction, ϕ_{OH} , at a middle spanwise plane, $z = 1.5D$, and $t = 17\tau_0$ for (a) Case1, (b) Case2, (c) Case3, and (d) Case4.	62
Figure 1.33:	Instantaneous contours of the H mass fraction, ϕ_H , at a middle spanwise plane, $z = 1.5D$, and $t = 17\tau_0$ for (a) Case1, (b) Case2, (c) Case3, and (d) Case4. (Note that the scale limits are set to the available values in each contour and are not the same.)	63

Figure 1.34:	Instantaneous contours of the heat release rate, $\dot{Q}_e (W)$, at a middle spanwise plane, $z = 1.5D$, and $t = 17\tau_0$ for (a) Case1, (b) Case2, (c) Case3, and (d) Case4. (Note that the scale limits are set to the available values in each contour and are not the same.)	65
Figure 1.35:	Mean and confidence intervals of $y - z$ plane averaged heat release rate, $\mu(\langle \dot{Q}_e \rangle_{yz}) \pm \sigma(\langle \dot{Q}_e \rangle_{yz})$, at $t = 17\tau_0$ versus streamwise direction, ξ , for four cases represented by (\square) Case1, (\circ) Case2, (\star) Case3, and (\diamond) Case4.	66
Figure 1.36:	Localized extinction and re-ignition at flame sheet identified based on heat release and a magnified view of them by a factor of 5:1, occurred in ultra-lean coflow (Case1).	67
Figure 1.37:	Scatter plot of the heat release rate, $\dot{Q}_e (W)$, versus TJI combustion progress variable, \mathcal{R} , for (a) Case1, (b) Case2, (c) Case3, and (d) Case4 at different streamwise sections represented by (\square) Sec1, (\circ) Sec2, and (\star) Sec3.	69
Figure 1.38:	Scatter plot of the heat release rate, $\dot{Q}_e (W)$, versus strain rate, $\dot{\epsilon} (1/s)$, for (a) Case1 and (b) Case4 at different streamwise sections represented by (\square) Sec1, (\circ) Sec2, and (\star) Sec3.	71
Figure 1.39:	(a) Cross-stream location of $\max(T_{rms})$ and $\max(I)$, (b) turbulence intensity, I , values at $\max(T_{rms})$ and $\max(I)$ locations, and (c) vorticity magnitude, ω , at $\max(T_{rms})$ and $\max(I)$ locations, versus streamwise direction, ξ , for four cases represented by (\square) Case1, (\circ) Case2, (\star) Case3, and (\diamond) Case4. Thick solid and thin dashed lines correspond to $\max(T_{rms})$ and $\max(I)$, respectively.	72
Figure 1.40:	Instantaneous contours of the OH mass fraction, ϕ_{OH} , at a middle spanwise plane, $z = 1.5D$, and $t = 17\tau_0$ for (a) Case5 and (b) Case6.	75
Figure 1.41:	Instantaneous contours of the H mass fraction, ϕ_H , at a middle spanwise plane, $z = 1.5D$, and $t = 17\tau_0$ for (a) Case5 and (b) Case6. (Note that the scale limits are set to the available values in each contour and are not the same.)	76
Figure 1.42:	Instantaneous contours of the heat release rate, $\dot{Q}_e (W)$, at a middle spanwise plane, $z = 1.5D$, and $t = 17\tau_0$ for (a) Case5 and (b) Case6. (c) Mean and confidence intervals of $y - z$ plane averaged heat release rate, $\mu(\langle \dot{Q}_e \rangle_{yz}) \pm \sigma(\langle \dot{Q}_e \rangle_{yz})$, at $t = 17\tau_0$ versus streamwise direction, ξ , for three cases represented by (\star) Case3, (\times) Case5, and (\triangleright) Case6.	78

Figure 1.43:	Scatter plot of the heat release rate, \dot{Q}_e (W), versus TJI combustion progress variable, \mathcal{R} , for (a) Case5 and (b) Case6 at different streamwise sections represented by (\square) Sec1, (\circ) Sec2, and ($*$) Sec3.	79
Figure 2.1:	The attributes of the hybrid LES/FMDF model.	97
Figure 2.2:	Schematic of the grid points, large black circles; MC particles, small purple circles; control volumes, dashed green lines around the grid points; FD mesh, solid yellow line; and sweeping directions to determine i^{th} and j^{th} components of the point q .	99
Figure 2.3:	Schematic of approximated domain using IB method. Ω_{fluid} , out of domain Ω_{out} , approximated boundary (thick line), actual boundary (parallel lines), and Monte Carlo particles \bullet .	100
Figure 2.4:	(a) TJI-RCM combustion system and (b) 3D view of the TJI-RCM mesh.	102
Figure 2.5:	TJI-RCM flow structures at the end of the compression stage: (a) Contour plot of iso-surfaces of velocity magnitude, $ \vec{U} $ (m/s), and (b) Contour plot of vorticity magnitude, $ \vec{\omega} $ (1/s), in the middle of the domain at xy and xz planes.	104
Figure 2.6:	Time evolution of the PCh flow field during the compression stage considering contour plots of velocity magnitude, $ \vec{U} $ (m/s).	105
Figure 2.7:	Time evolution of the PCh flow field during the compression stage considering contour plots of vorticity magnitude, $ \vec{\omega} $ (1/s).	106
Figure 2.8:	Schematic of the wall heat transfer model and related quantities.	107
Figure 2.9:	Temperature contours of TJI-assisted RCM at the end of the compression stage, piston located at TDC, for the cases with (a) adiabatic and (b) conductive walls.	107
Figure 2.10:	Quantitative comparison of the predicted pressures of both cases using adiabatic and conductive walls with available experimental data during the compression stage of the TJI-RCM.	108
Figure 2.11:	TJI-RCM combustion phases based on the composition and direction of the flow at the nozzle.	110
Figure 2.12:	The first phase of the TJI-assisted RCM combustion stage. Instantaneous iso-surfaces of velocity magnitude colored by (a) fuel mass fraction, ϕ_{CH_4} , and (b) Temperature, T , at $t = 1.0$ (ms)	112

Figure 2.13:	The second phase of the TJI-assisted RCM combustion stage. Instantaneous iso-surfaces of velocity magnitude colored by (a) fuel mass fraction, ϕ_{CH_4} , and (b) Temperature, T , at $t = 2.5$ (ms)	113
Figure 2.14:	The reverse unburned fuel jet of the third phase of the TJI-assisted RCM combustion stage; instantaneous iso-surfaces of velocity magnitude colored by (a) fuel mass fraction, ϕ_{CH_4} , and (b) Temperature, T at $t = 4.0$ (ms). The reverse hot product jet of the third phase of the TJI-assisted RCM combustion stage; instantaneous iso-surfaces of velocity magnitude colored by (c) fuel mass fraction, ϕ_{CH_4} , and (d) Temperature, T , at $t = 8.0$ (ms).	115
Figure 2.15:	Qualitative comparison between LES/FMDF and experimental results: (a ₁)-(a ₃): Experimental pictures; (b ₁)-(b ₃): LES/FMDF span-wised averaged temperature contours at; and (c ₁)-(c ₃): LES/FMDF temperature contours in the middle of the MCh.	118
Figure 2.16:	Comparing the experimental (\diamond) and simulated pressure traces at Point _{MCh} in Case1 (\circ) and Case2 (\square).	119
Figure 2.17:	Temporal evolution of simulated temperature, T , fuel mass fraction, ϕ_{CH_4} , and velocity magnitude, $ \vec{U} $ (m/s), contours for Case1.	121
Figure 2.18:	Temporal evolution of simulated temperature, T , fuel mass fraction, ϕ_{CH_4} , and velocity magnitude, $ \vec{U} $ (m/s), contours for Case2.	122
Figure 2.19:	Temporal evolution of simulated temperature, T , fuel mass fraction, ϕ_{CH_4} , and velocity magnitude, $ \vec{U} $ (m/s), contours for Case3.	124
Figure 2.20:	Temporal evolution of simulated temperature, T , fuel mass fraction, ϕ_{CH_4} , and velocity magnitude, $ \vec{U} $ (m/s), contours for Case4.	125
Figure 2.21:	Temporal evolution of simulated temperature, T , fuel mass fraction, ϕ_{CH_4} , and velocity magnitude, $ \vec{U} $ (m/s), contours for Case5.	127
Figure 2.22:	(a) Simulated pressure traces in Pch (dashed thin lines) and Mch (solid thick lines) versus time for Case3 (\circ), Case4 (\square), and Case5 (\star). (b)-(e) Simulated temperature (blue solid lines) and fuel mass fraction (red dashed lines) at a point in the nozzle exit in the MCh side versus time for Case2 to Case5. The streamwise velocity values are also shown.	129
Figure 2.23:	Temporal evolution of simulated temperature, T , fuel mass fraction, ϕ_{CH_4} , and velocity magnitude, $ \vec{U} $ (m/s), contours for Case6.	130

Figure 2.24:	Temporal evolution of simulated temperature, T , fuel mass fraction, ϕ_{CH_4} , and velocity magnitude, $ \vec{U} $ (m/s), contours for Case7.	131
Figure 2.25:	Temporal evolution of simulated temperature, T , fuel mass fraction, ϕ_{CH_4} , and velocity magnitude, $ \vec{U} $ (m/s), contours for Case8.	132
Figure 2.26:	Temporal evolution of simulated temperature, T , fuel mass fraction, ϕ_{CH_4} , and velocity magnitude, $ \vec{U} $ (m/s), contours for Case9.	133
Figure 2.27:	(a) Simulated pressure traces in Pch (dashed thin lines) and Mch (solid thick lines) versus time for Case6 (\square), Case7 (\circ), Case8 (\star), and Case9 (\times). (b)-(e) Simulated temperature (blue solid lines) and fuel mass fraction (red dashed lines) at a point in the nozzle exit in the MCh side versus time for Case6 to Case9. The streamwise velocity values are also shown.	135
Figure 2.28:	Temporal evolution of simulated temperature, T , fuel mass fraction, ϕ_{CH_4} , and velocity magnitude, $ \vec{U} $ (m/s), contours for Case10.	136
Figure 2.29:	Temporal evolution of simulated temperature, T , fuel mass fraction, ϕ_{CH_4} , and velocity magnitude, $ \vec{U} $ (m/s), contours for Case11.	137
Figure 2.30:	Temporal evolution of simulated temperature, T , fuel mass fraction, ϕ_{CH_4} , and velocity magnitude, $ \vec{U} $ (m/s), contours for Case12.	138
Figure 2.31:	Temporal evolution of simulated temperature, T , fuel mass fraction, ϕ_{CH_4} , and velocity magnitude, $ \vec{U} $ (m/s), contours for Case13.	139
Figure 2.32:	(a) Simulated pressure traces in Pch (dashed thin lines) and Mch (solid thick lines) versus time for Case10 (\square), Case11 (\circ), Case12 (\star), and Case13 (\times). (b)-(e) Simulated temperature (blue solid lines) and fuel mass fraction (red dashed lines) at a point in the nozzle exit in the MCh side versus time for Case10 to Case13. The streamwise velocity values are also shown.	141

KEY TO SYMBOLS AND ABBREVIATIONS

Abbreviations

<i>CFD</i>	Computational fluid dynamics
<i>EDM</i>	Energy deposition model
<i>FD</i>	Finite difference
<i>FDF</i>	Filtered density function
<i>FMDF</i>	Filtered mass density function
<i>IB</i>	Immersed boundary
<i>IC</i>	Internal combustion
<i>LES</i>	Large eddy simulation
<i>MCh</i>	Main chamber
<i>PCh</i>	Pre chamber
<i>PDF</i>	Probability density function
<i>RCM</i>	Rapid compression machine
<i>rms</i>	root mean square
<i>SDE</i>	Stochastic differential equation
<i>SGS</i>	Sub-grid scale
<i>SI</i>	Spark ignition
<i>SU</i>	Service unit
<i>TJI</i>	Turbulent jet ignition
DNS	Direct numerical simulation
TJI	Turbulent jet ignition
TPJ	Turbulent plane jet

Conventions

$\bar{()}$	Time averaged value
$\langle \rangle_s$	spanwise averaged value

$\langle \rangle_L$	Conditional Favre filtered value
$\langle \rangle$	Time averaged value
$\langle \rangle_l \text{ or } -$	Filtered value
$\langle \rangle_L \text{ or } \sim$	Favre filtered value
$\langle \rangle_{l'}$	Secondary filter function
<i>Symbols</i>	
$\Delta h_{f,\alpha}^0$	Enthalpy of formation of species α , J/Kg
\dot{Q}_e	Heat release rate , J/(Kg s)
\mathcal{K}	Kurtosis
\mathcal{S}	Skewness
μ	Mean
ϕ_α	Mass fraction of species α
σ	Standard deviation
τ_0	Flow-through time, s
e_t	Total energy, J/Kg
β	Baroclinic torque magnitude, $1/s^2$
δ	Dirac delta function
Δ_G	Filter size, m
$\dot{\omega}_\alpha$	Reaction rate of species α , 1/s
\dot{Q}	Heat release rate, J/Kg.s
\dot{S}_α	Rate of mass production/destruction per unit volume for species α due to chemical reaction, Kg/s
η	Kolmogorov length, m
$\eta_t, \eta_x, \eta_y, \eta_z$	Metric coefficients of the coordinate transformation
Γ, Γ_t	Diffusion and turbulent diffusion coefficients, Kg/m.s
$\hat{F}, \hat{G}, \hat{H}$	Inviscid fluxes
$\hat{F}_v, \hat{G}_v, \hat{H}_v$	Viscous fluxes

$\kappa, \kappa_e, \kappa^*$	Thermal, effective, artificial conductivity, J/m.s.K
$ \tilde{S} $	Strain rate magnitude, 1/s
μ, μ_e, μ^*	Molecular, effective, artificial kinematic viscosity, Kg/m.s
ω	Vorticity magnitude, 1/s
Ω_m	Mixing frequency, 1/s
Φ	Composition vector
ϕ_α^+	Parabolic representations of scalar α
Ψ	Composition sample space vector
ρ	Density, Kg/m ³
σ	Fine-grained density
τ_{ij}	Viscous stress tensor
Θ_{ij}	Total stress tensor
ξ, η, ζ, τ	Independent variables in transformed domain
$\xi_t, \xi_x, \xi_y, \xi_z$	Metric coefficients of the coordinate transformation
$\zeta_t, \zeta_x, \zeta_y, \zeta_z$	Metric coefficients of the coordinate transformation
a	Speed of sound, m/s
C_m	MKEV model constant
C_ω	Mixing model constant
$C_{p\alpha}$	Specific heat of species α , J/Kg.K
D	Width of turbulent plane jet, m
E	Total internal energy, J/kg
G	Filter function
H	Total enthalpy, J/Kg
h_α	Enthalpy of species α , J/Kg
I	Turbulence intensity
J	Jacobian transformation
J_i^α	Species diffusion term, m ² /s

n	Normal direction to the immersed surface
N_s	Number of species
p	Pressure, Pa
Pr_t	Turbulent Prandtl number
q_i	Heat flux vector, Kg/s ³
R	Mixture gas constant, J/Kg.K
R^0	Universal gas constant, J/Kg.K
r_u	Velocity ratio
r_Δ	Grid size, $(\Delta_x \Delta_y \Delta_z)^{\frac{1}{3}}$
Sc	Schmidt number
T	Temperature, K
t	Time, s
U	Solution vector
u', v', w'	Fluctuations of velocity components, m/s
u_i	Velocity component in i^{th} direction, m/s
U_j	Jet velocity, m/s
U_{co}	coflow velocity, m/s
W	Wiener process, $s^{0.5}$
$w^{(n)}$	Weight of the n^{th} Monte Carlo particle
W_α	Molecular weight of species α , Kg/mole
$x, y, \text{ and } z$	streamwise, cross-stream, and spanwise directions
x_i	i^{th} component of the position vector, m
X_i^+	Probabilistic representation of position, m
\mathbf{x}	Position vector, m

Chapter 1

Fundamental Study of Turbulent Jet Ignition and Combustion in a Lean Premixed Configuration with DNS

1.1 Chapter summary

Direct numerical simulations (DNS) of turbulent jet ignition (TJI)-assisted combustion of lean premixed fuel-air mixtures are performed in a three-dimensional planar jet configuration for various thermo-chemical and flow conditions. TJI is a novel ignition enhancement method which facilitates the combustion of lean and ultra-lean mixtures by rapidly exposing them to high temperature combustion products. It is also an efficient method for initiating and controlling combustion in ultra-lean combustion systems. Fully compressible gas dynamics and species equations are solved with high order finite difference methods. The hydrogen-air reaction is simulated with a detailed chemical kinetics mechanism consisting of 9 species and 38 elementary reactions. The physical processes involved in the TJI-assisted combustion including localized premixed flame extinction and simultaneous premixed/non-premixed flames are investigated by considering the flame heat release, temperature, species concentrations, scalar dissipation, vorticity, Baroclinic torque, and a newly defined TJI progress

variable. The complex turbulent flame and flow structures are delineated in three main combustion zones as *i*) hot product jet zone, *ii*) burned-mixed zone, and *iii*) flame zone. The flow structures and statistics, temperature and species distributions, and the flame features (such as the flame speed and temperature) in the TJI-assisted combustion are found to be quite different than those in “standard” turbulent premixed combustion. The differences are mainly due to intensive interactions of the turbulence/flame with a high energy turbulent hot product jet zone.

1.2 Introduction

Turbulent jet ignition (TJI) is a novel method for initiating and controlling ultra-lean combustion in internal combustion (IC) engines [63], high-speed combustors [46], and other combustion systems [66]. TJI facilitates lean combustion by providing and propagating pockets of hot and often fuel-rich mixture products as energy and fuel sources throughout the combustor. It not only increases the efficiency and decreases the emissions but also provides more control over the entire combustion process. TJI-assisted combustion systems typically include a main chamber, a pre-chamber, and passageways to connect them. An ignition device (e.g. a spark plug) is installed in the pre-chamber to ignite the charge and create a high velocity hot product jet exiting out into the main chamber. This jet initiates and maintains the main combustion. TJI-assisted combustion of premixed mixtures have been studied in the past by several investigators, focusing on the transition and the viability of the designed configurations [15, 94, 39, 20, 22, 80]. Injecting a hot product jet into a fuel-air mixture may also be a source of strong deflagration [16] and even detonation combustion [22], which are important to the safety of the related industrial systems [28].

The ignition and combustion of premixed mixtures by turbulent jets have been studied and analyzed both numerically and experimentally in different configurations and for various fuels [15, 94, 39, 20, 22, 80]. The work of [94], for example, provides increased understanding of the influence of the jet temperature and turbulent mixing on ignition. In the study conducted by [39], the effects of jet Reynolds number and reactant diffusivity on ignition have been investigated. Generally, the main focus of these studies and other previous jet ignition studies was on the transition and the viability of the designed configurations. There is certainly a need for in-depth studies of the very complicated physical and chemical processes involved in the TJI-assisted combustion.

One of the major challenges of numerically simulating the TJI-assisted combustion is to predict different flame types (premixed, non-premixed, flamelet, distributed) at the same time. The flamelet combustion models based on G-equation [77, 78] and mixture fraction [81], each are capable of modeling either premixed or non-premixed regimes. The models based on moment closure [52] can be used in non-premixed regimes. Linear eddy [51] and scale-similarity models [43] might be better candidates for simulating different combustion regimes. However, these assumptions may be inappropriate for quantities that are dominated by small scales (e.g. chemical reactions and scalar dissipation) and therefore, high Reynolds number zones are unlikely to be resolved. The most promising modeling approaches which are capable of dealing with different combustion regimes in TJI-assisted combustion processes are the ones developed based on probability density function (pdf) methods [87] and Monte Carlo simulation techniques via the filtered density function [41]. The complexities and challenges of TJI simulations also arise from the strong coupling of the flow and thermo-chemical variables over a wide range of temporal and spatial scales, and the highly nonlinear, multicomponent, and unsteady nature of the heat and mass transport and chemical reactions

[45, 89]. An accurate and reliable numerical approach is clearly required to delineate and capture the flame and turbulence structures in such systems.

Here, for the first time, we study TJI and combustion in a well characterized three-dimensional turbulent planar jet (TPJ) [35, 32, 86, 89, 38] via direct numerical simulation (DNS). This configuration is designed such that after a sufficiently long time, the flow/combustion reaches a “stationary” condition. This unique setup makes the current work distinguishable from the previous studies in this area and attractive for fundamental investigations of TJI. The TPJ is composed of hot products of combustion of stoichiometric hydrogen-air mixture. This jet is injected into a relatively cooler lean premixed hydrogen-air coflow mixture. The flow and combustion parameters (e.g., the jet width, the streamwise, cross-stream, and spanwise domain lengths, the main jet and coflow properties, and the boundary conditions) are important factors in designing the TJI-TPJ to reach a well developed reacting condition. Both non-reacting and reacting simulations with similar flow conditions have been performed. One may have difficulty to setup the non-reacting case experimentally, because the incoming hot turbulent jet naturally ignites the premixed mixture. Nevertheless, this case provides the opportunity to isolate and study the combustion effects on the developing turbulent scalar and hydrodynamics fields. Also, the non-reacting flow results can be compared with those available in the literature for non-isothermal non-reacting jets [89, 38, 37, 86]. Our direct numerical simulations provide a wealth of data for a better understanding of various phenomena involved in TJI. These data can also be used to develop reliable models for Reynolds-average Navier-Stokes (RANS) and large eddy simulation (LES) of TJI. Here, we study the details of TJI-TPJ and investigate some of its unique features by analyzing a range of flow/combustion variables. The reacting flow is spatially divided into near-field and developed regions. In the later region, three main flow/combustion zones

are identified: *i*) remnant of the hot product jet zone, *ii*) burned-mixed zone where the products of the coflow combustion mix with the remnant of the hot jet, and *iii*) flame zone that separates the unburned coflow and burned-mixed zones. Details of the flame-turbulence structures in each zone including the associated statistics are presented in later sections.

The unique TPJ-TJI setup provides fundamental insights on the complex flame and turbulence structures in TJI-assisted combustion systems. It can be used for parametric studies of key flow/combustion parameters. Among important parameters, here, we consider the very important thermo-chemical conditions of the coflow and the incoming jet to develop insights into the temporal development of premixed/diffusion flame-turbulence interactions and various combustion zones. A wide range of coflow compositions is considered, from ultra-lean to lean mixtures with equivalence ratios of $\phi = 0.1, 0.2, 0.35$, and 0.5 . It is found that TJI is capable of initiating ultra-lean combustion by exposing the mixture, constantly and for a longer duration, to a high temperature jet. It is shown that the low flammability limit of Hydrogen-fuel mixture, $\phi = 0.14$, can be decreased more despite the existence of the localized flame extinctions. We observe an important change in flame type by changing the jet composition from the products of lean to stoichiometric, and then to rich mixtures. Even though the flame is mostly of premixed type in all simulated flows, in cases with very rich initial the mixture the generated jet includes unburned high temperature fuel, which results into the simultaneous generation of the premixed and diffusion flames. This phenomenon affects the combustion processes, significantly, by increasing overall temperature and heat release. Our understanding of TJI-assisted combustion would benefit tremendously from the DNS data and analysis provided in this study.

This chapter is organized as follows. In §1.3, the governing equations and numerical methodology are presented. In §1.4, the flow configuration is described. Section 1.5

provides detailed analysis of the flow and the temporal and spatial evolutions of various flow/combustion quantities such as heat release rate, temperature, species concentrations, vorticity, Baroclinic torque, and flame speed. In section 1.6, the effects of the coflow and incoming jet thermo-chemical properties are studied considering various flow/combustion quantities such as heat release rate, temperature, species concentrations, vorticity, and a newly defined TJI progress variable. Section 1.7 summarizes the main findings and conclusion. Section 1.7 summarizes the main findings and conclusions.

1.3 Governing equations and numerical methodology

For this DNS study, an in-house code is developed in which the conservative form of fully compressible, three-dimensional Navier-Stokes equations is solved with high order numerical methods. The governing equations include the following continuity, momentum, energy, and species equations:

$$\frac{\partial \rho}{\partial t} + \frac{\partial}{\partial x_i} (\rho u_i) = 0 \quad (i = 1, 2, 3), \quad (1.1)$$

$$\frac{\partial}{\partial t} (\rho u_i) + \frac{\partial}{\partial x_j} (\rho u_i u_j) = -\frac{\partial p}{\partial x_i} + \frac{\partial \tau_{ij}}{\partial x_j}, \quad (1.2)$$

$$\frac{\partial (\rho e_t)}{\partial t} + \frac{\partial}{\partial x_i} (\rho u_i e_t) = -\frac{\partial q_i}{\partial x_i} + \frac{\partial}{\partial x_j} (\Theta_{ij} u_i) + \dot{Q}_e + \rho \sum_{\alpha=1}^{N_s} [\phi_\alpha (u_i + u_{\alpha,i})], \quad (1.3)$$

and

$$\frac{\partial}{\partial t} (\rho \phi_\alpha) + \frac{\partial}{\partial x_i} (\rho u_i \phi_\alpha) = -\frac{\partial J_i^\alpha}{\partial x_i} + \rho \dot{S}_\alpha. \quad (1.4)$$

In equations 1.1-1.4, the primary variables are the density, ρ , the velocity component in i^{th} direction, u_i , the total energy, e_t , and the scalar mass fraction, ϕ_α , $\alpha \equiv 1, \dots, N_s$ (N_s

represents the number of species). Θ_{ij} is the total stress tensor

$$\Theta_{ij} = \tau_{ij} + p\delta_{ij}. \quad (1.5)$$

The viscous stress tensor, τ_{ij} , is obtained by the following Newtonian model:

$$\tau_{ij} = \frac{2\mu}{Re} \left[\frac{1}{2} \left(\frac{\partial u_i}{\partial x_j} + \frac{\partial u_j}{\partial x_i} \right) - \frac{1}{3} \frac{\partial u_k}{\partial x_k} \delta_{ij} \right]. \quad (1.6)$$

The heat flux vector, q_i , is obtained based on the Fourier law as

$$q_i = \frac{-\mu}{(\gamma - 1) Re Pr M_\infty^2} \frac{\partial T}{\partial x_i}, \quad (1.7)$$

and the species diffusion term

$$J_i^\alpha = \rho \phi_\alpha u_{\alpha,i}, \quad (1.8)$$

is evaluated based on the Fick's law, where $u_{\alpha,i}$ is the i^{th} component of diffusion velocity for species α . In equations 1.3 and 1.4, \dot{S}_α is the rate of mass production/destruction per unit volume for species α by chemical reaction and \dot{Q}_e represents the heat release rate calculated as

$$\dot{Q}_e = \sum_{\alpha=1}^{N_s} \dot{S}_\alpha h_\alpha. \quad (1.9)$$

The total energy and species enthalpy, h_α , are expressed as

$$e_t = \sum_{\alpha=1}^{N_s} h_\alpha \phi_\alpha - p/\rho + \frac{1}{2} u_i u_i, \quad (1.10)$$

and

$$h_\alpha = \int_{T_0}^T C_{p\alpha}(T) dT + \Delta h_{f,\alpha}^0, \quad (1.11)$$

where $C_{p\alpha}$ and $\Delta h_{f,\alpha}^0$ are the specific heat and enthalpy of formation of species α , respectively. The conservation equations are closed by the equation of state,

$$p = \rho R^0 T \sum_{\alpha=1}^{Ns} \frac{\phi_\alpha}{W_\alpha}, \quad (1.12)$$

where W_α and R^0 are the molecular weight of species α and the universal gas constant. The Chemkin thermodynamic database [49] is used to obtain species thermodynamics and transport properties. The differential diffusion effects [44] are expected to be important in the studied hydrogen flame and are included in the calculations.

The combustion of hydrogen-air is modeled with the detailed chemical kinetics mechanism developed by [102]. This mechanism, which is extensively used in several previous studies on hydrogen combustion [47, 108, 7, 13], consists of 38 elementary reactions and 9 species (H_2 , O_2 , O , OH , H_2O , H , HO_2 , H_2O_2 , and N_2). Table 1.3 shows all the forward and backward elementary reactions, not readily available in the literature. Reversed rate constants in this mechanism are computed from the forward rate and equilibrium constants.

The discretization of the governing equations is based on the compact finite difference scheme [84, 57], which yields up to eighth order spatial accuracy. In order to avoid numerical instabilities and remove the spurious high frequency fluctuations in the solutions, a low pass, high order (up to sixth order), spatial implicit filtering operator is used. The time differencing is based on the third order low storage explicit Runge Kutta method [50]. The numerical method utilized here has been used previously in DNS and LES of low speed and high speed

turbulent reacting flows [10, 3, 58, 11] and is proven to be quite accurate and suitable for the current study.

1.4 Flow configuration

The computational configuration considered in this study consists of a spatially developing, three-dimensional turbulent jet issuing hot combustion products into an ambient combustible lean premixed coflow. A schematic of the flow configuration, together with the specifications of physical dimensions are presented in figure 1.1. The flow evolves spatially in the stream-wise direction (x). The free stream boundary conditions are imposed in the cross-stream direction (y), and periodic boundary conditions are implemented in the spanwise direction (z) [84]. In the TJI-TPJ, the jet expansion is highly affected by the coflow momentum, fuel-air equivalence ratio, and turbulence-controlled flame speed. A pre-study was performed for designing a well developed reacting TJI-TPJ configuration. The TJI-TPJ flow hydrodynamics, thermo-chemical properties, and geometries have been designed such that stable combustion regions and zones are established.

Table 1.1 provides the coflow and the jet thermo-chemical properties, where T_{co} , U_{co} , $Z_{H_{co}}$, and ϕ_{co} represent the temperature, the streamwise velocity, the elemental mass fraction of H radical, and the equivalence ratio of the coflow. The equivalent variables for the incoming jet are denoted by T_j , U_j , Z_{H_j} , and ϕ_{i_j} . However, ϕ_{i_j} is the equivalence ratio of an initial hydrogen-air mixture at a temperature equals to 1000 (K), which its combustion products and temperature are assigned to the incoming jets. The species mass fraction values of the jets for all six cases are provided in table 1.2. In Case1 to Case4, the coflow compositions vary from ultra-lean to lean ($\phi_{co} = 0.1, 0.2, 0.35$, and 0.5), with the same coflow temperature

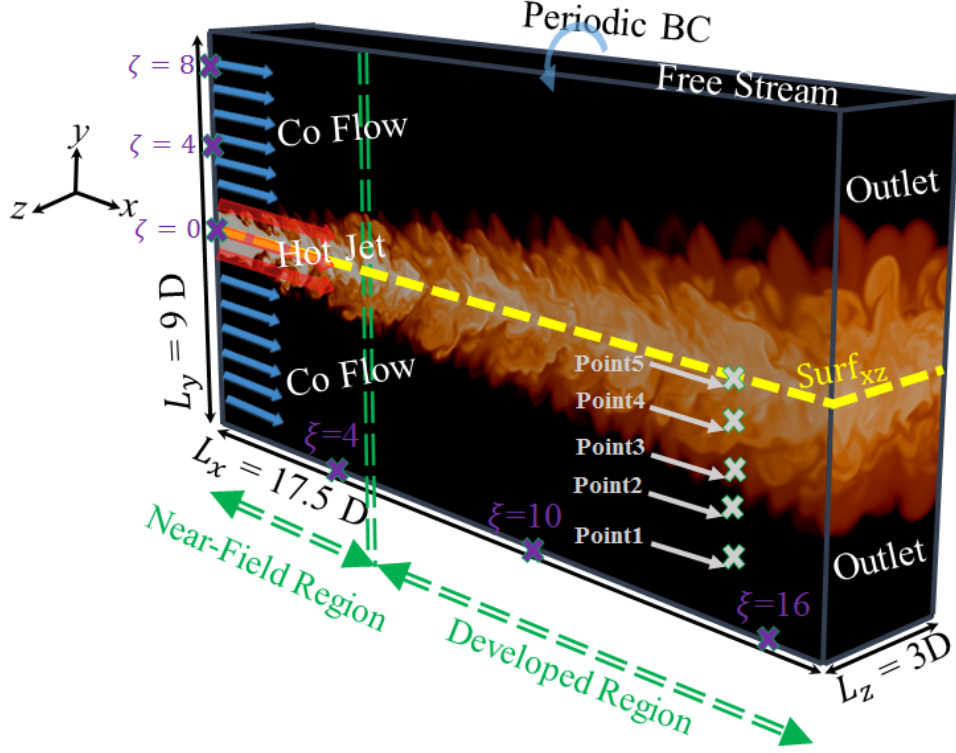


Figure 1.1: Schematic of turbulent jet ignition of turbulent plane jet, TJI-TPJ, configuration.

and velocity, $T_{co} = 850$ (K) and $U_{co} = 150$ (m/s). These cases have the same hot product jet with $\phi_{ij} = 1.0$ and $T_j = 2556.0$ (K) and can greatly help to analyze the coflow effects on the turbulence-combustion interactions. They exhibit very different flame behavior from fast burning to mixed flames with significant finite-chemistry effects and even local extinction. The effects of the jet composition or equivalence ratio (lean and rich with $\phi_{ij} = 0.5$ and 2.0) are investigated by considering Case5 and Case6. In these cases, the same coflow conditions (equivalence ratio, etc.) as Case3 are considered. Note that by changing the initial mixture equivalence ratio from 0. to 2.0, effectively the fuel concentration in the products is changed from none to significant, also the jet temperature is changed from $T_j = 2050$ to 2350 (K). In all six cases considered here, the jet velocity is set to be three times of the coflow velocity, $U_j = 3U_{co} = 450$ (m/s). In order to isolate the combustion effects, within the first three flow through time, the reaction source terms in the energy and species equations (equations 1.3

and 1.4) are turned off, so that the flow and turbulence fields become fully developed by $t = 3\tau_0$. The simulations performed up to $t = 17\tau_0$ in order to accurately calculate the time averaged statistics. The selected configuration allows the understanding of specific TJI-TPJ physical features that are believed to be invariant of the geometry and common in practical TJI-assisted combustion systems [103].

Table 1.1: Thermo-chemical properties of the incoming jets and coflows.

Case #	$T_j(K)$	$T_{co}(K)$	ϕ_{i_j}	ϕ_{co}	Z_{H_j}	$Z_{H_{co}}$
Case1	2556	850	1.0e0	1.0e-1	2.85e-2	4.03e-2
Case2	2556	850	1.0e0	2.0e-1	2.85e-2	7.74e-2
Case3	2556	850	1.0e0	3.5e-1	2.85e-2	1.28e-1
Case4	2556	850	1.0e0	5.0e-1	2.85e-2	1.73e-1
Case5	2050	850	5.0e-1	3.5e-1	1.44e-2	1.28e-1
Case6	2350	850	2.0e0	3.5e-1	5.54e-2	1.28e-1

Table 1.2: The species mass fractions in the incoming jets.

Case #	ϕ_{H_2}	ϕ_H	ϕ_{O_2}	ϕ_O	ϕ_{OH}	ϕ_{H_2O}	ϕ_{HO_2}	$\phi_{H_2O_2}$	ϕ_{N_2}
Case1-4	2.0e-7	2.1e-4	1.2e-2	1.2e-3	9.9e-3	2.2e-1	2.1e-4	3.4e-7	7.57e-1
Case5	1.9e-7	1.3e-6	1.1e-1	1.7e-4	1.8e-3	1.2e-1	1.6e-6	1.7e-7	7.55e-1
Case6	2.7e-2	3.3e-4	1.2e-5	1.5e-5	9.9e-4	2.4e-1	6.7e-9	6.8e-9	7.24e-1

The grid and time resolution in the simulations are carefully chosen to resolve all turbulent flame and flow structures. Since a detailed chemical kinetics mechanism [102] is incorporated to describe the hydrogen-air combustion, the flame structures and scalar fields are significantly complex. Therefore, a fine mesh is incorporated for capturing the flame zone as represented by intermediate radicals, e.g. H [91]. Uniform grid spacings of $\Delta_y = D/60 = 62.5 \mu m$, $\Delta_x = 1.5 \times \Delta_y$, and $\Delta_z = 1.9 \times \Delta_y$ are used in the cross-stream, streamwise, and spanwise directions, respectively. The grid points around a locally maximum H mass fraction area are shown in figure 1.2, illustrating a magnified region of the flame front. The minimum grid points covering the flame thickness (based on H radical) in the entire computational domain is found to be 9. The minimum grid number for capturing the flame zone based

Table 1.3: Detailed chemistry model for H_2/O_2 system.

No.	Mechanism		A (cm/mol/s)	Exp of T	E (kJ/mol)
1	$O_2 + H \rightleftharpoons OH + O$	k_f	2.20E14	0.00	7.03E01
		k_b	1.72E13	0.00	3.52E00
2	$H_2 + O \rightleftharpoons OH + H$	k_f	5.06E04	2.67	2.63E01
		k_b	2.22E04	2.67	1.82E01
3	$H_2 + OH \rightleftharpoons H_2O + H$	k_f	1.00E08	1.60	1.38E01
		k_b	4.31E08	1.60	7.64E01
4	$OH + OH \rightleftharpoons H_2O + O$	k_f	1.50E09	1.14	0.42E00
		k_b	1.47E10	1.14	7.10E01
5	$H + H + M \rightleftharpoons H_2 + M$	k_f	1.80E18	-1.00	0.00E00
		k_b	7.26E18	-1.00	4.36E02
6	$H + OH + M \rightleftharpoons H_2O + M$	k_f	2.20E22	-2.00	0.00E00
		k_b	3.83E23	-2.00	4.99E02
7	$O + O + M \rightleftharpoons O_2 + M$	k_f	2.90E17	-1.00	0.00E00
		k_b	6.55E18	-1.00	4.95E02
8	$H + O_2 + M \rightleftharpoons HO_2 + M$	k_f	2.30E18	-0.80	0.00E00
		k_b	3.19E18	-0.80	1.95E02
9	$HO_2 + H \rightleftharpoons OH + OH$	k_f	1.50E14	0.00	4.20E00
		k_b	1.50E13	0.00	1.70E02
10	$HO_2 + H \rightleftharpoons H_2 + O_2$	k_f	2.50E13	0.00	2.90E00
		k_b	7.27E13	0.00	2.44E02
11	$HO_2 + H \rightleftharpoons H_2O + O$	k_f	3.00E13	0.00	7.20E00
		k_b	2.95E13	0.00	2.44E02
12	$HO_2 + O \rightleftharpoons OH + O_2$	k_f	1.80E13	0.00	1.70E00
		k_b	2.30E13	0.00	2.31E02
13	$HO_2 + OH \rightleftharpoons H_2O + O_2$	k_f	6.00E13	0.00	0.00E00
		k_b	7.52E14	0.00	3.04E02
14	$HO_2 + HO_2 \rightleftharpoons 2HO_2$	k_f	2.50E11	0.00	5.20E00
		k_b	0.00E00	0.00	0.00E00
15	$OH + OH + M \rightleftharpoons H_2O_2 + M$	k_f	3.25E22	-2.00	0.00E00
		k_b	1.69E24	-2.00	2.02E02
16	$H_2O_2 + H \rightleftharpoons H_2 + O_2$	k_f	1.70E12	0.00	15.70E00
		k_b	1.32E12	0.00	83.59E00
17	$H_2O_2 + H \rightleftharpoons H_2O + OH$	k_f	1.00E13	0.00	15.00E00
		k_b	3.34E12	0.00	3.12E02
18	$H_2O_2 + OH \rightleftharpoons H_2O + HO_2$	k_f	2.80E13	0.00	26.80E00
		k_b	9.51E12	0.00	8.68E01
19	$H_2O_2 + OH \rightleftharpoons H_2O + HO_2$	k_f	5.40E12	0.00	4.20E00
		k_b	1.80E13	0.00	1.34E02

$k = A.T^n.exp(-E_a/RT)$; units: mol, cm^3 , K, and kcal.

Third-Body M is $H_2 + 6.5H_2O + 0.4O_2 + 0.4N_2 + O + OH + HO_2 + H_2O_2$.

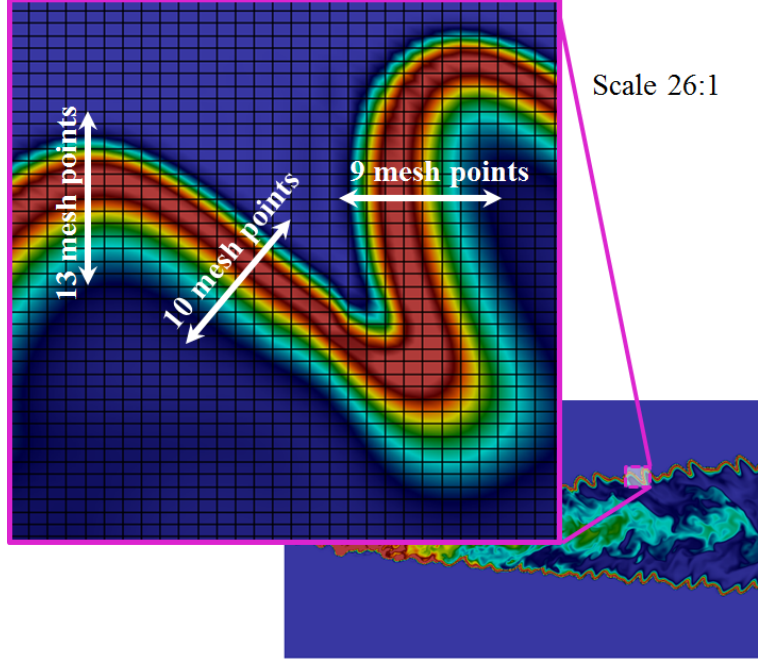


Figure 1.2: The grid resolution at the flame front, identified based on ϕ_H , and a magnified view of the flame front by a factor of 26 : 1.

on the hydroxyl radical OH is more than 15. The concentration variations of other species (not shown here) also confirms the scalar fields to be accurately computed with the adopted grids. However, to further assess the adequacy of grid resolution in different flame and turbulence zones, specially the flame zone, we have computed the local values of the Kolmogorov length scale, $\eta = \left(\frac{\nu^3}{\epsilon}\right)^{1/4}$, and found them to be lower than the grid size $\Delta = (\Delta_x \Delta_y \Delta_z)^{1/3}$. Therefore, the designed computational mesh is believed to be fine enough to accurately resolve all temporal and spatial structures of flow, turbulence, and scalars. In order to ensure the grid independence, all simulations are conducted with the highest resolution involving $820 \times 660 \times 95$ uniform grid points. The computational time increment is set to be smaller than the smallest characteristic time scales associated with the hydrodynamics and chemistry.

To produce a well developed turbulent inflow, turbulent fluctuations based on an isotropic turbulence field are added to the incoming hot product jet velocity profiles. This field

is generated by solving the governing equations with periodic boundary conditions and an initially random, solenoidal, and Gaussian velocity field for a long time [116]. The turbulence (velocity) intensity is chosen to be 10% of the hot jet velocity. To obtain temporal statistics, the simulations are advanced for a sufficiently long time, $17\tau_0$ ($\tau_0 = 218.75 \mu s$, for the average velocity of $U_{ref} = \frac{U_j + U_{co}}{2} = 300 \text{ (m/s)}$, and the streamwise domain length of $L_x = 17.5 \times D = 65.625 \times 10^{-3} \text{ (m)}$). Each simulation utilizes about 0.2 million Service Units (SU)s on 250 Intel machines at Michigan State University and University of Texas at Austin.

To produce a well developed turbulent inflow, turbulent fluctuations based on an isotropic turbulence field are added to the incoming hot product jet velocity profiles. This field is generated by solving the governing equations with periodic boundary conditions and an initially random, solenoidal, and Gaussian velocity field for a long time [116]. The turbulence intensity is chosen to be 10% of the hot jet velocity. To obtain statistics, the simulation is advanced for three flow-through time, τ_0 , before averaging the variables for a long time, $17\tau_0$ ($\tau_0 = 218.75 \mu s$, for the average velocity of $U_{ref} = \frac{U_j + U_{co}}{2} = 300 \text{ (m/s)}$, and the streamwise domain length of $L_x = 17.5 \times D = 65.625 \times 10^{-3} \text{ (m)}$). Each simulation utilizes about 0.3 million Service Units (SU)s on 250 Intel machines at Michigan State University [1] and University of Texas at Austin [2].

1.5 Results and discussions: flow and flame features of TJI-assisted combustion

In this section, the results associated with the flow hydrodynamics and thermo-chemical conditions of Case3 (shown in tables 1.2 and 1.1) for both non-reacting and reacting flows are presented and analyzed with a focus on the reacting flow. Within the first three flow

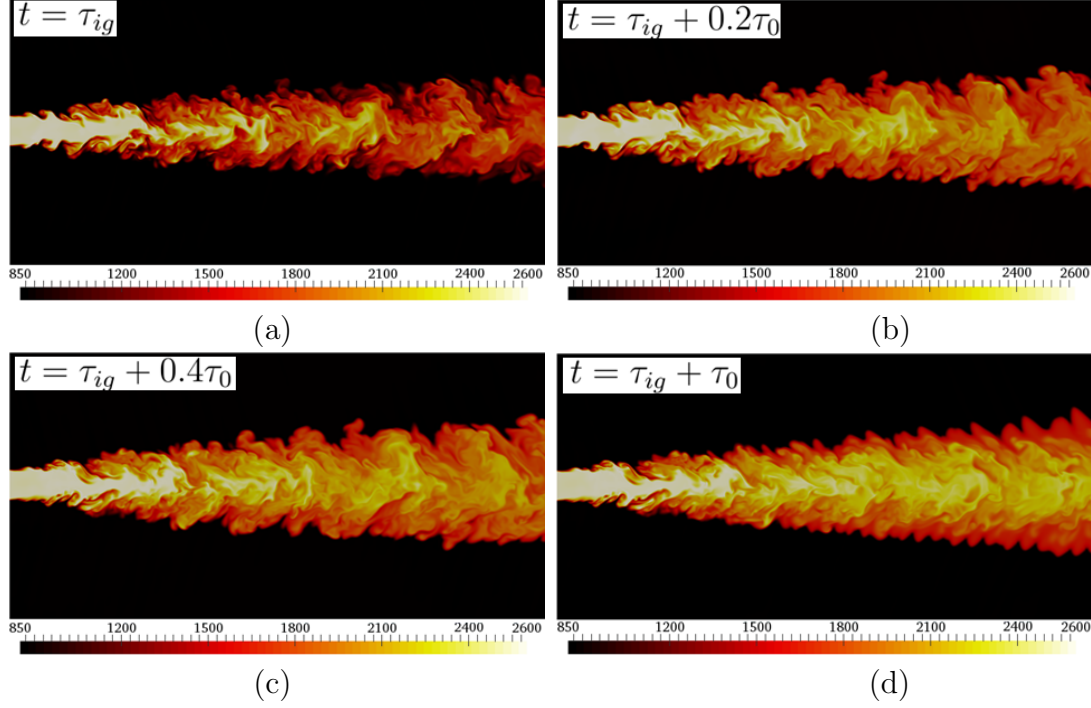


Figure 1.3: Instantaneous contours of the temperature at a middle spanwise plane, ($z = 1.5 \times D$), at different times during flow transition from a non-reacting flow to a reacting one. ($\tau_{ig} = 3\tau_0$)

through time, the reaction source terms in the energy and species equations (equations 1.3 and 1.4) are turned off, so that the flow and turbulence fields become fully developed by $t = 3\tau_0$ as seen in figure 1.3(a). The basic characteristics of isothermal and non-isothermal mixing jets for different thermo-chemical and hydrodynamics conditions have been discussed in details in previous studies [86, 83, 103, 21, 74, 92, 4, 114, 113]. Here, the non-reacting TPJ is simulated as a benchmark, providing a unique opportunity to isolate the combustion effects on the flow and turbulence. The reacting TJI-TPJ simulated in this study is the first of its kind.

1.5.1 Flow-flame structure

The flow transition from non-reacting to reacting conditions is shown in figure 1.3, where the temporal variations of the instantaneous temperature contours are considered. This transition may not be reproducible experimentally since the reaction can not be suddenly initiated from a fully developed and mixed turbulent hot product and fuel-air mixture. Figure 1.3(a) shows the already developed non-reacting jet at $t = 3\tau_0$, just before the combustion starts. Figures 1.3(b) and (c) show that, in comparison to the non-reacting jet, the reacting jet spreads much more in the cross-stream direction as the jet temperature increases by the formation of flame zones surrounding the jet edges. One of the main effects of the combustion appears to be on the relatively small flow scales. The sequence of temperature contours in figures 1.3(a)-(d) clearly shows that small-scale turbulent structures in the jet zone are gradually removed by the combustion. Yet, the turbulence wrinkles and alters the local flame structures observed to be formed in the regions surrounding the main jet (figure 1.3d). Despite their similarities to those observed in “standard” turbulent premixed flames [93], the flow and flame structures in the TJI-TPJ are significantly influenced by the existence of the hot product turbulent jet behind the flame in the burned zone.

To better describe the complex flame and turbulence fields in the TJI-TPJ, it is useful to divide the entire flow into different regions and combustion zones. Primarily, the flow is divided spatially into separate regions based on the physical flame structures, identified by the heat of reaction. The combustion heat release rate, \dot{Q}_e , is a critical quantity to discern flames and their locations in turbulent reacting flows. The spatial distribution of \dot{Q}_e is significantly dependent on the flame-turbulence interactions. Despite its significance, measuring \dot{Q}_e is a challenging task [75, 71]. Here, \dot{Q}_e is conveniently obtained by equation 1.9 [69]. Figure 1.4

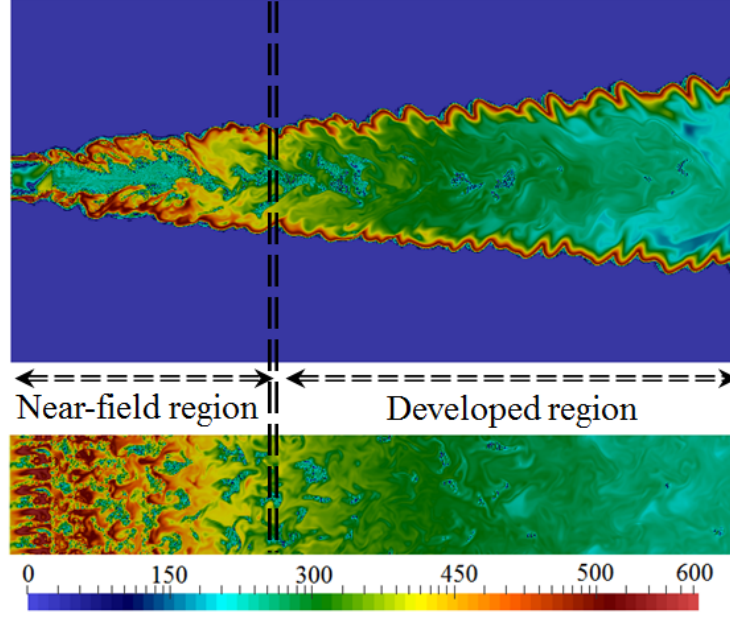


Figure 1.4: Instantaneous heat release rate contour after $17\tau_0$. (Contours presented in the lower figures are for the $y = 0.5 \times D$ plane (Surf_{xz} in figure 1.1))

shows the instantaneous contours of heat release rate at $17\tau_0$. This figure indicates that the flow field can indeed be divided into two regions in the streamwise direction: *i*) near-field ($x \leq 4D$) and *ii*) developed ($x \geq 4D$) regions with very different flame-turbulence features. In the near-field region, the hot incoming jet essentially causes autoignition at the jet shear layer and surrounding areas, where the jet heats the premixed coflow and ultimately sustains the flame in an ultra-lean fuel-air mixture. In addition to the combustion, highly distorted turbulent structures are developed in this region which enhance the mixing. The process of flame-turbulence interactions and mixing of the incoming hot jet with cooler premixed coflow in the reacting shear layer creates relatively thick and geometrically complex flames. The flame thickness is determined mainly based on the distributed \dot{Q}_e values. Marching in the streamwise direction, a spatially continuous and distorted flame is developed. While the flame moves away from the main turbulent jet and spreads in the coflow, it becomes thinner. The \dot{Q}_e contour plots in figure 1.4 clearly show the separation of the unburned and

burned zones in the developed region with the cross-stream spreading of the relatively thin distorted turbulent flame front. The lower contours in this figure show the \dot{Q}_e distribution in the spanwise direction in a $x - z$ plane at $y = D/2$. It is observed that the distributed high heat release rate values virtually vanish from the main jet as the flow move away from the near-field to the developed region. Even though the flame and turbulence features vary over time (as shown in §1.5.3), they appear to be well stabilized in the developed region.

In the developed region of the simulated TJI-TPJ, the flow can be divided into four main zones based on the flame/turbulence parameters. Figure 1.5 shows the schematic of these four zones:

- I. hot product jet zone,
- II. burned-mixed zone,
- III. flame zone, and
- IV. premixed coflow zone.

In order to identify the above zones, we primarily used the temperature, the H radical mass fraction, and the heat release rate even though other quantities such as OH mass fraction, ϕ_{OH} , vorticity, $\vec{\omega}$, and Baroclinic torque, $\vec{\beta}$, may also be used. The probability density functions (PDF)s of temperature, $\mathcal{P}(T)$, and H radical mass fraction, $\mathcal{P}(\phi_H)$, and the scatter plot of ϕ_H versus T are shown in figures 1.6(a)-(c). The PDF plots are useful in delineating the flow into different zones as shown in figure 1.5. The three distinguishable peaks of $\mathcal{P}(T)$ and $\mathcal{P}(\phi_H)$ in figures 1.6(a) and (b) are related to the three active combustion zones. The data associated with the coflow are not included in these figures. It is worthwhile to mention that details of the flow and flame may vary with changes in thermo-chemical and

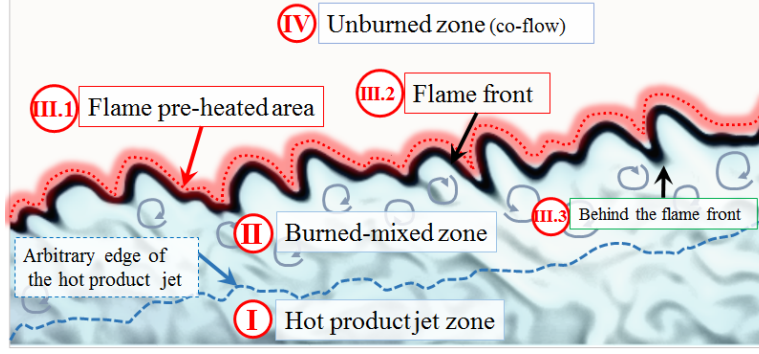


Figure 1.5: Various zones in the developed region of the simulated turbulent planar jet with turbulent jet ignition.

hydrodynamics conditions, but the general characteristics of various zones identified in the TJI-TPJ configuration stay the same.

The hot product jet zone (labeled as zone I) is identified by the $\mathcal{P}(T)$ peak located at the highest temperature values in figure 1.6(a) and by the $\mathcal{P}(\phi_H)$ peak located at the moderate ϕ_H values in figure 1.6(b). In the non-reacting flow, as expected and shown in figure 1.3(a) (and figure 1.23b), the jet temperature decreases by 30% in about $16D$ from the jet inlet due to heat transfer and mixing of hot jet with the cooler coflow. There is also a temperature reduction in the reacting jet because the flame temperature of the lean coflow mixture is considerably lower than the temperature of the hot product incoming jet. However, the temperature reduction is less than 10%, due to heating of the remnant hot product jet zone by the reaction. The initial value of ϕ_H in the hot product jet is also increased from 0.4×10^{-4} to 2.1×10^{-4} , which is consistent with the amount of H radical generated through combustion of the lean coflow mixture.

The $\mathcal{P}(T)$ peak in the intermediate temperature range in figure 1.6(a) and the $\mathcal{P}(\phi_H)$ peak in the lowest ϕ_H range in figure 1.6(b) are both associated with the burned-mixed zone, which is labeled as zone II. There is a significant interaction between turbulence and flame and, as it can be observed in the scatter plot of ϕ_H versus T in figure 1.6(c), there

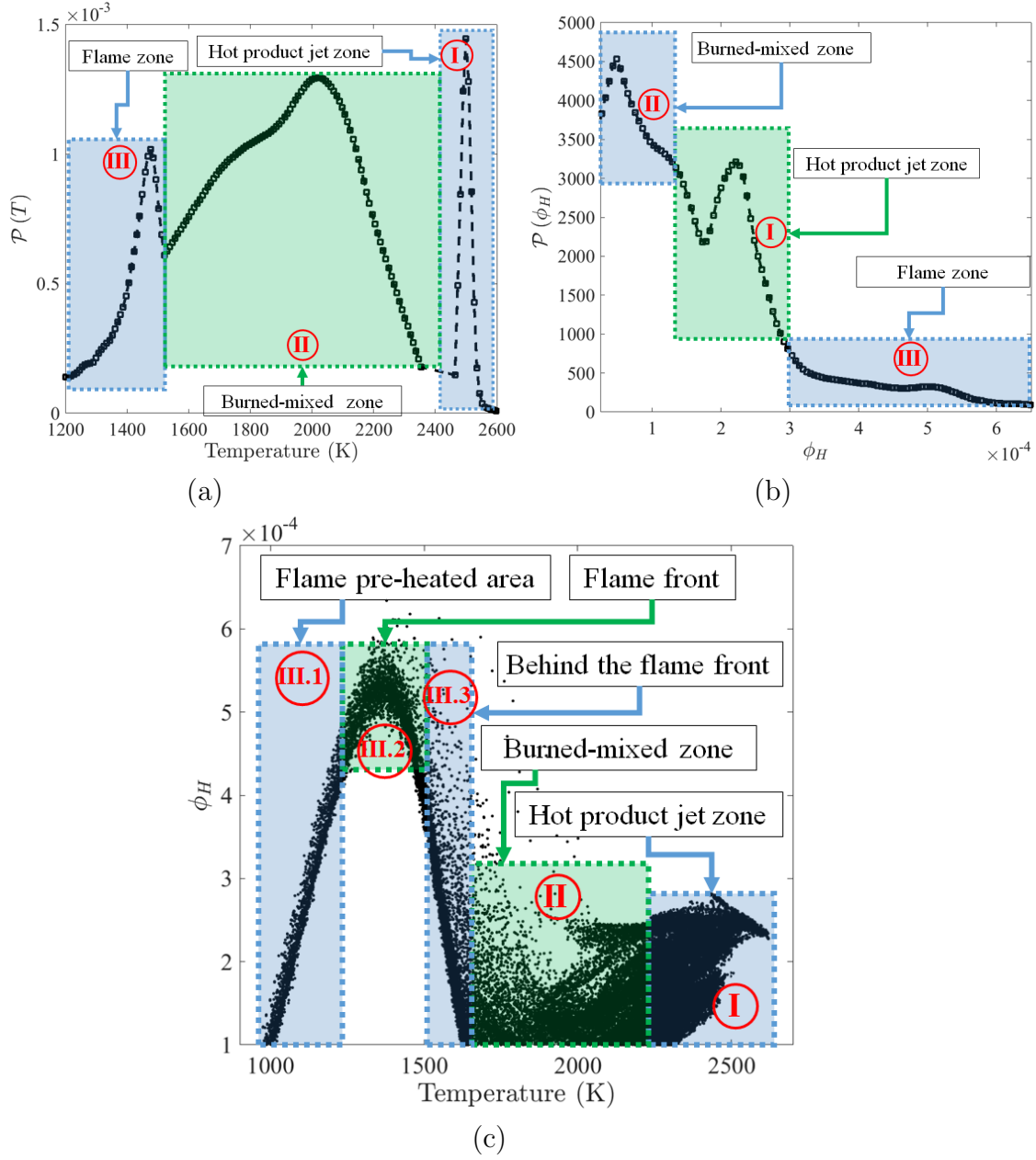


Figure 1.6: Marginal PDFs of (a) Temperature and (b) H radical mass fraction. (c) Scatter plot of H radical mass fraction and temperature.

may not be well defined and fine boundaries between zone II and its neighboring zones, particularly, the hot product jet zone. The $\mathcal{P}(T)$ peak falls in between the adiabatic flame temperature of the lean coflow and the hot product jet temperature. This clearly indicates that on average the coflow mixture is exposed to a sufficient amount of heat to initiate and sustain the combustion as zone II is significantly affected by the hot product jet. In contrast, the peak of $\mathcal{P}(\phi_H)$ occurs at the smallest ϕ_H values. As a reliable variable to identify the flame front, the maximum values of ϕ_H occur at the flame front. The ϕ_H values in the burned-mixed zone are less than their values in the hot product jet and flame front zones as the lean premixed combustion heat and products are diffused toward the main inner jet and coflow. The burned-mixed zone in the TJI-TPJ has some similarities with the burned zone appearing in standard turbulent premixed flames [88, 93, 17], but with relatively higher temperature and product species mass fraction values. The complexity of this zone arises from the strong interactions of the inner hot product jet turbulence and composition fields with the lean premixed turbulent flame.

The $\mathcal{P}(T)$ peak in the lowest temperature range or zone III of figure 1.6(a) and the $\mathcal{P}(\phi_H)$ peak in the highest ϕ_H range in figure 1.6(b) are associated with the flame temperature and ϕ_H at the flame front of combustion of lean hydrogen-air mixture (with equivalence ratio of 0.35 and initial temperature of 850 (K)). These two peaks clearly identify the flame zone. Similar to what has been suggested for standard turbulent premixed flames [23, 88, 93, 17, 14], three areas in the flame zones can be identified:

III.1) Preheated zone which is located very close to the flame front but inside the unburned fresh coflow mixture. This zone is shown in figure 1.6(c) and also in figure 1.5 by a shadow area on top of the flame front.

III.2) Flame front which is identified by the highest ϕ_H values and a relatively higher temperature than the adiabatic flame temperature of lean mixture. This zone is a thin wrinkled flame sheet separating unburned zone from the other zones as shown in figures 1.5 and 1.6(c).

III.3) Behind the flame front in burned-mixed zone which has a ϕ_H level less than that in the flame front (figure 1.6c). It is worthwhile to emphasize that the temperature and H mass fraction in area III.3 and the entire flame zone are greater than those expected for a standard turbulent premixed flame [30, 61, 33, 55, 60] because of the heat transfer and mixing with the hot product jet.

Having various combustion zones in the flow/flame fields identified, we can study the effects of combustion on these zones by examining scalar variables (like T , H_2 , OH , and H) and hydrodynamics variables (like ω , and Baroclinic torque). Figure 1.7 shows the temperature contours for both non-reacting and reacting flows at $17\tau_0$. Comparing these results to the ones presented in figure 1.3(a) and (d) confirms that the reacting flow is already well developed at $t = 4\tau_0$ and it is qualitatively similar to that shown at $t = 17\tau_0$. Our simulations are conducted for a long time to calculate the statistics. The small turbulent flow structures in non-reacting flow, as seen in figure 1.7, are virtually eliminated by the combustion. In the spanwise direction, the flow field is shown to be initially homogeneous and isotropic due to the imposed turbulent inflow. It stays homogeneous further downstream, but with considerably larger turbulent scales. Evidently, reaction causes the formation of complex combustion zones, particularly, at the shear layers and also considerable jet spreading and heating. However, the flame/turbulence structures at the flame zones are not well characterized by the temperature contours, since the incoming jet temperature is considerably higher

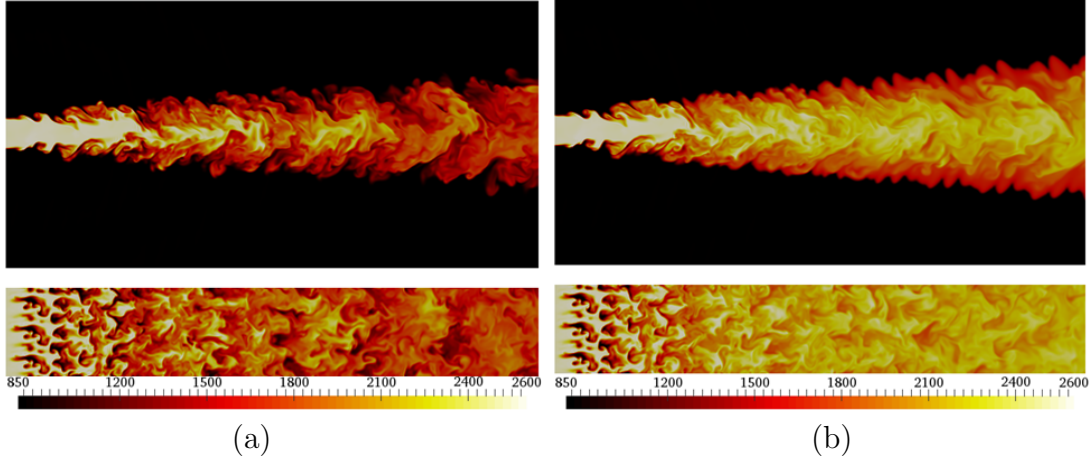


Figure 1.7: Instantaneous Temperature contours for: (a) Non-reacting and (b) Reacting cases after 17 flow through time, τ_0 .

than the adiabatic flame temperature of the lean coflow combustion.

To find suitable flame markers which correlate well with the flame and \dot{Q}_e , the spatial distributions of various species in the TJI-TPJ flow field have been examined in details. The fuel mass fraction contours (not shown here) generally represent the main reactive areas; however, more details of the flow/flame scalar fields can be obtained by considering the radical species like OH and H . As the jet composition is made of the products of stoichiometric hydrogen-air mixture combustion, the ϕ_{OH} values in the hot jet are relatively high, as opposed to that in the lean premixed coflow combustion. Naturally, in the non-reacting flow the high OH and H concentrations in the hot product jet are considerably diluted through mixing with the coflow, exhibiting qualitatively similar behavior to temperature in figure 1.7(a). In the reacting case, as shown in figure 1.8(a), the OH radical generated by the combustion (very intensively in the near-field region and less intensively in the developed region) adds up to the initial amount of OH in the jet, causing the maximum ϕ_{OH} to occur in the hot product zone and not in the flame zone. In standard premixed flames, OH radicals can identify the flame zone [64, 111, 13]. Figure 1.8(a) shows that the ϕ_{OH} values are

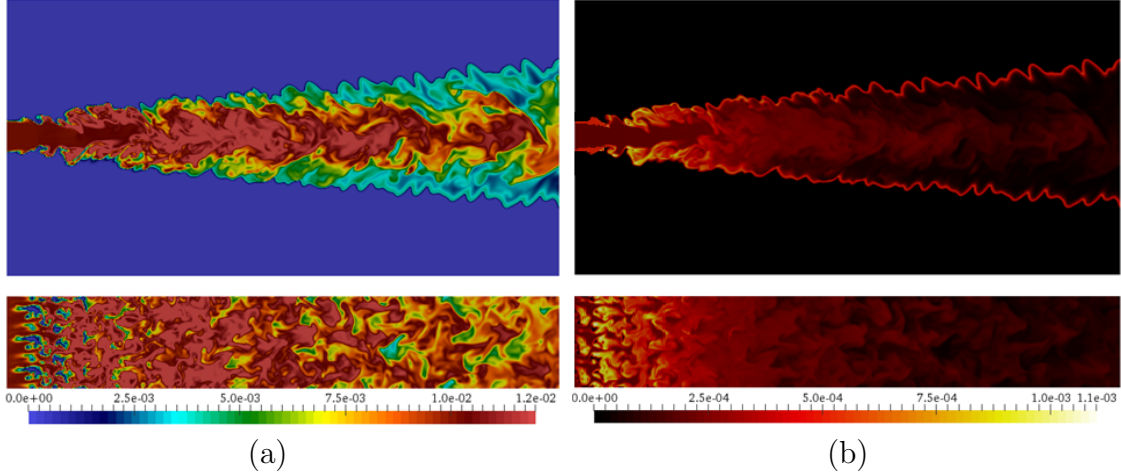


Figure 1.8: Instantaneous (a) OH and (b) H concentration contours for reacting flow at $t = 17\tau_0$.

indeed higher in the flame front than those in the immediate flame surrounding. However, since the OH concentration in the stoichiometricly-burned product jet is already significant, isolation of the flame front by ϕ_{OH} becomes somewhat difficult. In contrast to OH , the H radical level is relatively low in the hot product jet. Consequently, as shown in figure 1.8(b), ϕ_H better identifies the location of the flame front. Within the near-field region, the high values of ϕ_H initially occur at the edges of the incoming jet before spreading into the jet as shear layers develop and generate relatively thick flames. In the developed region, ϕ_H values maximize at the flame front and drop to very low values in the burned-mixed zone, consistent with the heat release rate contour plots in figure 1.4.

The scatter plot of ϕ_{OH} versus \dot{Q}_e , colored based on flow/combustion zones, in figure 1.9(a) quantifies the relationship between these two variables. Low correlation (with correlation coefficient of 0.35) between ϕ_{OH} and \dot{Q}_e indicates that the OH radical is not suitable for isolating the flame in the TJI-TPJ configuration. In contrast, the scatter plot of ϕ_H and \dot{Q}_e in figure 1.9(b) exhibits a high correlation (with correlation coefficient of 0.88) between these two quantities. In conclusion, because of relatively low ϕ_H in the product jet, H rad-

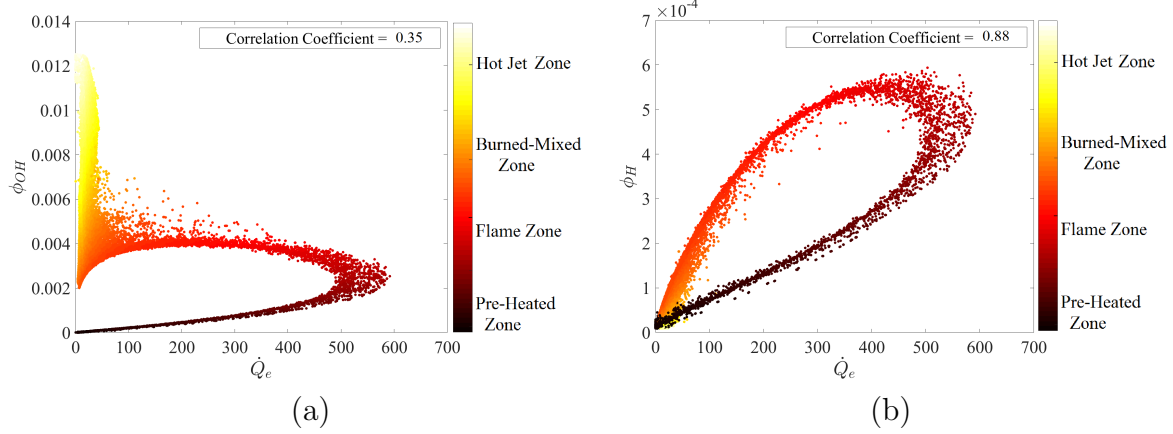


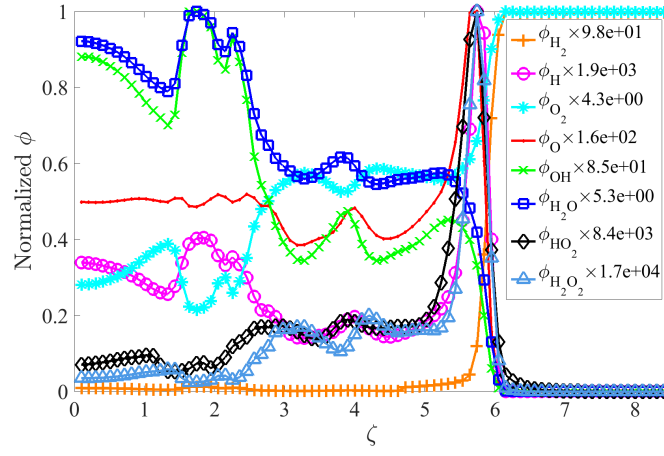
Figure 1.9: Scatter plots of \dot{Q}_e , ϕ_H , and ϕ_{OH} , an illustration of the spatial correlation between heat release rate and (a) OH mass fraction and (b) H mass fraction .

ical (and other species with similar behavior like O , HO_2 , and H_2O_2) is better representing the lean flame front in the simulated TJI-TPJ by providing clear boundaries between the unburned and burned-mixed zones. Note that figures 1.9(a) and (b) are associated with the flow in the developed region. Due to more significant interactions of flame and flow in the near-field region, the corresponding correlation coefficients are lower (0.32 for ϕ_{OH} with \dot{Q}_e and 0.84 for ϕ_H with \dot{Q}_e) in this region.

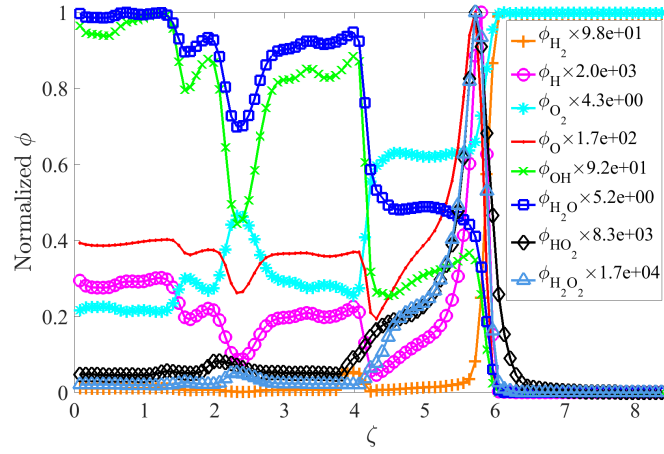
To further investigate the behavior of OH , H , and other species in the simulated TJI-TPJ configuration, the spatial distribution of all reactive species is examined. Figures 1.10(a) and (b) show the normalized species mass fractions at two streamwise locations $\xi = x/D = 4$ and 16 (shown in figure 1.1) versus the cross-stream distance from centerline, normalized by the jet half width, i.e. $\zeta = y/(D/2)$. The species mass fractions are normalized by their local maximum values. Evidently and expectedly, the reactive species follow different trends in different zones. While the fuel is completely consumed in the flame zone and has zero concentration in the burned-mixed and hot jet zones, considerable amount of O_2 is transported to and mixed with the main core jet. H and O radicals as well as HO_2 and

H_2O_2 species follow a similar trend. Their mass fraction values remain relatively small in the burned-mixed and hot jet zones and increase at the flame front at $5.5 \leq \zeta \leq 5.8$. In contrast, the OH and H_2O mass fractions maximize in the hot product jet zone and not at the flame front, where their values are not distinguishable from those in the neighboring zones. A close examination of figures 1.10(a) and (b) indicates that the H_2 , H , O_2 , O , HO_2 , and H_2O_2 mass fraction profiles at $\xi = 4$ and 16 are similar at the flame front, indicating self similar trends in the species distribution in this zone, but not necessarily at the burned-mixed and hot jet zones. The OH and H_2O profiles are quite different along these two locations, where self similarity can not be achieved for these two species in the simulated flow.

The influence of combustion on the flow variables around the flame zone is further studied by considering the conditional joint PDF of the temperature and H mass fraction in areas with $1000 \leq T \leq 1800$, $\mathcal{P}(T, \phi_H \mid 1000 \leq T \leq 1800)$, in figure 1.11(a). Similar to figure 1.6(c), a normal bell shaped profile can be observed for the joint T - ϕ_H PDF. In the areas with temperatures less than the adiabatic flame temperature (e.g., in the preheated zone very close to the flame front inside the unburned coflow) ϕ_H and T vary within the same range as they do at the flame front. However, the values of $\mathcal{P}(T, \phi_H \mid T)$ at the flame front are lower than those behind the flame front. In fact, the area behind the flame front inside the burned-mixed zone accounts for majority of the high temperature values in zone III.3 in figure 1.6(c). This confirms that the flame front is a thin zone surrounded by hot premixed mixture and products. These results are consistent with the conditional marginal PDF of temperature in the flame zone, conditioned on $4 \leq \phi_H \times 10^4 \leq 6$, in figure 1.11(b). As shown in figure 1.6(c) (zone III.2), $4 \leq \phi_H \times 10^4 \leq 6$ corresponds to the flame front. The PDF of temperature within the flame zone, $\mathcal{P}(T \mid \phi_H)$, is somewhat similar to that one normally seen in a standard lean premixed flame autoignited at 850 (K). It is close to a normal



(a)



(b)

Figure 1.10: Normalized species mass fractions versus ζ at (a) $\xi = 4$ and (b) $\xi = 16$.

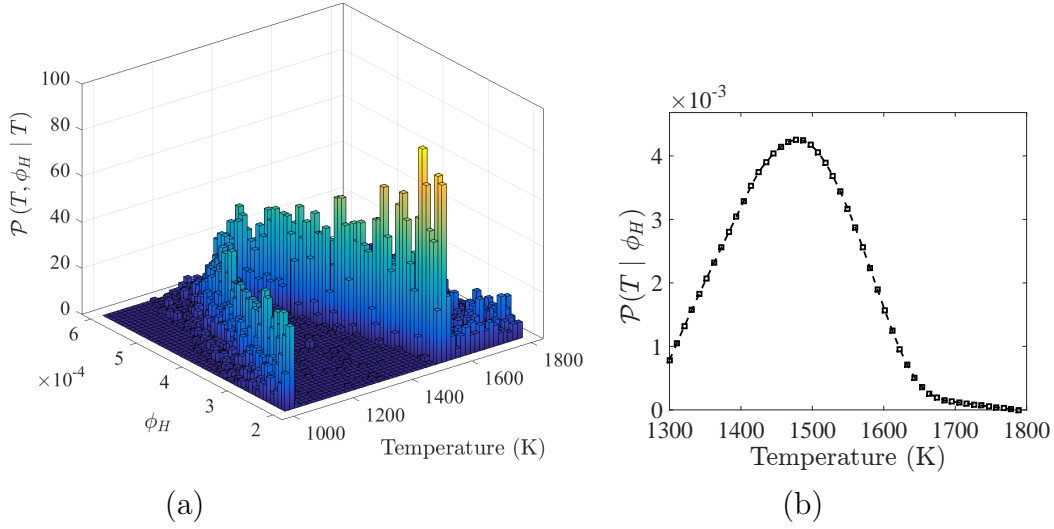


Figure 1.11: Conditional joint and marginal PDFs. (a) Conditional joint PDF of temperature and ϕ_H , $\mathcal{P}(T, \phi_H | 1000 \leq T \leq 1800)$ (b) Conditional marginal PDF of temperature, $\mathcal{P}(T | 4 \times 10^{-4} \leq \phi_H \leq 6 \times 10^{-4})$.

distribution with a peak around 1480 (K) and a significant variance. However, the profile is skewed toward higher temperatures, mostly because of preheating of the flame by the hot jet. The plateau at the right end of the $\mathcal{P}(T | \phi_H)$, where the flame starts to diminish, is associated with the burned-mixed zone. Since the standard deviation of $\mathcal{P}(T | \phi_H)$ is relatively high, the temperature might not be a good indicator for the flame location in the simulated TJI-TPJ configuration as opposed to standard turbulent premixed flames.

In addition to heat release, temperature, and species we have also considered the behavior of turbulent variables like vorticity in the TJI-TPJ. Figure 1.12 shows the contours of vorticity magnitude, $\omega = |\vec{\omega}|$, for both non-reacting and reacting cases. The contour values have been adjusted so that quantitative comparisons can be made. It can be seen in figure 1.12(a) that the simulated non-isothermal jet is highly turbulent with significant fluctuations at all length (and time) scales. Overall, a similar vorticity field is observed in reacting and non-reacting flows, even though the small-scale turbulent structures are clearly depleted by

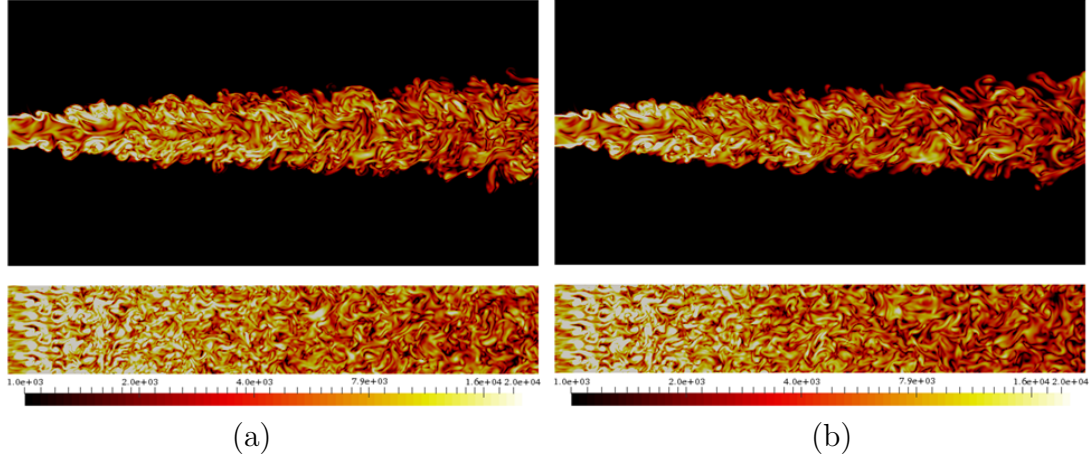


Figure 1.12: Instantaneous vorticity magnitude, ω , contours for (a) Non-reacting and (b) Reacting cases at $t = 17\tau_0$.

the combustion. In the near-field region, the vortex stretching and compressibility are the sources of the vorticity production. Further downstream in the developed region, the significant variations in density and pressure cause the Baroclinic torque, $\vec{\beta} = \frac{1}{\rho} \nabla \rho \times \nabla P$, to play a more important role in generating vorticity. This behavior is generally the same in both non-reacting and reacting flows. Close to the flame zone, the Baroclinic torque and the vortex stretching are the main sources of generating vorticity. However, in the combustion zones the vorticity field is negatively affected by the reaction because heat release induces volumetric flow expansion and temperature dependency of viscosity increases the dissipation of vorticity.

The flame surfaces are convected, wrinkled, and strained (much more intensely in the near-field region) by the turbulence propagating with relatively high velocities parallel and perpendicular to the coflow. Yet, even for the lean premixed flame considered here, the turbulence is not strong enough to cause a noticeable local flame extinction and flame surface breakup as observed in figure 1.8(b). There is a pressure field associated with the heat of reaction of the wrinkled flame and expanded flow, that indirectly affects the flame sheet

evolution through oscillations in the velocity field. As expected, there are also locally large density drops in the combustion zones. The accumulative effects of pressure and density gradients and their misalignment make the Baroclinic torque (or the magnitude of it, $\beta = |\vec{\beta}|$) a suitable turbulent “hydrodynamic” variable for characterizing the simulated TJI-TPJ.

In figure 1.13(a) it can be observed that even in the absence of the reaction, significant β is generated at the shear layer due to density jump between hot jet and coflow. Further downstream, turbulent mixing causes more distributed values of low level β throughout the domain, particularly, at small-scales. The same general behavior can be observed to exist in figure 1.13(b) for the reacting case. In fact, the Baroclinic torque distribution in the near-field region is very similar even though they are different in the developed region when there is combustion. In the near-field region and inside the reactive zones at the overlap of the hot product and burned-mixed zones, β is generated mainly due to density difference between the incoming hot jet and products of the lean coflow combustion. In the developed region, the dominant mechanism for Baroclinic torque generation is changing as the density gradients decrease. Large scale variations in β are virtually eliminated by the combustion in the reacting flow. The importance of β in representing the flame front is clearly evident in figure 1.13(b), where it is shown that the local maximum values of β in the flame zone are remarkably similar to the local maximum values of \dot{Q}_e and ϕ_H . The single point marginal PDFs of Baroclinic torque for non-reacting and reacting cases are shown in figure 1.14. Consistent with figures 1.13(a) and (b), a wide range of Baroclinic torque values exists in the domain in both cases. This figure also confirms that the high β values seen in the non-reacting flow disappear in the reacting flow and the relatively small values become dominant. This indicates that in the simulated TJI-TPJ configuration, combustion negatively affects the large and small-scale vorticity fields not only because of volumetric flow expansion and

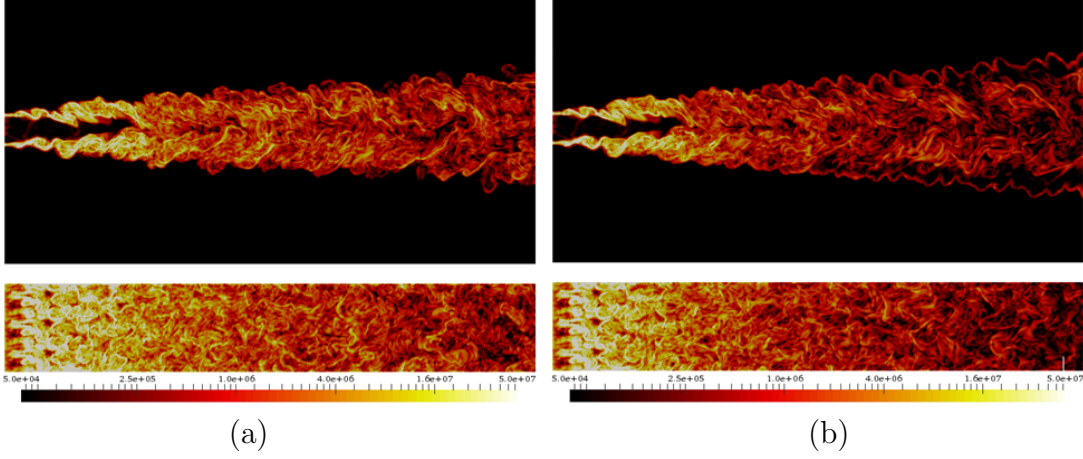


Figure 1.13: Instantaneous Baroclinic torque, β contours for: (a) Non-reacting and (b) Reacting cases at $t = 17\tau_0$.

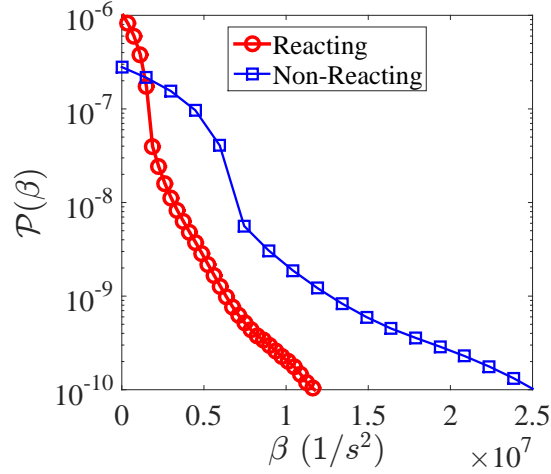


Figure 1.14: Marginal PDF of β , $\mathcal{P}(\phi_\beta)$.

increase in viscosity, but also because of reduction in high Baroclinic torque generation.

Figure 1.15(a) shows the conditional mean and confidence intervals of the Baroclinic torque, $\mu_\beta \pm \sigma_\beta$, conditioned on ϕ_H . The coflow values are included in these conditional plots. Note that by increasing ϕ_H one effectively moves from the coflow and burned-mixed zones toward the remnant hot jet zone and, afterward, to the flame zone. Figure 1.15(a) shows that at low ϕ_H values, associated with the burned mixed zone, the mean Baroclinic torque μ_β is small. μ_β increases in the hot jet zone but it maximizes at the flame zone. A

similar behavior to μ_β is observed for the scalar dissipation rate of H radical, χ_H , defined as [101]

$$\chi_H = \mathfrak{D} \left[\left(\frac{\partial \phi_H}{\partial x} \right)^2 + \left(\frac{\partial \phi_H}{\partial y} \right)^2 + \left(\frac{\partial \phi_H}{\partial z} \right)^2 \right], \quad (1.13)$$

where \mathfrak{D} is the diffusivity coefficient, a function of temperature. The scalar dissipation rate is tied to the turbulent velocity field. Since χ_H and β both are transported by turbulence from the jet to the coflow in a similar way, χ_H follows similar trends to those for β . The flame structure can be captured by χ_H .

Figure 1.15(b) shows the conditional mean and confidence intervals of χ_H , $\mu_{\chi_H} \pm \sigma_{\chi_H}$, versus ϕ_H . The relatively low values of μ_{χ_H} in the burned-mixed and coflow zones are due to the small and somewhat uniform values of ϕ_H in these zones. In the remnant hot jet zone, μ_{χ_H} increases due to stronger variations in ϕ_H and also \mathfrak{D} . High flame wrinkling results into large scalar gradients or χ_H at the flame front where $5 \times 10^{-4} \leq \phi_H \leq 6 \times 10^{-4}$ (area III.2 in figure 1.6c). However, in the two sides of the flame (zones III.1 and III.2 in figure 1.6c), behind the flame front in the burned-mixed zone side and in the preheated zone in the coflow side, μ_{χ_H} decreases. Thus, the highest values of χ_H are associated with the flame front, which can also be used to identify its location. Comparison between figures 1.15(a) and (b) additionally confirms that β is a suitable turbulent (hydrodynamic) quantity for identifying the flame in the TJI-TPJ configuration.

1.5.2 Turbulent flame speed

A simple method is used to calculate the turbulent flame speed. Figures 1.16(a) and (b) show the time and spanwise averaged temperature $\langle \overline{T} \rangle_s$ for non-reacting and reacting cases. The jet spread rate in the reacting flow is considerably greater than that in the non-reacting

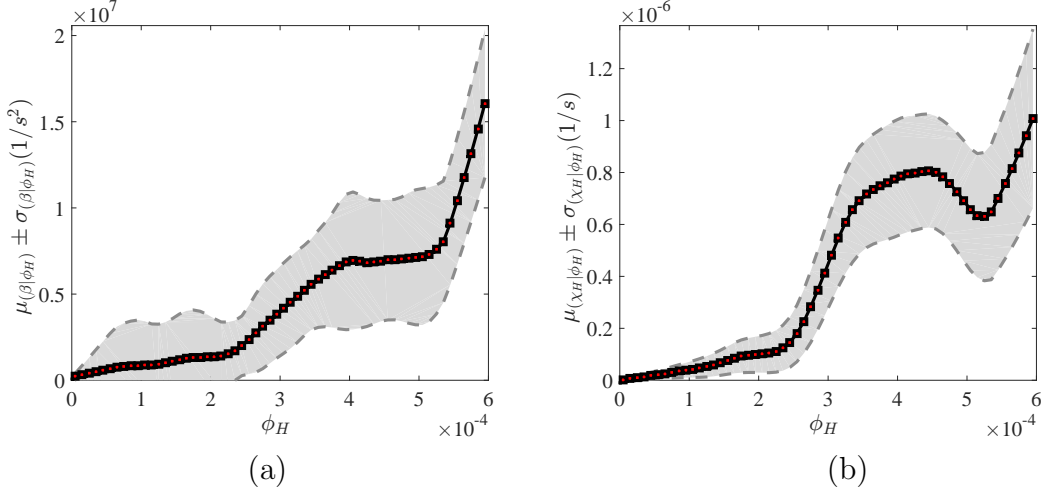


Figure 1.15: Conditional means and confidence bounds of (a) Baroclinic torque, β , and (b) scalar dissipation rate of H radical.

flow, mainly, because of the turbulent burning velocity. The combustion induced changes in the flow and turbulence within the burned-mixed and hot product jet zones also have some effects on the jet spread rate. These effects can not be well characterized and are expected to be less significant than the flame propagation speed; thus, they are not included in our flame speed calculations.

Assume points \mathbf{p}_N and \mathbf{p}_R in figures 1.16 to be located at the edge of the non-reacting and reacting jets at the geometrical locations of $(x_{\mathbf{p}_N}, y_{\mathbf{p}_N})$ and $(x_{\mathbf{p}_R}, y_{\mathbf{p}_R})$, where $x_{\mathbf{p}_N} = x_{\mathbf{p}_R}$. The jet angles can be calculated as $\alpha_N = \tan^{-1}\left(\frac{y_{\mathbf{p}_N}}{x_{\mathbf{p}_N}}\right)$ and $\alpha_R = \tan^{-1}\left(\frac{y_{\mathbf{p}_R}}{x_{\mathbf{p}_R}}\right)$, assuming the origin of the angles is located at the virtual jet origin [53]. The turbulent flame speed at any axial location can then be calculated as $S_T = \frac{y_{\mathbf{p}_R} - y_{\mathbf{p}_N}}{t_T}$, where $t_T = \frac{u}{x_{\mathbf{p}_N}}$ and u are time and convective velocity. Figure 1.17(a) shows the variations of the calculated turbulent flame speed, S_T , and the turbulence intensity, $I = \frac{(u'^2 + v'^2 + w'^2)^{\frac{1}{2}}}{U_{ref}}$, at the flame front, where $U_{ref} = \frac{U_{co} + U_j}{2} = 300$ (m/s) is the average of the coflow and hot product jet velocities. It is observed that the turbulence intensity constantly decreases along the jet, as the jet

spreading and combustion simultaneously dissipate turbulent structures inside the jet and at the flame front. It is also shown that the turbulent flame speed is directly correlated to the turbulence intensity; the higher turbulence intensity, the higher turbulent flame speed. These results are consistent with previous studies [59, 12]. Various analytical, numerical, and experimental studies have been previously used to calculate the hydrogen turbulent flame speed [112, 97]. Despite differences in thermo-chemical conditions, the calculated hydrogen turbulent flame speeds are found to be comparable but slightly higher than those reported in the literature possibly due to different flow/flame structures in the burned zone and the existence of the hot jet. Close examination of the instantaneous temperature, heat release, and species distributions at different times indicates strong variations in flame structure and turbulence intensity, which is not evident in the mean flame speed profiles in figure 1.17(a). Figure 1.17(b) shows the conditional (conditioned on ϕ_H) mean and confidence intervals of I , $\mu_I \pm \sigma_I$, versus ϕ_H for the entire flow. The high standard deviation of turbulence intensity at the flame zone, where $4 \times 10^{-4} \leq \phi_H \leq 6 \times 10^{-4}$, is an indicator of a strong variation in local flame speed. Contrary to the standard turbulent premixed flames, in the studied TJI-TPJ configuration a high temperature and momentum turbulent flow exists behind the flame front in the burned zone, which enhances the combustion at the flame zone and increases the flame burning velocity, S_T . This is evident in figure 1.17(b), which shows relatively high turbulence intensities in the burned-mixed and hot jet zones ($1 \times 10^{-4} \leq \phi_H \leq 4 \times 10^{-4}$).

1.5.3 Temporal and spatial variations of turbulent variables

In order to quantitatively characterize the flame and turbulence dynamics in the TJI-TPJ, time signals of the streamwise velocity, temperature, and H radical mass fraction, with the corresponding PDF, mean, μ , standard deviation, σ , Skewness, \mathcal{S} , and Kurtosis, \mathcal{K} , for Case3

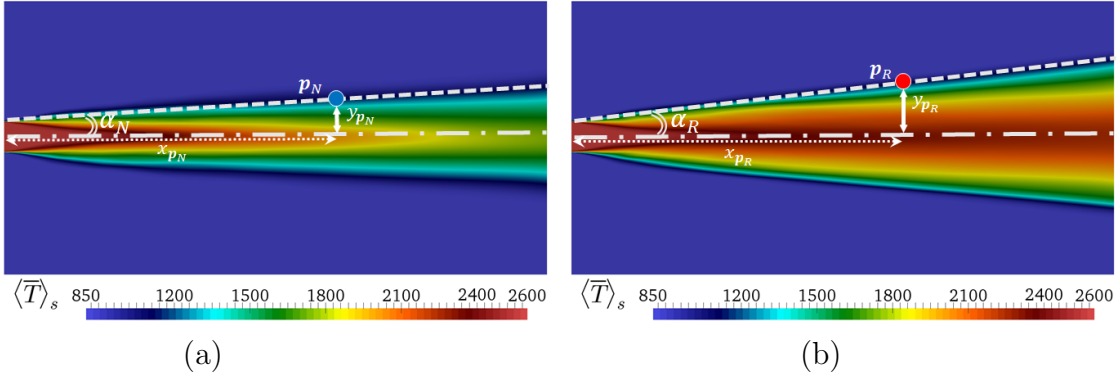


Figure 1.16: Contours of time and spanwise averaged temperature and the jet span spread rate for (a) Non-reacting and (b) Reacting cases.

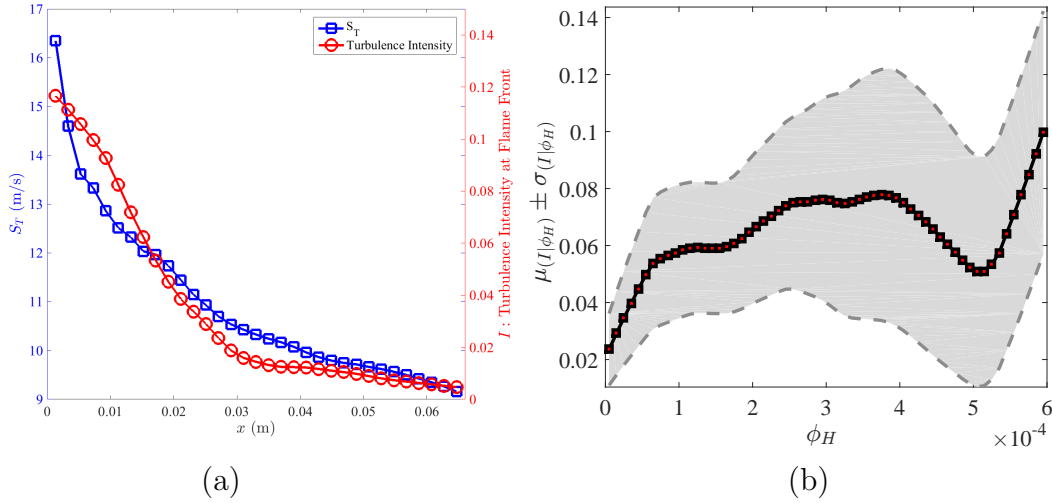
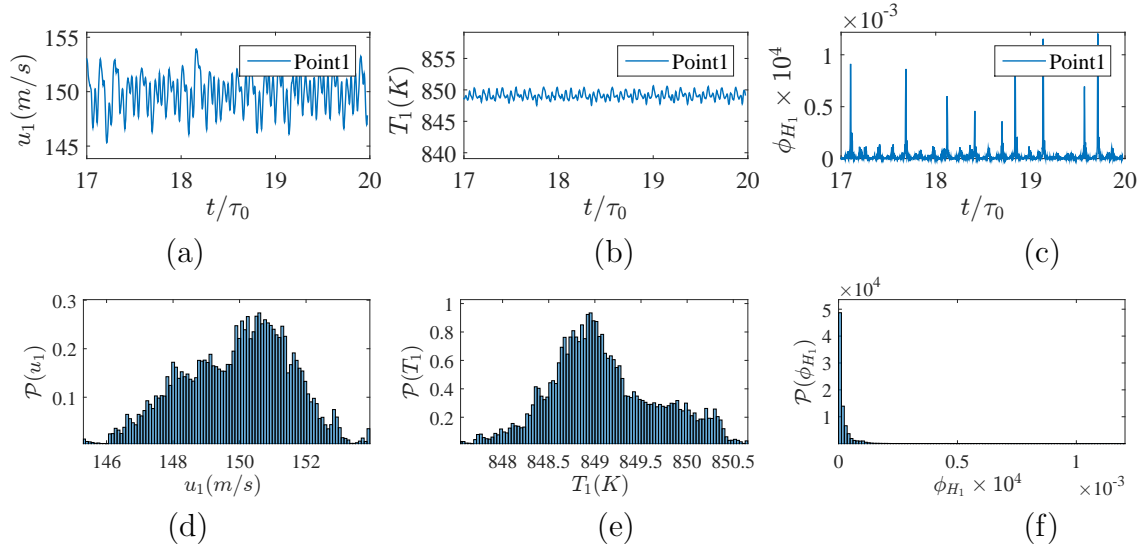


Figure 1.17: (a) Turbulent flame speed, S_T , and turbulence intensity, I , at flame front vs. streamwise flow direction, (b) Conditional mean and confidence bounds of turbulence intensity.

presented in table 1.1 are presented in figures 1.18-1.22 for the duration of $17\tau_0$ to $20\tau_0$ at *five* different points shown in figure 1.1.

Point1: This point is located inside the coflow far away from the flame front. Figure 1.18 provides the essential information required to understand the flow variations at this point. Figures 1.18(a)-(c) show the time variation of instantaneous streamwise velocity, u_1 , temperature, T_1 , and H radical mass fraction, ϕ_{H_1} , while figures 1.18(d)-(f) present the associated PDFs. The statistics are presented in figure 1.18(g). The time signals of T_1 , u_1 , and ϕ_{H_1} show oscillations around the coflow values close to those provided in table 1.1 for Case3. The mean and standard deviation of velocity are $\mu_{u_1} = 149$ (m/s) and $\sigma_{u_1} = 1.62$ (m/s), consistent with the coflow values. The small negative value of \mathcal{S}_{u_1} is consistent with the $\mathcal{P}(u_1)$ to be negatively skewed. \mathcal{K}_{u_1} is equal to 2.75, close to the value for a normal distribution. The T_1 signal is positively skewed, with small standard deviation. Since Point1 is located out of the combustion zones, $\mu_{\phi_{H_1}}$ and $\sigma_{\phi_{H_1}}$ are zero. Nevertheless, large positive values of $\mathcal{S}_{\phi_{H_1}}$ and $\mathcal{K}_{\phi_{H_1}}$ indicate that small residuals of the H radical produced in the flame zone are sporadically transported to Point1.

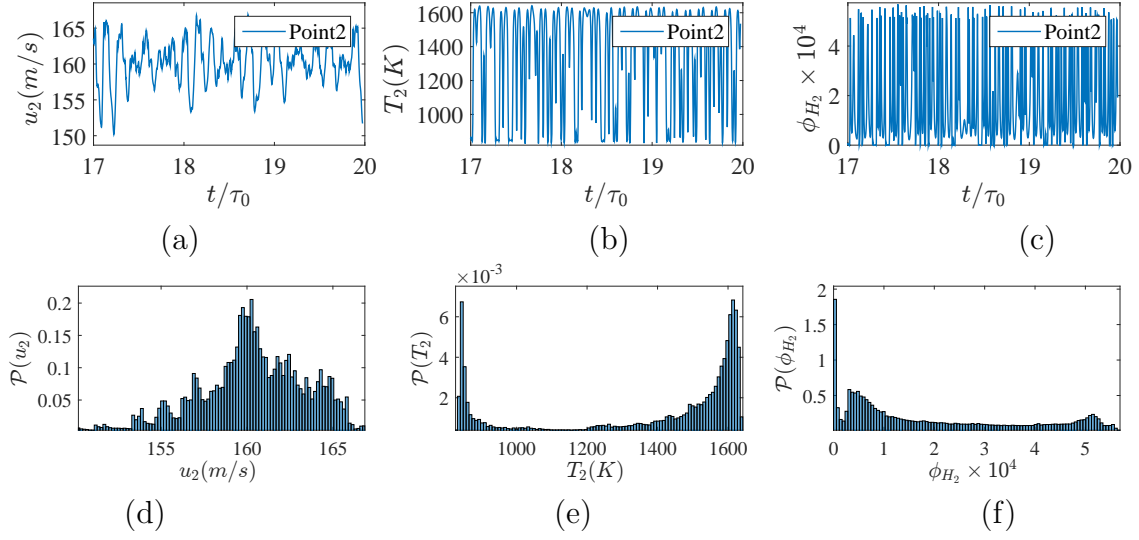
Point2: This point is located in the preheated zone very close to the flame front (in the coflow side). However, the flow at this point is still strongly affected by the coflow; the streamwise velocity component oscillates in the range of U_{co} as shown in figures 1.19(a) and (d). The mean velocity μ_{u_2} is equal to 160 (m/s) with relatively small standard deviation, $\sigma_{u_2} = 3.12$ (m/s). The u_2 signals also show an asymmetric, negatively skewed behavior. T_2 signals show a bimodal distribution of temperature varying widely from coflow temperature T_{co} to the adiabatic flame temperature of the lean mixture as normally expected in the preheated zone of premixed flames [17]. $\mathcal{P}(\phi_{H_2})$ forms a trimodal distribution indicating



(g) μ , σ , \mathcal{S} , and \mathcal{K} at Point1

	μ	σ	\mathcal{S}	\mathcal{K}
u_1	149	1.62	-0.251	2.5
T_1	849	0.6	0.31	2.75
$\phi_{H_1} \times 10^4$	0.0	0.0	7.1	62.4

Figure 1.18: (a-c) instantaneous variations of u_1 , T_1 , and ϕ_{H_1} in time; (d-f) PDF of u_1 , T_1 , and ϕ_{H_1} ; and (g) associated μ , σ , \mathcal{S} , and \mathcal{K} .



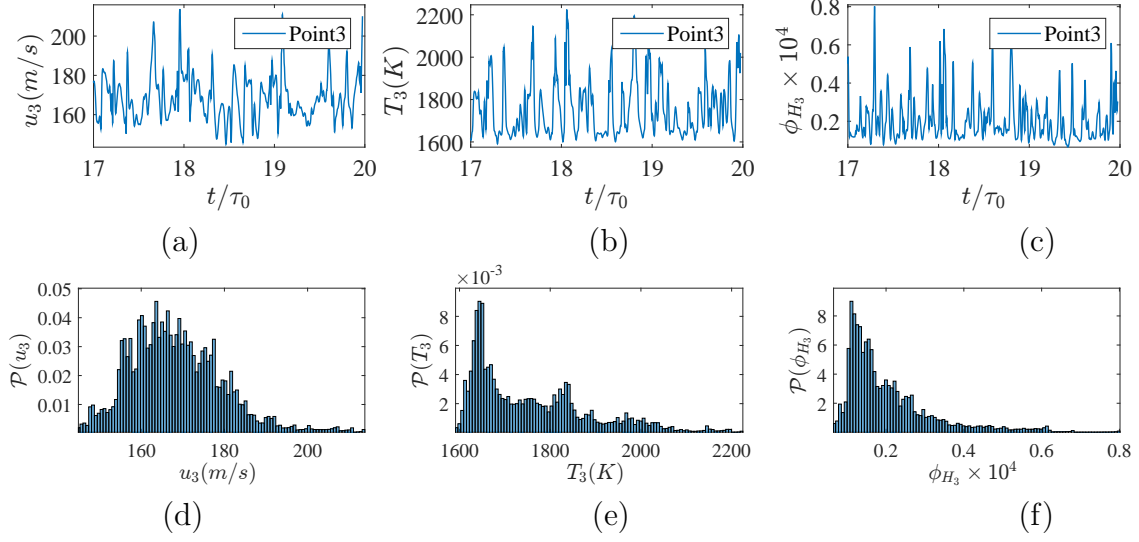
(g) μ , σ , \mathcal{S} , and \mathcal{K} at Point2

	μ	σ	\mathcal{S}	\mathcal{K}
u_2	160	3.12	-0.44	3.09
T_2	1345	285	-0.7	1.90
$\phi_{H_2} \times 10^4$	1.9	1.75	0.74	2.11

Figure 1.19: (a-c) instantaneous variations of u_2 , T_2 , and ϕ_{H_2} in time; (d-f) PDF of u_2 , T_2 , and ϕ_{H_2} ; and (g) associated μ , σ , \mathcal{S} , and \mathcal{K} .

that in time three different types of the flow pass through Point2, namely those seen in the coflow, the preheated, and flame zones. At this point, the ϕ_H values vary from zero (the coflow), to 1×10^{-4} (the preheated flame zone), to 5×10^{-4} (the flame front).

Point3: This point is also located at the flame front but inside the reacting zone. The flow at Point3 is affected by the burned-mixed zone. Figures 1.20(a) and (d) show that the turbulent flow at this point has higher velocity than the coflow, therefore, $\mu_{u_3} = 169$ (m/s) and $\sigma_{u_2} = 11.46$ (m/s) are larger than their corresponding values at Point2. $\mathcal{P}(u_3)$ is positively skewed with the highest Kurtosis, $\mathcal{K}_{u_3} = 4.04$, as compared to those at other points. It is shown in figures 1.20(b) and (e) that Point3 temperature oscillates between the flame front temperature and the higher temperatures associated with the burned-mixed



(g) μ , σ , \mathcal{S} , and \mathcal{K} at Point3

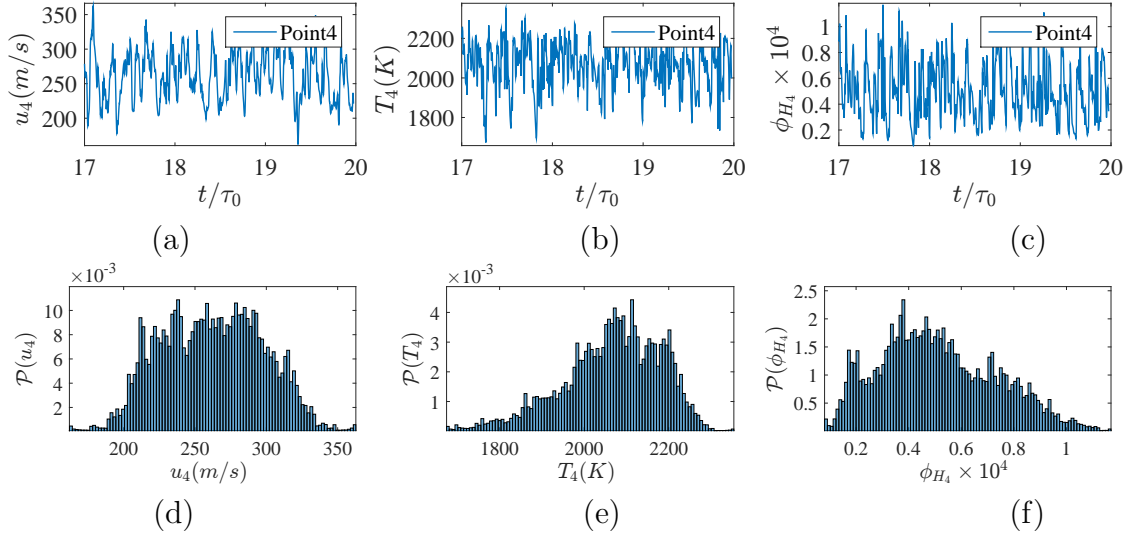
	μ	σ	\mathcal{S}	\mathcal{K}
u_3	169	11.46	0.78	4.04
T_3	1757	130	1.05	3.50
$\phi_{H_3} \times 10^4$	0.2	0.11	1.82	6.71

Figure 1.20: (a-c) instantaneous variations of u_3 , T_3 , and ϕ_{H_3} in time; (d-f) PDF of u_3 , T_3 , and ϕ_{H_3} ; and (g) associated μ , σ , \mathcal{S} , and \mathcal{K} .

zone with μ_{T_3} and σ_{T_3} of 1757 (K) and 130 (K), respectively. $\mathcal{P}(T_3)$ is a right skewed distribution, which suggests that this point is indeed affected by the burned-mixed zone. As expected, the ϕ_{H_3} values are lower than those in the flame zone. $\mathcal{P}(\phi_{H_3})$ also shows a right skewed distribution with a relatively small peak values and less weighting at the right tail. Since the flame front is highly distorted and the flame location changes in time, the characterization of the flame by fixed spatial points is difficult. Our examination of heat release rate and H radical contours indicates that the flame front flickers between Point2 and Point3 in time. Thus, the simultaneous results in these points provide a better understanding of the flame behavior and associated scalar and hydrodynamic fields in time.

Point4: This point is located inside the burned-mixed zone, where unlike Point3, the flow field is significantly affected by the hot product jet. Figures 1.21(a) and (d) show that the velocity at this point is widely changing in time with the mean velocity of $\mu_{u_4} = 262 \text{ (m/s)}$ and relatively high standard deviation of $\sigma_{u_4} = 35.55 \text{ (m/s)}$, an indication of intensive turbulence. A Gaussian distribution can be fitted to $\mathcal{P}(u_4)$ since it generates a near zero skewness of $\mathcal{S}_{u_4} = 0.02$ and Kurtosis of $\mathcal{K}_{u_4} = 2.31$. The influences of the hot product jet can be more clearly observed in the T_4 signals which they are generally greater than T_3 . The mean and standard deviation of temperature at this point, μ_{T_4} and σ_{T_4} , are equal to 2065 (K) and 116 (K) , respectively. $\mathcal{P}(T_4)$ is a negatively skewed distribution with a high peak around the mean values of $\mu_{T_4} = 2065 \text{ (K)}$. Similarly, $\mu_{\phi_{H_4}}$ is higher than $\mu_{\phi_{H_3}}$, indicating again the influence of the hot jet which consists of higher H radicals. The PDF of ϕ_{H_4} , $\mathcal{P}(\phi_{H_4})$, is positively skewed and has a concentrated distribution and a high peak around the mean value of 0.5×10^{-4} .

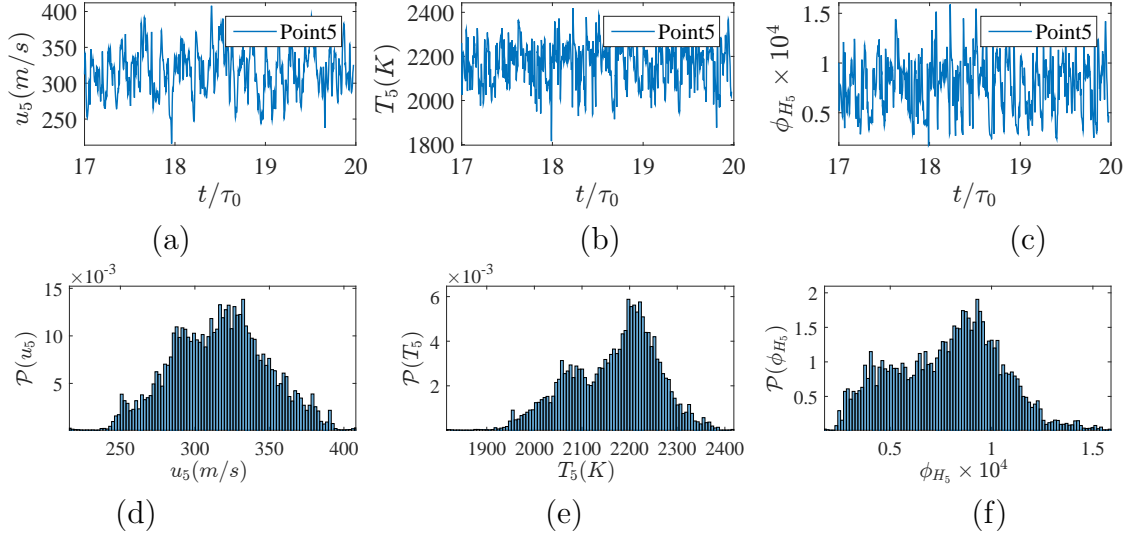
Point5: This point is located deep inside the hot product jet, exhibiting the features expected for a reacting hot turbulent jet mixing with a cooler premixed fuel-air mixture. Figure 1.22 provides the essential information for studying the temporal flow features at this point. The velocity values are the highest when compared to those at other points with $\mu_{u_5} = 316 \text{ (m/s)}$ and $\sigma_{u_5} = 32.1 \text{ (m/s)}$. The Skewness and Kurtosis for the velocity distribution are equal to -0.002 and 2.65 (figure 1.22g) which suggest a symmetric and nearly Gaussian distribution. The temperature signals at this point (figure 1.22b) show a bimodal $\mathcal{P}(T_5)$ distribution (figure 1.22e), indicating the influences of both burned-mixed and hot jet zones. This suggests that distinguishing burned-mixed zone from the hot product zone may not be trivial and there is an overlap between these two zones even at the center of the



(g) μ , σ , \mathcal{S} , and \mathcal{K} at Point4

	μ	σ	\mathcal{S}	\mathcal{K}
u_4	262	35.55	0.02	2.31
T_4	2065	116	-0.61	3.12
$\phi_{H_4} \times 10^4$	0.5	0.21	0.36	2.45

Figure 1.21: (a-c) instantaneous variations of u_4 , T_4 , and ϕ_{H_4} in time; (d-f) PDF of u_4 , T_4 , and ϕ_{H_4} ; and (g) associated μ , σ , \mathcal{S} , and \mathcal{K} .



(g) μ , σ , \mathcal{S} , and \mathcal{K} at Point5

	μ	σ	\mathcal{S}	\mathcal{K}
u_5	316	32.10	-0.002	2.65
T_5	2168	91	-0.4	2.72
$\phi_{H_5} \times 10^4$	0.7	0.26	-0.009	2.453

Figure 1.22: (a-c) instantaneous variations of u_5 , T_5 , and ϕ_{H_5} in time; (d-f) PDF of u_5 , T_5 , and ϕ_{H_5} ; and (g) associated μ , σ , \mathcal{S} , and \mathcal{K} .

hot jet. However, higher temperature and H radical mass fraction at Point5 (figure 1.22b and c), in comparison to those at Pint4, indicate that the dominant effects at Point5 are those due hot product jet. This is also shown in figure 1.22(e) and (f), where the $\mathcal{P}(T_5)$ and $\mathcal{P}(\phi_{H_5})$ are observed to peak around higher T and ϕ_{H_5} values.

The results in figures 1.18-1.22 show the time history of the flow variables and appropriate statistics at limited number of points. To better show the average spatial variations of flow variables in the TJI-TPJ, the mean and root mean square (rms) values of the streamwise velocity and temperature along several axial and lateral directions are considered. These results are obtained by time averaging for about $17\tau_0$ which is a sufficiently long time to assess the high order statistics. To analyze the self similarity [86, 32] of these variables in the

simulated TJI-TPJ configuration, one may normalize the calculated statistics by spatially variable normalization factors; for example, velocity components might be normalized by the maximum local velocity. However, here we scale the variables by constant factors (i.e. the coflow velocity and temperature, U_{co} and T_{co}) in order to show their spatial behavior.

Figure 1.23 shows the mean velocity and temperature, $\langle \bar{u} \rangle_s / U_{co}$ and $\langle \bar{T} \rangle_s / T_{co}$, versus the streamwise direction ($\xi = x/D$) at $\zeta = y/(D/2) = 0, 4$, and 8. Note that the origin of ζ is at the middle of computational domain, so that $\zeta = 0$ and $\zeta = 8$ correspond to the jet centerline and coflow, respectively. It can be observed in figure 1.23(a) that for both reacting and non-reacting flows inside the hot product jet zone the mean velocity generally decreases along the streamwise direction, first very rapidly in the near-field region then slowly in the developed region. The behavior is similar for both flows in the near-field region. However, in the developed region $\langle \bar{u} \rangle_s / U_{co}$ decreases less in the reacting flow than in the non-reacting flow, suggesting that the heat of combustion not only causes the jet to spread in the cross-stream, it also enhances the jet velocity in the streamwise direction. The non-reacting $\langle \bar{u} \rangle_s / U_{co}$ values inside the coflow ($\zeta = 8$) stay unchanged, whereas the reacting values slightly increase at the intersection of the coflow and combustion zones.

The streamwise variations of $\langle \bar{T} \rangle_s / T_{co}$ as shown in figure 1.23(b) exhibit more interesting trends. The maximum value of $\langle \bar{T} \rangle_s / T_{co}$ is equal to $T_j / T_{co} = 2556/850 = 3.01$ for both non-reacting and reacting flows and occurs at the inlet. As expected, along the jet centerline ($\zeta = 0$) the mean temperature is decreased less and is even slightly increased in the reacting case because of the combustion. The spatial shifts between different flow zones can be better represented along $\zeta = 4$, where the coflow is initially the dominant zone. At this cross-stream location, $\langle \bar{T} \rangle_s / T_{co}$ of the reacting flow increases from 1 at $\xi \simeq 8$ to 2.2 at $\xi \simeq 16$, indicating the change of flow from the coflow zone to the burned-mixed zone. However, the mean

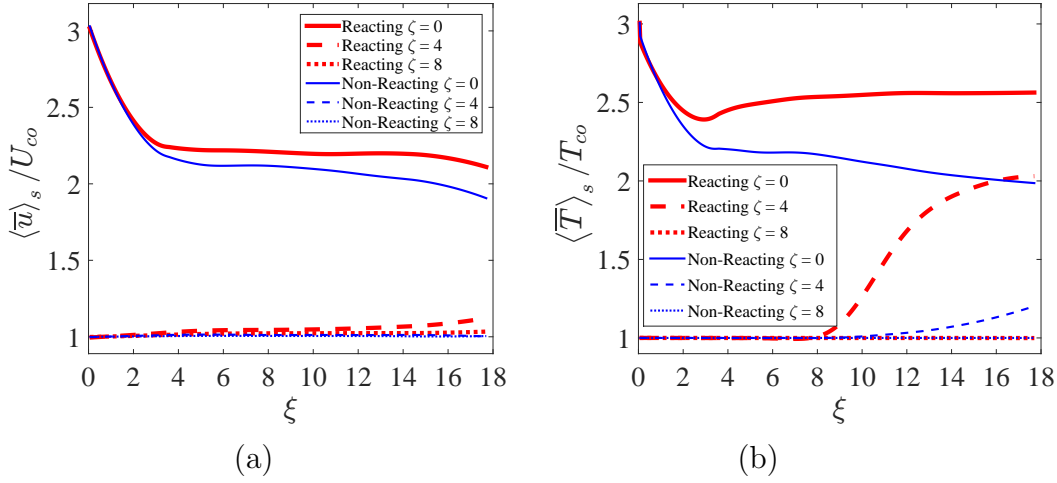


Figure 1.23: Streamwise variations of averaged values (a) streamwise velocity component and (b) temperature profiles at different cross-stream locations. ($\langle - \rangle_s$ refers to both time and spanwise averaged value. Thick and thin lines represent the reacting and non-reacting cases, respectively)

temperature in the non-reacting flow starts to slightly increase at $\xi \geq 10.5$. The flow field at $\zeta = 8$ for both cases stays within the coflow zone as $\langle \bar{T} \rangle_s / T_{co}$ remains constant and equals to 1.

The cross-stream profiles of $\langle \bar{u} \rangle_s / U_{co}$ and $\langle u_{rms} \rangle_s / U_{co}$ at three different streamwise locations are shown in figures 1.24(a) and (b). These profiles are consistent with the time varying velocities in figures 1.18-1.22, where the mean velocity is shown to continuously decrease from the jet centerline to the coflow and the maximum rms of velocity to occur at the jet edges. The trends are similar in non-reacting and reacting flows. In the near-field region, the peak rms velocity occurs close to the flame zone where the rms temperature is the highest, indicating significant effects of the turbulence on combustion and vice versa in this region. Further away from the inlet, the maximum values of rms velocity and temperature occur at different cross-stream locations, indicating much less interactions between the jet and flame zones. Nevertheless, the ratio of $\frac{u_{rms}}{\langle \bar{u} \rangle_s}$ in both flows are less than 0.03, which

shows that the turbulence is not unusually strong in the simulated TJI-TPJ, rather it is compatible with those reported in the studies on non-isothermal non-reacting planar jets [114, 113] and thus is not able to break the flame surface and create significant local flame extinction in the simulated flow.

Figure 1.24(c) presents the $\langle \overline{T} \rangle_s / T_{co}$ for both non-reacting and reacting cases at three different streamwise locations along the cross-stream direction. As it is also observed in figure 1.23, the maximum jet temperature decreases in streamwise direction much less in the reacting flow. The $\langle \overline{T} \rangle_s / T_{co}$ reduction rate from $\xi = 16$ to 4 is %74 for the non-reacting case, whereas it is %93 for the reacting case. Consistent with figures 1.18-1.22, time averaged temperature values decrease continuously from the hot jet zone to the coflow zone even in the reacting flow since the maximum temperature of the combustion of the lean coflow is less than the jet temperature. The combustion effects on temperature fluctuations or rms are rather different. The values of $\langle T_{rms} \rangle_s / T_{co}$ versus the lateral axis for both non-reacting and reacting cases at three different streamwise locations, $\xi = 4, 10$, and 16, are shown in figure 1.24(d). Maximum values of non-reacting $\langle T_{rms} \rangle_s / T_{co}$, consistent with the velocity rms, occur close to the jet edges and decrease in the streamwise direction. This behavior is expected for a heated turbulent jet mixing with the colder coflow. Figure 1.24(d) also reveals that the jet expands to about $2.3D$ at $\xi = 16$ in the non-reacting case, whereas jet span is $4.3D$ at the same axial location in the reacting case. The maximum values of $\langle T_{rms} \rangle_s / T_{co}$ occur close to the jet edges for both cases. In the developed region of the reacting flow, the peak rms temperature, which occurs at the cross-stream locations is very different than the peak of the rms velocity. Since high temperature variations locally happen at the flame zone, T_{rms} can be used to identify this zone, in addition of \dot{Q}_e , ϕ_H , and β .

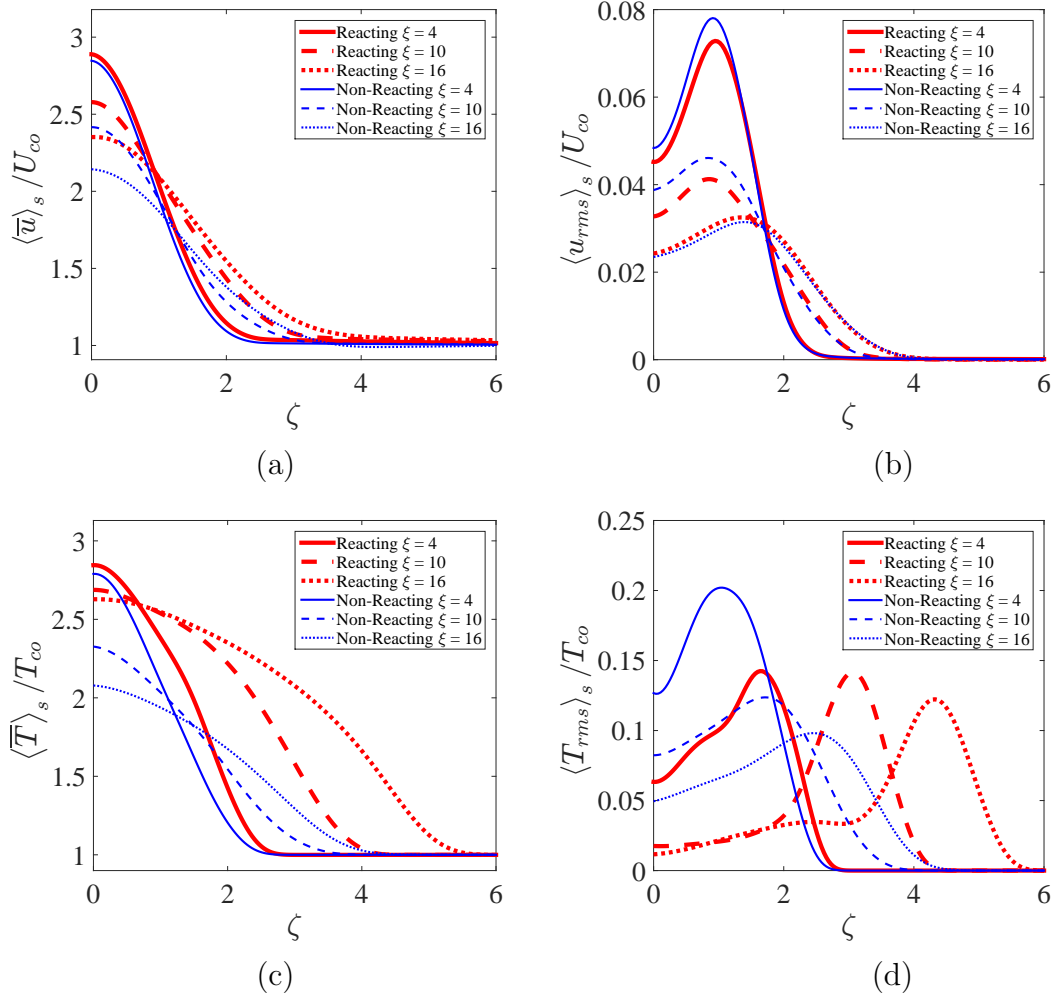


Figure 1.24: Cross-stream variations of (a) mean streamwise velocity, (b) rms of streamwise velocity, (c) mean temperature, and (d) rms of temperature. (Thick and thin lines represent the reacting and non-reacting cases, respectively)

Comparison of the mean velocity and temperature (shown in figures 1.23a and 1.23c) and the rms of velocity and temperature (shown in figure 1.24b and 1.24d) indicates that combustion effects on the scalar field are much more notable as compared with the velocity field. It also shows that these two fields are not correlated specially at the flame zone. This is more important and has to be considered in developing closure models for LES and RANS of TJI-assisted combustion systems.

1.6 Results and discussions: jet and coflow effects on development of premixed and non-premixed flames including localized extinction in TJI-assisted combustion

In this section, results concerning the effects of coflow and jet conditions on the physical processes involved in the TJI-assisted combustion are presented and discussed. Figures 1.25(a)-(f) present the instantaneous temperature contours in a $x - y$ plane at the middle of the three-dimensional domain for the conditions presented in table 1.1 at $t = 17\tau_0$ (s). The contour range values of $850(K) \leq T \leq 2600(K)$ are chosen for all cases so that a better comparisons can be made. In the nearfield region, $\xi = x/D \lesssim 4$, the hot incoming jet causes significant autoignition at the jet shear layer and surrounding areas, where the jet heats the premixed coflow and, ultimately, sustains the flame, even, in ultra-lean fuel-air mixtures. In addition to the combustion, highly distorted turbulent structures are developed in this region, which strongly interact with the combustion. The flame-turbulence interactions and mixing of the incoming hot jet with cooler premixed coflow in the reacting shear layer creates relatively thick and geometrically complex flame in the nearfield region. Independent of the coflow compositions, visually, similar flame/turbulence structures and shear layers are developed in the nearfield region in all cases, indicating the dominance of the incoming jet hydrodynamics. Even though the coflow composition is the same in Case3, Case5, and Case6, temperature contours in figures 1.25(e) and (f) when compared to figure 1.25(c), confirm that the nearfield jet variables are indeed influenced more by the incoming jet than the coflow combustion.

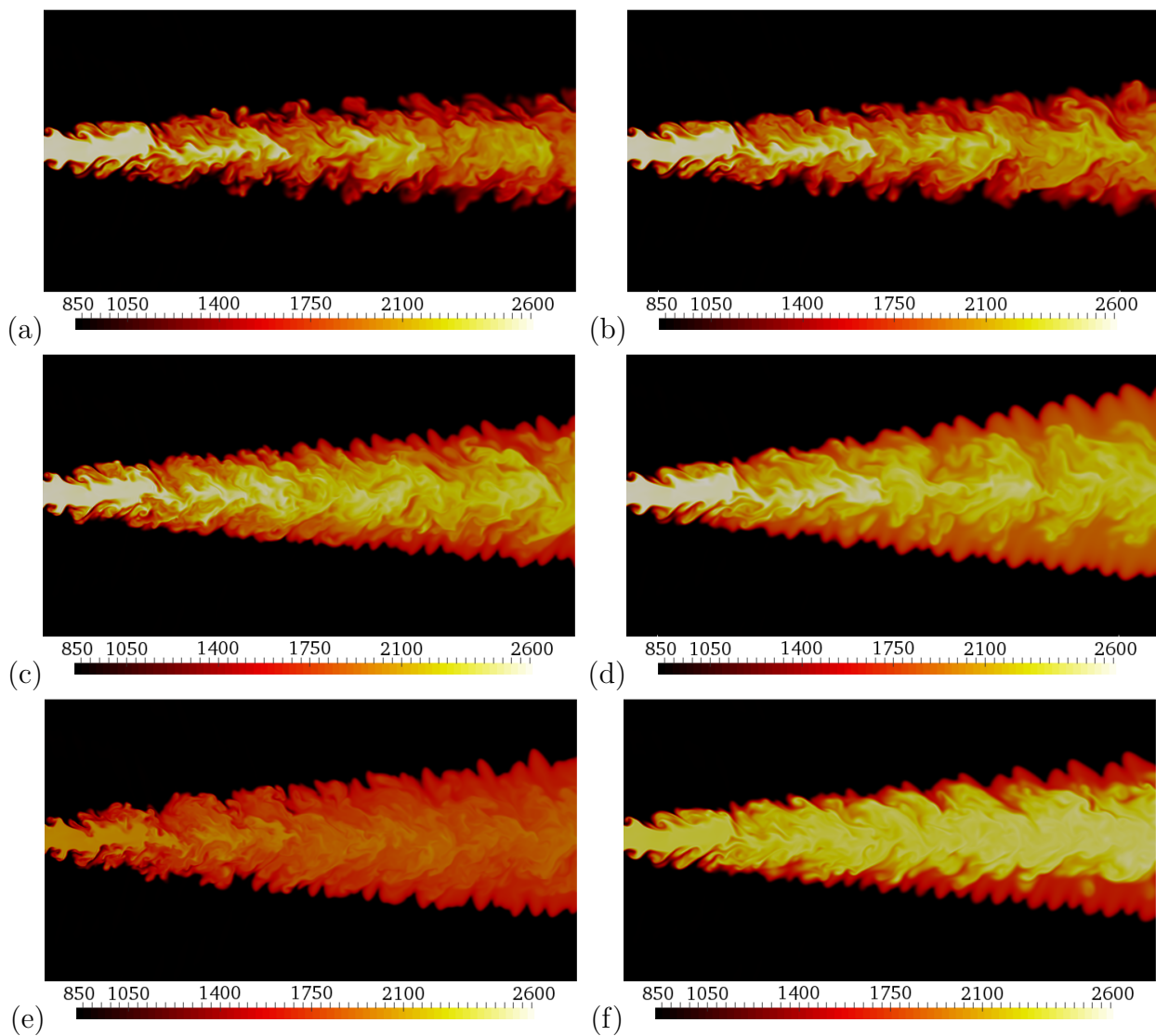


Figure 1.25: Instantaneous temperature contours at the middle spanwise plane ($z = 1.5D$) and $t = 17\tau_0$ for (a) Case1, (b) Case2, (c) Case3, (d) Case4, (e) Case5, and (f) Case6.

Marching in the streamwise direction in the developed region ($\xi \geq 4$), where spatially continuous and distorted reacting and flame zones are generated, the effect of coflow equivalence ratio is more clear. In this region, the turbulent premixed flame separates from the jet and active turbulent flow regions as it spreads into the coflow in cross-stream direction. This separation develops various combustion zones in the simulated TJI-TPJ configurations based on the flame/turbulence parameters as *i*) hot product jet zone, *ii*) premixed flame zone, and *iii*) burned-mixed zone. The hot product jet zone is identified by the highest temperature values. The flame zone is identified by relatively low temperature values associated with the adiabatic flame temperature of lean hydrogen-air combustion with initial coflow temperature of 850 (K). The burned-mixed zone is recognized based on the intermediate temperature values. The burned-mixed zone in the TJI-TPJ has some similarities with the burned zone appearing in standard turbulent premixed flames [88, 93, 17], but it has a relatively higher temperature and product species mass fraction values. The complexity of this region arises from the strong interactions of the inner hot product jet turbulence and composition fields with the lean premixed turbulent flame. Therefore, there may not be well defined boundaries between this zone and its neighboring zones, particularly, with the hot product jet zone. In the spanwise direction (not shown here), the flow field is initially homogeneous and isotropic due to the imposed turbulent inflow. It stays homogeneous further downstream, but with considerably larger turbulent scales. Detailed features of various zones and regions in TJI-assisted combustion systems have been discussed in reference [109].

Figure 1.25 shows that the flame progression or the jet growth rate of jet thermal half width in the developed region ($\xi \geq 4$) is highly dependent on the coflow mixture conditions. For Case3 and Case4 with coflow equivalence ratios of 0.35 and 0.5 the flame is stable and widely spreads in the cross-stream directions (figures 1.25c and d). However, the combustion

of ultra-lean mixtures in Case1 and Case2 with equivalence ratios of 0.1 and 0.2 is weak as shown in figures 1.25(a) and (b) hardly establishes stable and distinguishable combustion zones, showing significant localized flame extinction and re-ignition (more details are provided in section 1.6.2). Despite different burned jet thermo-chemical conditions, the growth and structure of combustion zones for Case5 and Case6 (figures 1.25e and f) are almost the same as those for Case3 (figure 1.25c), suggesting that the initial energy provided by the incoming product jet is sufficient to initiate a stable combustion in the nearfield region. These results indicate that the combustion in the developed region is very sensitive to the coflow composition but is less influenced by the incoming hot product jet composition. Expectedly, the unburned hot fuel in the incoming jet (figure 1.25f for Case6) rapidly mixes and reacts with the available oxidizer, establishing diffusion flames within the main jet surrounded by the premixed flames. However, the heat release by the diffusion flame has little effect on the overall behavior of the surrounding premixed flame. The low temperature incoming jet in Case5, also, slightly affects the growth rate of the combustion zones.

To qualitatively compare the flow and flame, the time and spanwise averaged values of temperature, $\langle \overline{T} \rangle_s$, for all six cases are illustrated in figures 1.26(a) and (b) versus the cross-stream direction, ζ , at two streamwise locations, $\xi_1 = 3$ and $\xi_2 = 15$. It can be observed in figure 1.26(a) that in the nearfield region the temperature profiles are nearly the same for the cases with similar incoming jet thermo-chemical conditions (Case1-4). However, figure 1.26(b) shows that the temperature profiles develop very differently for cases with different coflow and incoming jet conditions. In the nearfield region, the maximum temperature located at the jet centerline is lower for cases with lean and rich initial mixtures. The temperature profiles in the shear layers seem to be dependent more on the coflow composition than the incoming jet. Close examination of the results in figure 1.26 indicates that the

maximum temperature decreases much more in Case1. This shows that the mixing with cooler coflow has more effect on temperature than the weak combustion in Case1. The maximum temperature value in Case6 does not drop significantly, indicating that the non-premixed combustion inside the jet zone sustains the jet temperature at a high level. Among the cases with different coflow compositions, expectedly, the maximum temperature of Case4 is higher than the others and the maximum temperature for Case1 is the lowest. But the maximum temperature stays almost the same in Case5.

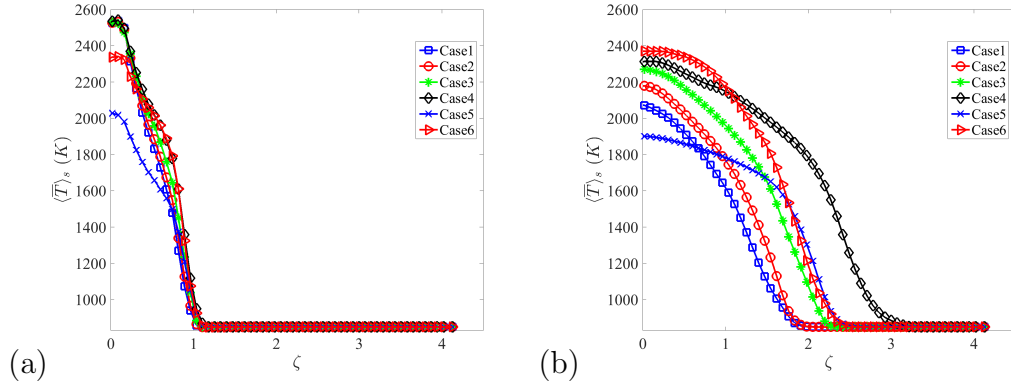


Figure 1.26: Time and spanwise averaged temperature values, $\langle \bar{T} \rangle_s$, at (a) ξ_1 and (b) ξ_2 versus cross-stream direction, ζ , for all cases represented by (\square) Case1, (\circ) Case2, ($*$) Case3, (\diamond) Case4, (\times) Case5, and (\triangleright) Case6.

The overall effects of the coflow and incoming jet conditions are explored more in figure 1.27, which shows the mean and confidence intervals of $y - z$ plane and time averaged temperature, $\mu(\langle \bar{T} \rangle_{yz}) \pm \sigma(\langle \bar{T} \rangle_{yz})$, versus streamwise direction for all simulated cases. The time averaged statistics are calculated based on the simulated data for a sufficiently long time, $17\tau_0$. The coflow data are excluded in this figure, but the preheated zones of the premixed flame zones are included, which, potentially, lower the mean temperature values. Evidently, the plots associated with the nearfield region are very similar for Case1 to Case4, which shows the importance and dominance of the incoming jet hydrodynamics and its mixing with the

coflow. Similar behavior can be observed for Case5 and Case6, even though the incoming jet temperatures are generally lower in these two cases. The transition from the nearfield region to the developed region approximately starts at $\xi \approx 3$. In the developed region, the averaged temperature values continuously decrease along the jet but with much higher rate in Case1 with equivalence ratio of 0.1 than compared to those in Case4 with equivalence ratio of 0.5. This shows the existence of weaker and lower temperature combustion in Case1. Case5 with a lean initial mixture, $\phi_{i,j} = 0.5$, exhibits rather different trend in comparison with other cases. For this case, the averaged temperature starts with a considerably lower initial value then increases in the developed after a sudden drop in the nearfield region reaching to a plateau further downstream. Comparison between Case5 and Case3 indicates that, even though the flow and combustion are similar in the nearfield region, the overall temperature is lower in Case5 since the temperature of the incoming jet is lower. In the developed region of Case6 with a rich initial mixture, $\phi_{i,j} = 2.0$, the averaged temperature profile plateaus after a small increase, which is similar to Case5 but is for different reasons. The incoming jet temperature in Case6 is lower than that in Case3, but unlike the Case5, the averaged temperature eventually becomes higher than that in Case3. Expectedly, the unburned hot fuel inside the incoming jet reacts with the remaining oxidizer of the lean coflow premixed combustion, creating a stable diffusion flame in the hot product jet zone. The non-premixed combustion, can also be observed in figure 1.25(f), where the temperature inside the combustion zones is shown to be much higher. The diffusion flame, evidently, increases the averaged temperature even higher than that in case3, despite the same coflow conditions.

It has been suggested in reference [109] that the thermal half width jet, D_{half} , in TJI-assisted combustion, can be computed based on the peak root mean square (rms) of temperature, $T_{rms} = (\overline{T^2} - \bar{T}^2)^{1/2}$, since high temperature variations usually occur at the flame

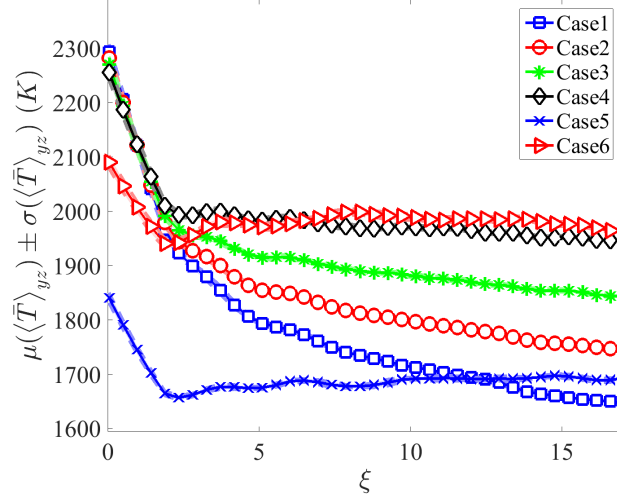


Figure 1.27: Mean and confidence intervals of $y - z$ plane and time averaged temperature, $\mu(\langle \bar{T} \rangle_{yz}) \pm \sigma(\langle \bar{T} \rangle_{yz})$, in the combustion zones versus streamwise direction, ξ , for all cases represented by (\square) Case1, (\circ) Case2, ($*$) Case3, (\diamond) Case4, (\times) Case5, and (\triangleright) Case6.

zone. Figure 1.28(i) shows the T_{rms} contours for Case3 in the mid plane. High value T_{rms} zones also exist in the nearfield region which represent the averaged location of relatively thick premixed/diffusion flames in this region. However, the focus here is the premixed flames in the developed region and the expansion of combustion zones under various coflow and incoming jet conditions. D_{half} is measured, simply, by fitting a straight line (dashed black line shown in figure 1.28(i)) to the local maximum T_{rms} values. Figure 1.28 shows the streamwise variations of thermal half width jet normalized by the incoming jet width, D_{half}/D , for different cases. The maximum and minimum D_{half} values correspond to Case4 and Case1, with the highest and the lowest coflow equivalence ratios. Evidently, for Case3, Case5, and Case6, D_{half} , unlikely change significantly by changing the thermo-chemical properties of the incoming jet. Nevertheless, D_{half} for Case6 is slightly greater than that for Case3, which suggests an insignificant effect of the diffusion combustion on D_{half} . It can be concluded that D_{half} is mainly controlled by the premixed combustion. For the conditions

that the premixed flames are located far away from the incoming jet, D_{half} is unlikely to be affected by the interactions with the incoming jet turbulence.

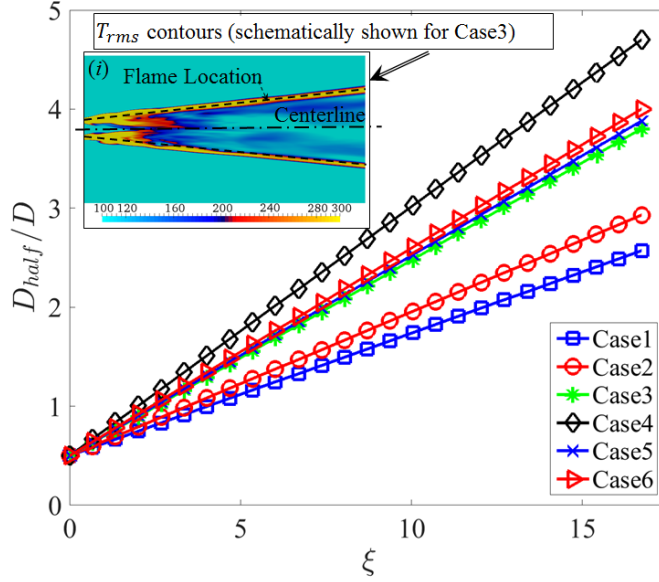


Figure 1.28: Normalized thermal half width jet by the incoming jet width, D_{half}/D , versus streamwise direction (ξ). (i) Contour of rms of temperature, T_{rms} , at the middle spanwise plane, ($z = 1.5D$), schematically shown for Case3.

1.6.1 Flame variable for TJI-assisted

Our primarily analysis of TJI-assisted combustion in TPJ configuration reveal that this type of combustion involves a wide range of premixed to diffusion (non-premixed) flames. To classify the TJI-assisted combustion regimes and flames under various conditions, a suitable flame variable needs to be defined. The premixed flame developed in this type of combustion systems is, essentially, a reacting "wave" initiated by the hot jet in the nearfield region which propagates into the unburned mixture or coflow. The basic parameter, known as the progress variable, in analyzing the standard premixed flames is defined as

$$c_{premixed} = \frac{T - T_f}{T_b - T_f}, \quad (1.14)$$

where T_f and T_b represent the flame and burned zone temperatures, respectively. The progress variable is conventionally set to zero and one in the unburned mixture and burned gas zones, respectively. The intermediate values are associated with the flame sheet. However, in the lean TJI-assisted combustion the maximum temperature is normally associated with the incoming hot jet and not necessarily the burned gases in the premixed flame zone. Therefore, the standard definition (equation 1.14) of the progress variable is not very useful valid for our analysis; the flowfield information concerning the local, incoming jet, and coflow temperatures must be included.

The challenge of defining a progress variable for TJI-assisted combustion also arises from the coexistence of diffusion and premixed flames. This phenomenon, the simultaneous existence of premixed and non-premixed combustion regimes, occurs in the cases that the burned product jet contains extra fuel (i.e. $\phi_{i,j} > 1$ for Case6), in which the unburned hot fuel inside the incoming jet gets mixed and reacts with the remainder of lean premixed combustion oxygen. In the TJI-assisted combustion systems, the fuel and air streams are getting exposed to each other mostly in the hot product jet zone (the non-premixed flames can occupy a significant part of this zone) confined by the premixed flame, instead of a flame sheet as normally seen in "standard" diffusion flames.

Consequently, the flame location and strength can be controlled by the hydrodynamics and thermo-chemical conditions of both the incoming jet and the coflow. The fuel and oxidizer feed the flame at different rates during the transition from the oxidizer in the burned-mixed zone to the fuel side in the hot product jet zone. Since this type of flames is mainly characterized by the inter-penetration of fuel and oxidizer, conveniently, a tracer of the mixture state is introduced based on the combination of transport equations of those two streams. One may argue that since the products exist in both fuel and oxidizer streams of the

non-premixed regime of the TJI-assisted combustion, a proper alternative definition of the mixture fraction might be based on the elemental conservation equations. But the combination of the fuel, oxidizer, or elemental transport equations is derived with the equi-diffusional approximation, which, ultimately, suppresses the effects of the temperature. Figure 1.29(a) shows the mean and confidence intervals of temperature in the combustion zones versus elemental mixture fraction (based on element H), $f = \frac{Z_H - Z_{Hj}}{Z_{Hco} - Z_{Hj}}$, for all 6 cases provided in table 1.1. Where $Z_H = \sum_{\alpha=1}^{N_s} \frac{a_H W_H}{W_\alpha} \phi_\alpha$, $Z_{Hco} = \sum_{\alpha=1}^{N_s} \frac{a_H W_H}{W_\alpha} \phi_{\alpha co}$, and $Z_{Hj} = \sum_{\alpha=1}^{N_s} \frac{a_H W_H}{W_\alpha} \phi_{\alpha j}$ are local, coflow, and the incoming jet elemental mass fractions. a_H is the number of element H with molecular weight W_H in species α with molecular weight W_α . The poor performance of f is evident as for a fixed f value various temperature values are predicted and the effects of the jet and coflow can not be distinguished. Hence, TJI-assisted progress variable not only has to trace the fuel and air streams, but also has to include the temperature effects, in a functional form like $\mathcal{R} \approx g(T, T_j, T_{co})h(\phi_{fuel}, \phi_{oxidizer})$. Based on the above argument, here, we define a normalized \mathcal{R} such that it represents both the mixture and the temperature effects as

$$\mathcal{R} = \left(\frac{T_j - T}{T_j - T_{co}} \right) \phi, \quad (1.15)$$

where ϕ is the local equivalence ratio. Figure 1.29(b) presents the mean and confidence intervals of temperature in the combustion zones versus \mathcal{R} for all 6 cases. At both sides of each plot, \mathcal{R} values describe the associated combustion zone conditions such as if $T \rightarrow T_{co}$ then $\mathcal{R} \rightarrow \phi_{co}$, which represents the preheated zone of the premixed flow inside the coflow. The straight line with negative slope shows the transition of the flow from unburned fresh coflow to the burned-mixed zone passing through a premixed flame. At the other side of flow if $T \rightarrow T_j$ then $\mathcal{R} \rightarrow 0$, which represents the hot product jet zone. In the cases with

extra fuel in the incoming jet, ϕ_j contributes to \mathcal{R} , resulting in small but greater than zero \mathcal{R} values, i.e. $T \rightarrow T_j$ then $\mathcal{R} \rightarrow \phi_j$, which essentially identifies the diffusion flames. The intermediate \mathcal{R} values represent the burned-mixed zone.

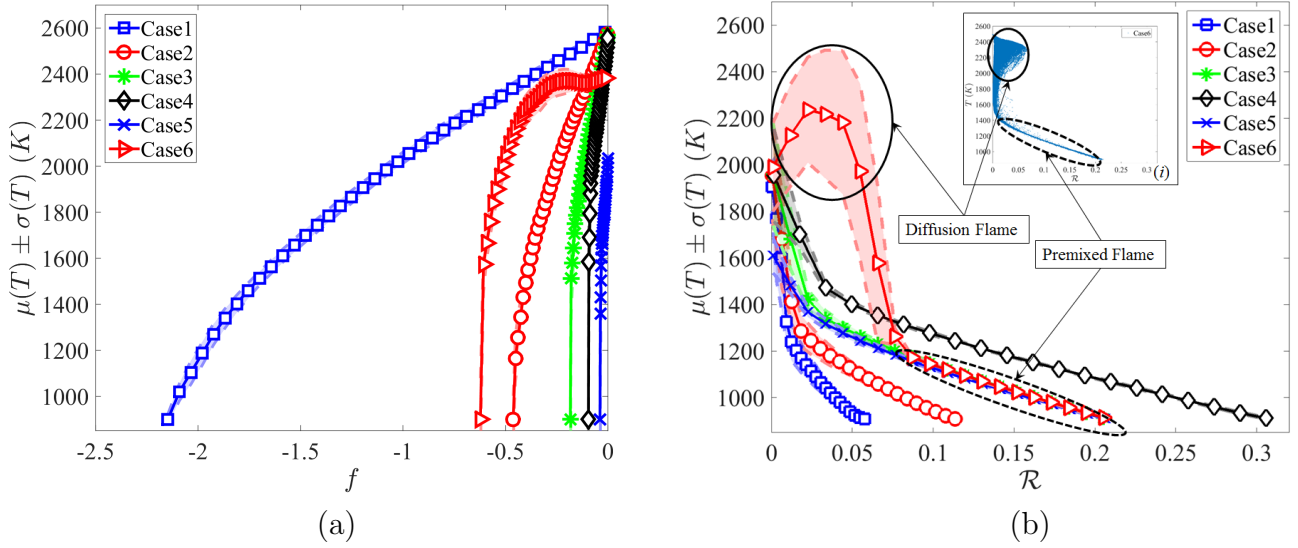


Figure 1.29: Mean and confidence intervals of temperature, $\mu(T) \pm \sigma(T)$, in the combustion zones at $t = 17\tau_0$ versus (a) elemental mixture fraction, f and (b) TJI combustion progress variable, \mathcal{R} , for all cases represented by (\square) Case1, (\circ) Case2, (\ast) Case3, (\diamond) Case4, (\times) Case5, and (\triangleright) Case6. (i) Scatter plot of temperature, T , in the combustion zones at $t = 17\tau_0$ versus TJI combustion progress variable, \mathcal{R} , for Case6, identifying the simultaneous existence of the premixed and non-premixed combustion regimes.

To further examine the performance of \mathcal{R} in identifying various flame types and combustion zones, the instantaneous values of \mathcal{R} at two streamwise locations, ξ_1 and ξ_2 , at the latest time, $t = 17\tau_0$, versus cross-stream direction are plotted in Figures 1.30(a) and (b) for all cases. It can be observed in figure 1.30(a) that in the nearfield region at ξ_1 , \mathcal{R} values are very small inside the jet for Case1 to Case5, but substantially increase in the premixed flame zone all the way to the coflow and stay constant equal to the correspondent coflow equivalence ratios. Different behavior is observed for Case6; the initially large values of \mathcal{R} are due to extra amount of fuel which creates diffusion flames in the inner jet. Moving forward in the streamwise direction (figure 1.30b), similar behaviors are expected for Cases1-5, and less

intense diffusion flames for Case6. Interestingly, the sharp transitions from the combustion zones to the fresh unburned coflow in the premixed flame zone is captured by sudden increase in \mathcal{R} values, confirming the ability of \mathcal{R} in locating the premixed flames in the scalar space.

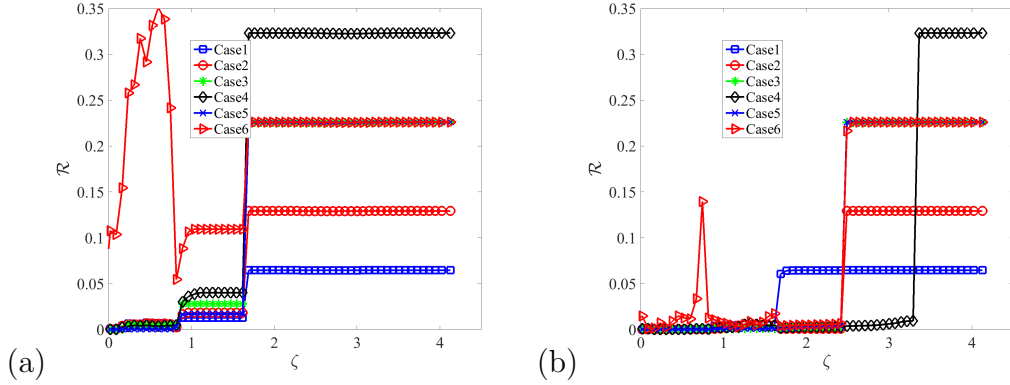


Figure 1.30: TJI combustion progress variable, \mathcal{R} , versus cross-stream direction at a middle spanwise plane, ($z = 1.5D$), and $t = 17\tau_0$ at (a) ξ_1 and (b) ξ_3 versus cross-stream axis, ζ , for all cases represented by (\square) Case1, (\circ) Case2, (\ast) Case3, (\diamond) Case4, (\times) Case5, and (\triangleright) Case6.

In the next section, the effects of coflow equivalence ratio on the flow/flame including the localized flame extinction and re-ignition in ultra-lean mixtures are examined. Changes in the coflow condition significantly affect the flame structure and its interactions with the turbulence.

1.6.2 Coflow composition effects

The spatial distributions of various species in the simulated TJI-assisted TPJ have been examined in details in order to develop a better understanding of premixed flame interactions with the turbulence for different conditions in the TJI-TPJ. The fuel mass fraction contours (not shown here) are similar to the temperature contours in figure 1.25, generally showing the similarity of the jet and combustion in the nearfield region and the very significant difference in the developed region regarding the flame propagation and jet structure. More

details of the flow/flame can be extracted from other species like H_2O , O_2 , OH , and H . Figures 1.31(a)-(d) illustrate the instantaneous H_2O mass fraction contours for Case1 to Case4. Since the incoming jet conditions are the same in these four cases, the ϕ_{H_2O} contours stay somewhat similar in the nearfield regions. The produced H_2O species during the lean premixed combustion are added to the initial values in the developed regions. Expectedly, the ϕ_{H_2O} are produced more in cases with higher coflow equivalence ratio. In Case1, the generated water is small, making the mixing of hot product jet with cooler coflow (not the combustion) the dominant process. Where the high ϕ_{H_2O} values in the hot product jet are, considerably, diluted through the mixing with the zero level ϕ_{H_2O} coflow, exhibiting qualitatively similar behavior to the temperature contours in figure 1.25(a). By increasing the equivalence ratio in Case2, Case3, and Case4, flame sheets with considerably higher ϕ_{H_2O} levels appear within the jet with consistently greater jet growth rate in later cases. In the developed region of Case4, three areas are distinguishable with ϕ_{H_2O} levels of 0.22, 0.17, and 0.0 in the main hot product jet zone, burned-mixed zone, and coflow. The vague transition from the burned-mixed zone to the coflow confirms that the flame zone can not be identified by H_2O , even though the turbulent mixing and highly fluctuating nature of the premixed flame can be observed in the ϕ_{H_2O} contours. The O_2 mass fraction contours (not shown here), while have an opposite behavior of H_2O contours, also indicate that the flame front can not be captured by O_2 .

In the standard premixed flames, OH radical is often used for identifying the flame zone [64, 111, 13]. Figures 1.32(a)-(d) show the OH mass fraction contours for four simulated TJI-assisted TPJ cases. As it can be observed in these figures, OH radicals produced by the combustion (very intensively in the nearfield region and less intensively in the developed region) add up to the initial OH of the incoming product jet, causing the maximum ϕ_{OH}

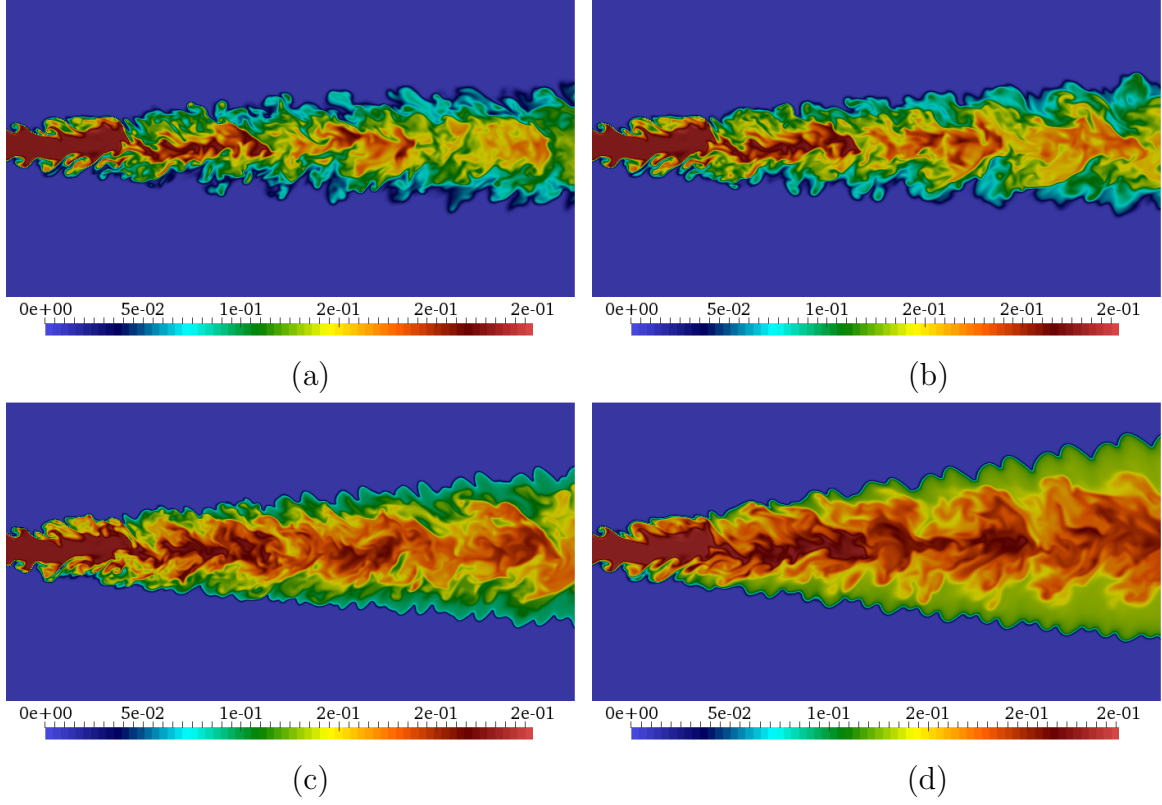


Figure 1.31: Instantaneous contours of the H_2O mass fraction, ϕ_{H_2O} , at a middle spanwise plane, $z = 1.5D$, and $t = 17\tau_0$ for (a) Case1, (b) Case2, (c) Case3, and (d) Case4. (Note that the scale limits are set to the available values in each contour and are not the same.)

to occur somewhere in the hot product jet and not at lean premixed flame front. The OH generation in Case1 and Case2, due to weak combustion of the ultra-lean coflow mixtures, in such an extent is relatively small. The local maximum values of ϕ_{OH} in the nearfield region are considerably larger than those in the developed region. Expectedly, the OH level in Case3 and Case4 increase, on average, due to more stable and stronger combustion. Figures 1.32(c) and 1.32(d) show that ϕ_{OH} values are also, locally, higher in the flame zone than those in the immediate surroundings. Thus, while OH might be a fair indicator of flame when the combustion is strong enough, and it may not be able to locate the flame front and also extincted flames in ultra-lean mixtures. Other radicals such as H in hydrogen combustion or CH in hydrocarbon combustion are potentially more helpful.

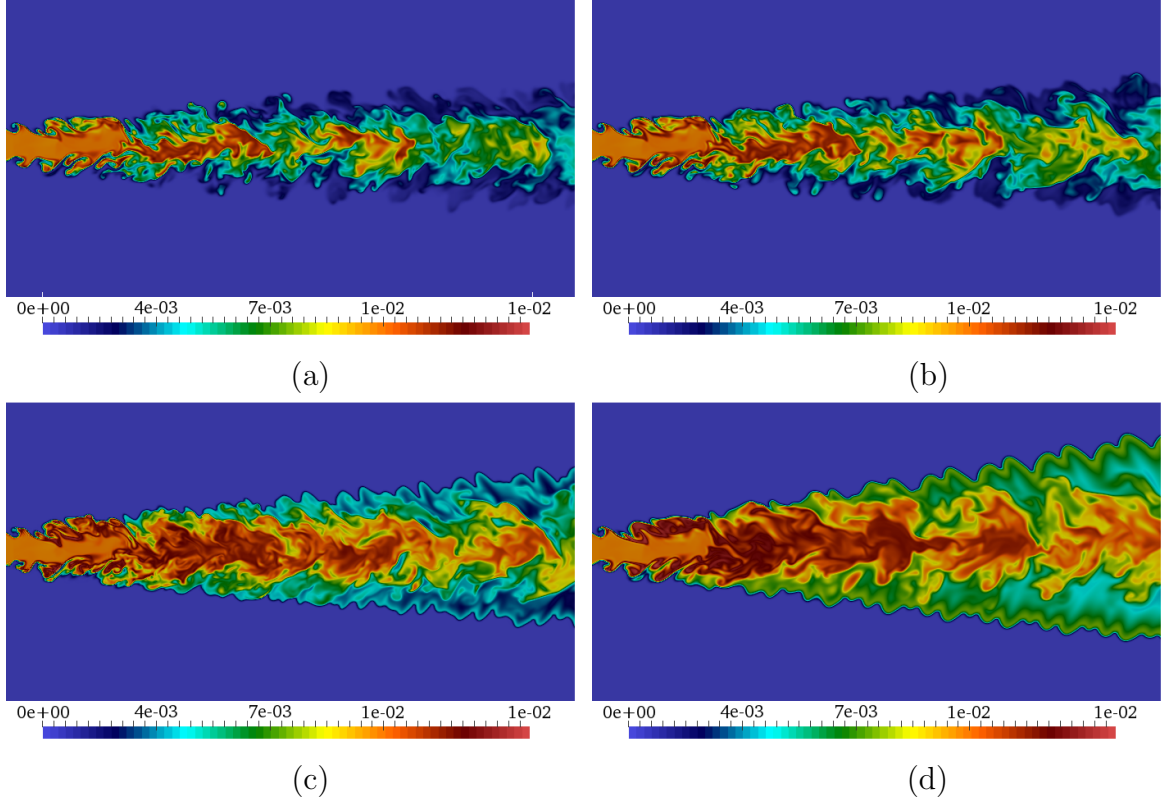


Figure 1.32: Instantaneous contours of the OH mass fraction, ϕ_{OH} , at a middle spanwise plane, $z = 1.5D$, and $t = 17\tau_0$ for (a) Case1, (b) Case2, (c) Case3, and (d) Case4.

Figures 1.33(a)-(d) present the contours of H mass fraction for Case1 to Case4. It can be observed that, interestingly, the maximum value of ϕ_H occurs right at the flame front while its value inside the incoming jet, in contrast to ϕ_{OH} , is relatively low. This behavior suggests that the radical H may be used as an accurate flame marker in TJI-assisted TPJ combustion. Note that the contour color maps in figures 1.33(a)-(d) are scaled differently to the range of data for better capturing of H radical behavior. For all coflow mixture fractions considered in this study, the high values of ϕ_H occur at the edges of the incoming jet in the nearfield region as shear layers develop and generate relatively thick flames. In the developed regions of Case2, Case3, and Case4, ϕ_H values maximize at the flame front and drop to very low values in the burned-mixed and hot product zones. In Case1, where the localized flame

extinction occur, similar trend is observed but with much smaller local maximum ϕ_H values at the flame front. It has been shown in [109] that H radical mass fraction values are well correlated with the heat of reaction, especially, in the developed regions.

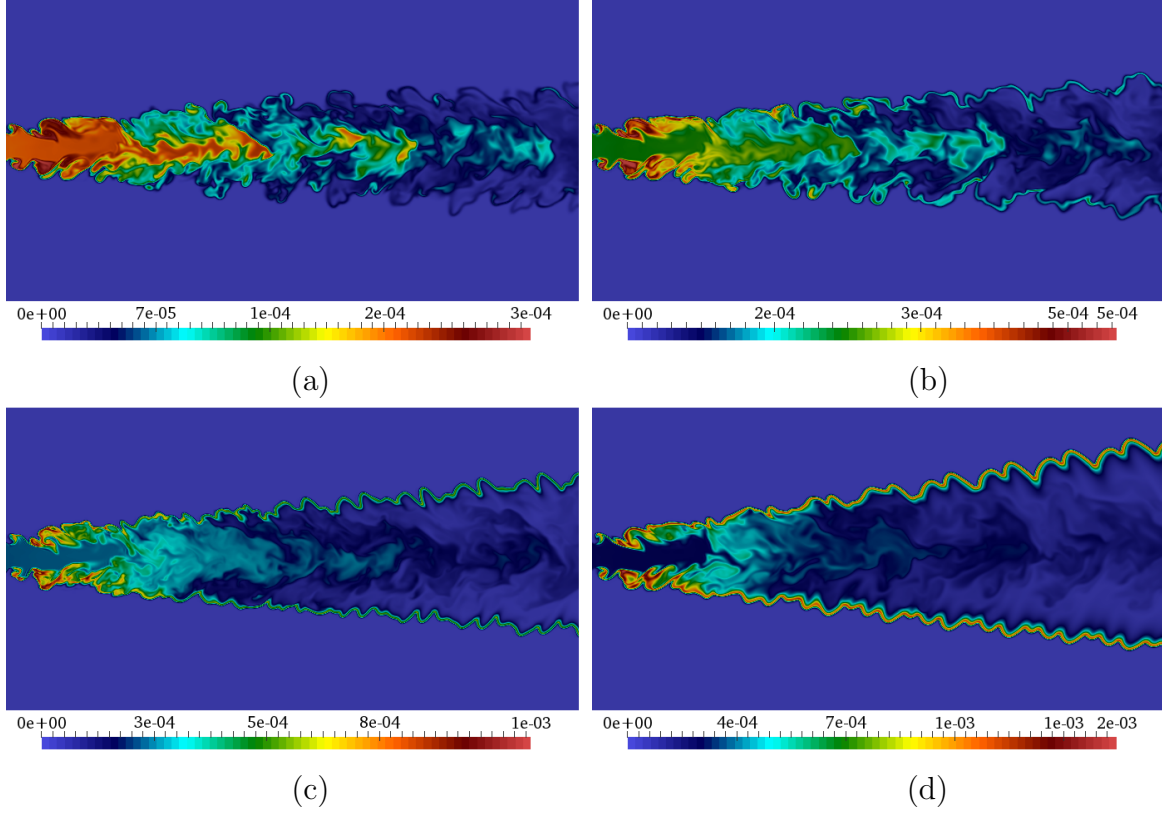


Figure 1.33: Instantaneous contours of the H mass fraction, ϕ_H , at a middle spanwise plane, $z = 1.5D$, and $t = 17\tau_0$ for (a) Case1, (b) Case2, (c) Case3, and (d) Case4. (Note that the scale limits are set to the available values in each contour and are not the same.)

The combustion heat release rate, \dot{Q}_e , is an important quantity to discern flames and their locations in turbulent reacting flows such as the TJI-TPJ. The spatial distribution of \dot{Q}_e is highly dependent on the flame-turbulence interactions as well as the chemical reaction. Despite the significance of \dot{Q}_e , measuring it is challenging [75, 71]. Here, \dot{Q}_e is, conveniently, obtained by equation 1.9 [69]. Figures 1.34(a)-(d) show the instantaneous contours of heat release rate for four cases with different coflow equivalence ratios. The process of flame-turbulence interactions and mixing of the incoming hot jet with cooler premixed coflow in

the nearfield region at the reacting shear layers creates relatively thick and geometrically complex flames in the TJI-TPJ. The nearfield region of TJI-assisted TPJ combustion might be similar to the corrugated and distributed burning zones in standard premixed flames, where the intense turbulence generates eddies strongly coupled with the combustion process, thickening the flame zone while the flame front being wrinkled. It is expected that the eddies generated in the nearfield region are in the tail of the energy spectrum such that their lifetime is very short and their impacts on the combustion zones in the developed region are thus limited. It is observed that the distributed reaction and high heat release rate values virtually vanish from the main jet as the flow transients from the nearfield to the developed regions. Moving in the streamwise direction, a spatially continuous, distorted, and concentrated flame is developed. While the premixed flame moves away from the incoming turbulent jet and propagates into the coflow, it becomes thinner and much less affected by the jet turbulence. The \dot{Q}_e contours shown in figures 1.34(b)-(d) clearly show the separation of the unburned and burned-mixed zones in the developed region in the cross-stream direction and the relatively thin distorted premixed turbulent flame zone. Even though the flame and turbulence features vary over time, they appear to be well stabilized in the developed region, particularly, in Case2, Case3, and Case4. The heat release contours shown in figures 1.34(a), consistent with H , illustrates relatively high and low (close to zero) \dot{Q}_e values along the flame front. It indicates that the coflow composition lays on the lower flammability limits of hydrogen-air mixtures. The lean (lower) flammability equivalence ratio for hydrogen-air mixture at $T = 359 \text{ (K)}$ is reported to be 0.14 [119]. Considering that the coflow temperature in Case1 is higher than that considered in experimental measurements of low flammability limits and since the fuel-air mixtures are continuously exposed to a high temperature jet, it is not surprising that the TJI-assisted combustion has a much lower lean flammability limits

than the standard premixed combustion.

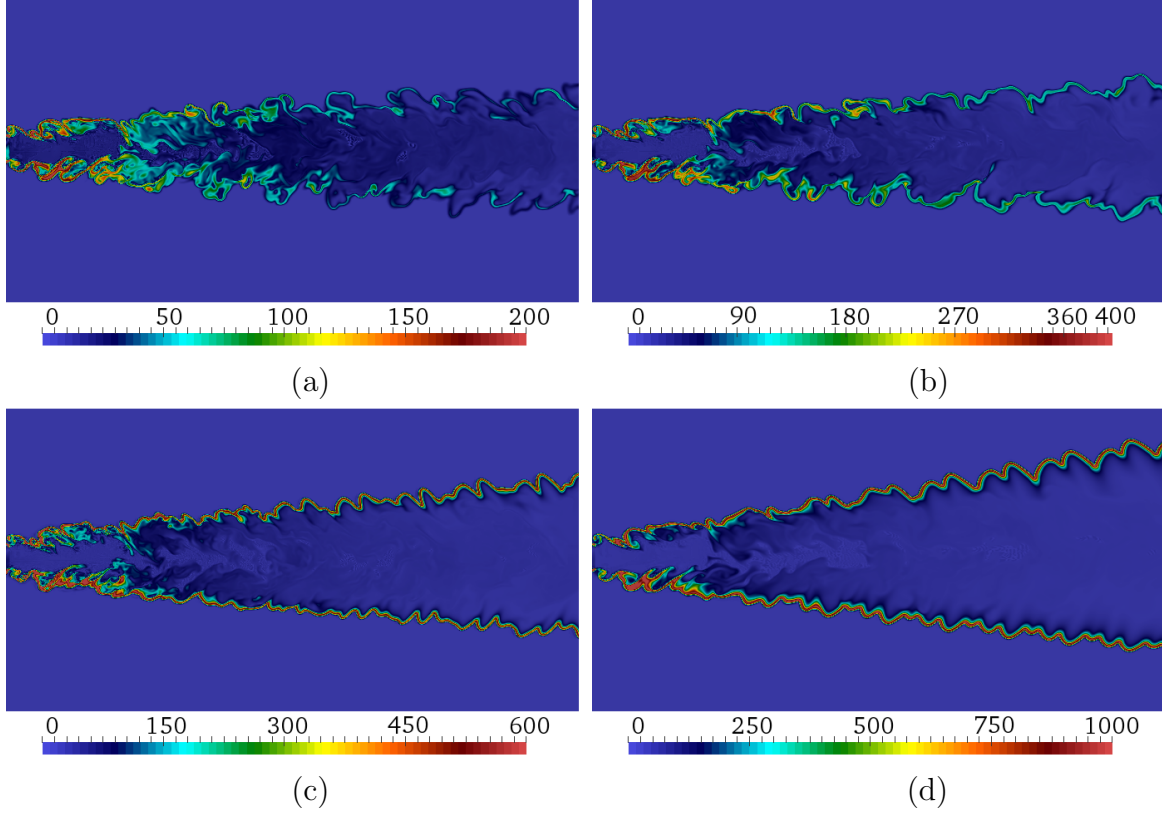


Figure 1.34: Instantaneous contours of the heat release rate, \dot{Q}_e (W), at a middle spanwise plane, $z = 1.5D$, and $t = 17\tau_0$ for (a) Case1, (b) Case2, (c) Case3, and (d) Case4. (Note that the scale limits are set to the available values in each contour and are not the same.)

In figure 1.35 the mean and confidence bounds of the $(y - z)$ plane averaged heat release rates, $\mu(\langle \dot{Q}_e \rangle_{yz}) \pm \sigma(\langle \dot{Q}_e \rangle_{yz})$, are plotted versus streamwise direction. The amount of combustion heat is, expectedly, increased by the coflow equivalence ratio. Nevertheless, in all cases the averaged heat is generated the most at the end of the nearfield region. Clearly, the heat release peaks are different but occur almost at the same streamwise location in all cases. This suggests that significant autoignition happens at all coflow equivalence ratios where the residence time is large enough, even though the combustion is already initiated at the shear layers. This confirms the dominance of the incoming jet hydrodynamics in this region. Surely, different behaviors are expected for various jet hydrodynamics. In the

developed region, descending heat release can be observed for all cases indicating cooling of the combustion zones. However, they converge to different values with different rates. In case1, $\langle \dot{Q}_e \rangle_{yz}$ reaches to nearly zero at the end of the computational domain, indicating a very weak combustion and significant extinction.

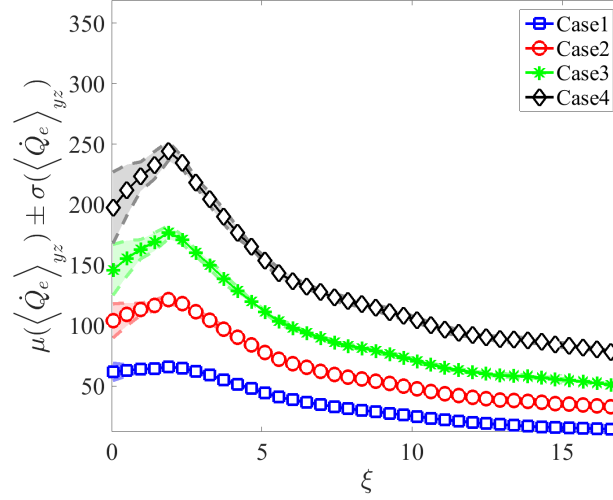


Figure 1.35: Mean and confidence intervals of $y - z$ plane averaged heat release rate, $\mu(\langle \dot{Q}_e \rangle_{yz}) \pm \sigma(\langle \dot{Q}_e \rangle_{yz})$, at $t = 17\tau_0$ versus streamwise direction, ξ , for four cases represented by (\square) Case1, (\circ) Case2, ($*$) Case3, and (\diamond) Case4.

The flame stability and extinction depend on the volumetric heat loss from the flame in comparison to its heat (energy) release. Heat loss is relatively significant, particularly, close to the lean flammability limit condition. In figure 1.36, the contours of \dot{Q}_e are shown again for the ultra lean coflow. In this figure, the scaled flow/flame fields in the developed region where the flames locally extinct and re-ignite are also shown. The local extinction and re-ignition flame events are illustrated by \odot and \bullet , respectively. The flame stretching and folding, induced by the mean velocity gradient and the small-scale turbulence, change in time and space over the premixed flame surface. If the stretching increases locally, the space between the both sides of the flame decreases, leading to the local flame extinction and incomplete combustion. The local flame extinction events are seen to be accompanied

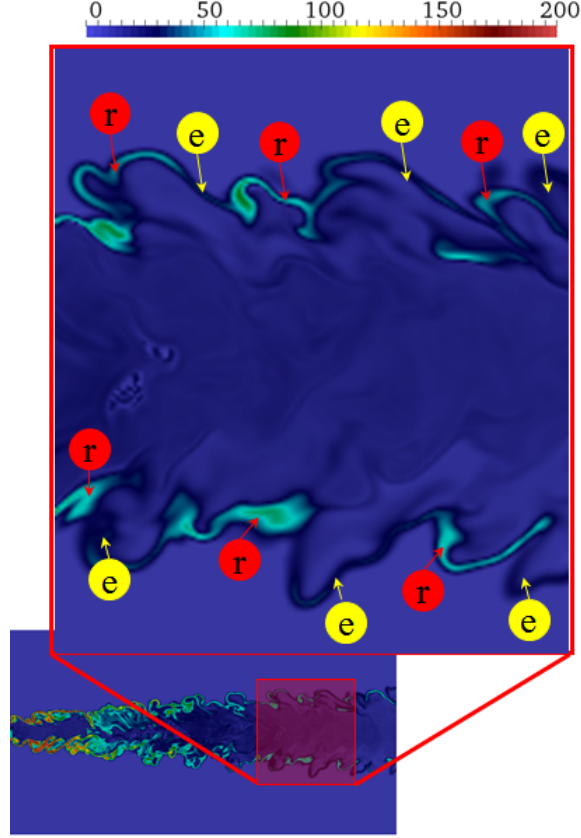


Figure 1.36: Localized extinction and re-ignition at flame sheet identified based on heat release and a magnified view of them by a factor of 5:1, occurred in ultra-lean coflow (Case1).

by a large drop in heat release even to values close to zero. As observed in the magnified image, when the flame front gets further away from the hot incoming jet, more local flame extinction events occur. Also, more re-ignition events are seen at the locations close to the hot product jet zone, where relatively high heat release values reappear among the extinct flame zones. These confirm that in situations where the premixed flame is close to the hot product jet, the intense interactions and heat transfer from the incoming jet helps the flame to re-ignite after extinction. As long as the flame front is connected, lean coflow mixtures stay largely separated from the flame front and hot product inside burned-mixed zone. However, a sequence of localized extinction and re-ignition occurs across the flame, indicating discontinuities in the flame for ultra lean mixtures. When the flame front is

interrupted, the combustion induced high-viscosity dilatation layer is no longer present to form a barrier for high temperature turbulent eddies, hence, they can escape through the holes in the flame zone and diffuse into the coflow. The mixing of the diffused hot products with coflow increases the temperature of the preheated zone of the premixed flame at the coflow side that may subsequently lead to re-ignition.

To better understand the local extinction and reignition in ultra lean mixture, the scatter plots of \dot{Q}_e versus \mathcal{R} are shown in figure 1.37 for Case1 to Case4. The results for various parts or sections of the flow are included such that Sec1, (\square), represents the nearfield region $0 \leq \xi \leq 4$, Sec2, (\diamond), represents the initial part of the developed region $4 \leq \xi \leq 10$, and Sec3, ($*$), represents the end part of the developed region $10 \leq \xi \leq 17$. The results in figure 1.37 basically show the compositional flame structure. The general behavior in this figure is that the maximum heat release happens at \mathcal{R} values corresponding to the flame front, i.e. $\mathcal{R} = 0.02, 0.04, 0.065$, and 0.1 . The areas with greater than these values correspond to the preheated zone of the premixed flame zone. The areas with smaller \mathcal{R} values represent either the hot product zone or the burned-mixed zone. The relative extent of scatter in the $\dot{Q}_e - \mathcal{R}$ plot also show the extent of local extinction in the flow. The very wide scatter of $\dot{Q}_e - \mathcal{R}$ data in the ultra lean mixture in Case1 indicates that the finite rate chemistry effects are very important and the local heat loss is more than the heat release and stable continuous flame zones can no longer be maintained. This is more clear when the data in different sections of the flow are compared. The flame behavior changes in the streamwise direction from a significantly thick premixed flame in the nearfield region to a localized thin extinguished-reignited flame in the developed region in Case1. Consequently as shown in figure 1.37(a), the flame is stable and continuously provides sufficient amount of heat. This is represented by high \dot{Q}_e values of low \mathcal{R} s and is also supported by H and \dot{Q}_e contours in

figures 1.34(a) and 1.33(a). Moving in the streamwise direction to Sec2, lower \dot{Q}_e values at a given \mathcal{R} become more significant. In Sec3 the extinction is dominant and scatter in data is important in all flame regions. A similar (but less intensive) behavior is shown in figure 1.37(b) for Case2. For case3 and Case4, the relatively narrow band of scatter in the $\dot{Q}_e - \mathcal{R}$ data in all sections supports the existence of strong, continuous, and stable premixed combustion. It should be added here that as it can be seen in figure 1.25(a), the temperature variations between the locally extincted and re-ignited flames are insignificant, unlike the standard turbulent premixed flames, which normally have low flame temperature in regions with significant flame extinction.

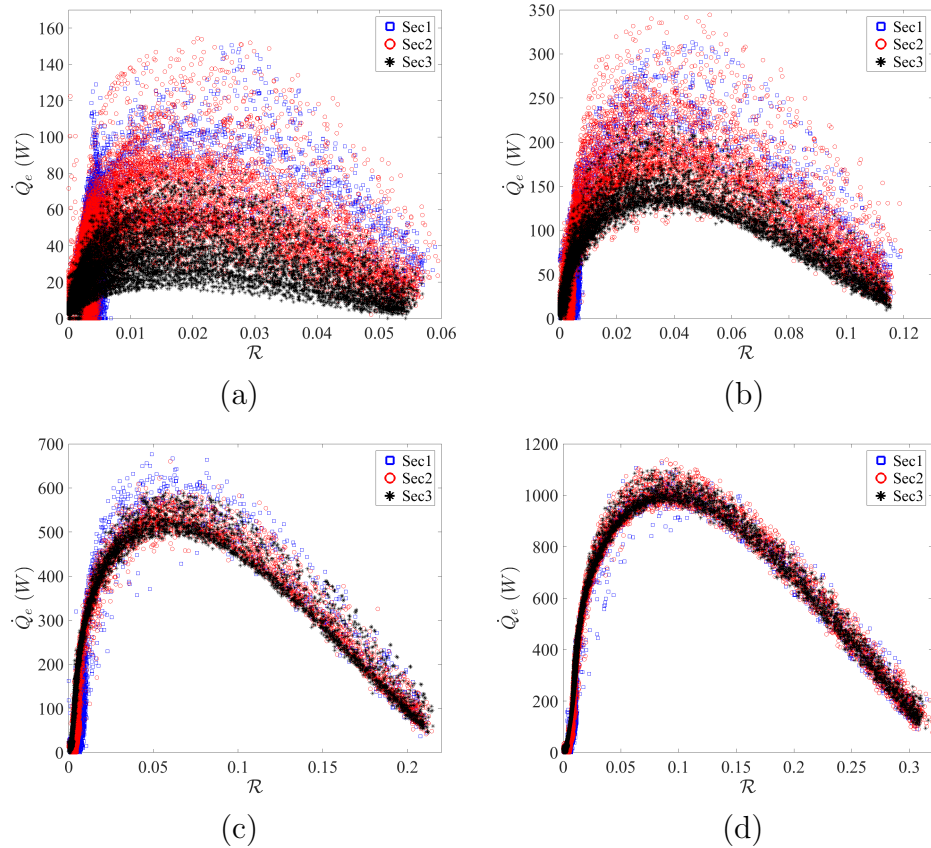


Figure 1.37: Scatter plot of the heat release rate, \dot{Q}_e (W), versus TJI combustion progress variable, \mathcal{R} , for (a) Case1, (b) Case2, (c) Case3, and (d) Case4 at different streamwise sections represented by (\square) Sec1, (\circ) Sec2, and ($*$) Sec3.

The effects of turbulence and flow strain rate on the TJI-assisted combustion and flame stabilization are different than those in standard propagating turbulent premixed flames. In the nearfield region, where the strain rate, $\dot{\epsilon}$, is high, the flow residence time is relatively small, which, theoretically, might lead to the incomplete reaction. However, high flow mixing and turbulence level in the nearfield region also facilitates the heat transfer of the hot product jet with the coflow. This overtakes the negative effects of the high strain rate and prevents local extinction in this region. In the developed region, Sec2 and Sec3 in figure 1.38(a), the high strain rate values, in one hand might cause the flame to extinct, but in another hand they help the reignition process by convecting heat to the extincted flames. This process stabilizes the combustion and, eventually, can lower the lean flammability limit. Figure 1.38(a) and (b) present the scatters of the heat release rate (\dot{Q}_e) versus strain rate ($\dot{\epsilon}$) for Case1 and Case4. The scatter data are separated for the three different sections in streamwise locations. Evidently, the heat release rate is unaffected by the strain rate since the magnitudes of strain rate are the same in these two cases, one with and one without extincted flames. Unlike the standard premixed flames, a critical strain rate can not be defined for the TJI-assisted combustion.

Here, the effects of the coflow combustion on the turbulence and vice versa are investigated by considering thermal half width jet, turbulence intensity, and vorticity in figure 1.39. The solid thick lines show the results at maximum rms of temperature, $\max(T_{rms})$, and the dashed thin lines denote those at maximum turbulence intensity, $\max(I)$, where
$$I = \frac{(u'^2 + v'^2 + w'^2)^{\frac{1}{2}}}{U_{ref}} \text{ and } U_{ref} = \frac{U_{co} + U_j}{2} = 300 \text{ (m/s)}$$
 is the average of the coflow and hot product jet velocities. Figure 1.39(a) shows the location of the maximum T_{rms} and I in the cross-stream direction versus the streamwise direction. The maximum T_{rms} can be used to

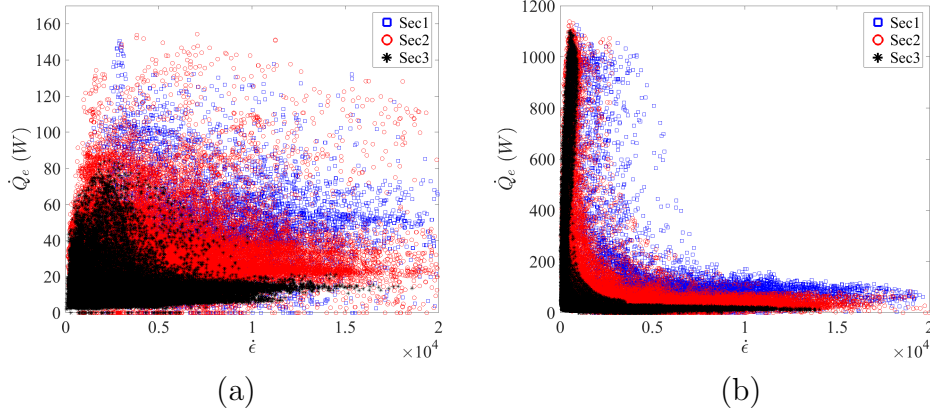


Figure 1.38: Scatter plot of the heat release rate, \dot{Q}_e (W), versus strain rate, $\dot{\epsilon}$ (1/s), for (a) Case1 and (b) Case4 at different streamwise sections represented by (\square) Sec1, (\circ) Sec2, and ($*$) Sec3.

identify the approximated location of the premixed flame and the thermal half width jet in the TJI-assisted combustion as it was shown in figure 1.28(i). The location of the maximum turbulence I , clearly, differs from the location of flame or maximum T_{rms} . This shows that as the premixed flame propagates into the coflow it gets separated from the main jet. It also confirms that the temperature field is not well correlated with the hydrodynamics field in the developed region of the TJI-TPJ [109]. However, the jet span, estimated based on the maximum I , is increasing by increasing the coflow equivalence ratio, since the premixed flame moves further away from the incoming jet, leading to less interactions between these two zones. The smallest jet width corresponds to the Case1 where the premixed flame is very close to the turbulent jet and has the most significant damping effects on the growth of the incoming jet in the cross-stream direction.

The I values at maximum T_{rms} and I locations, versus the streamwise direction are plotted in figure 1.39(b). The I values at these locations are initially almost the same close to jet inlet in all four cases. The small differences might be related to small variations in the coflow density. The I values at flame location or $max(T_{rms})$ in Case4 and Case3 drop rapidly

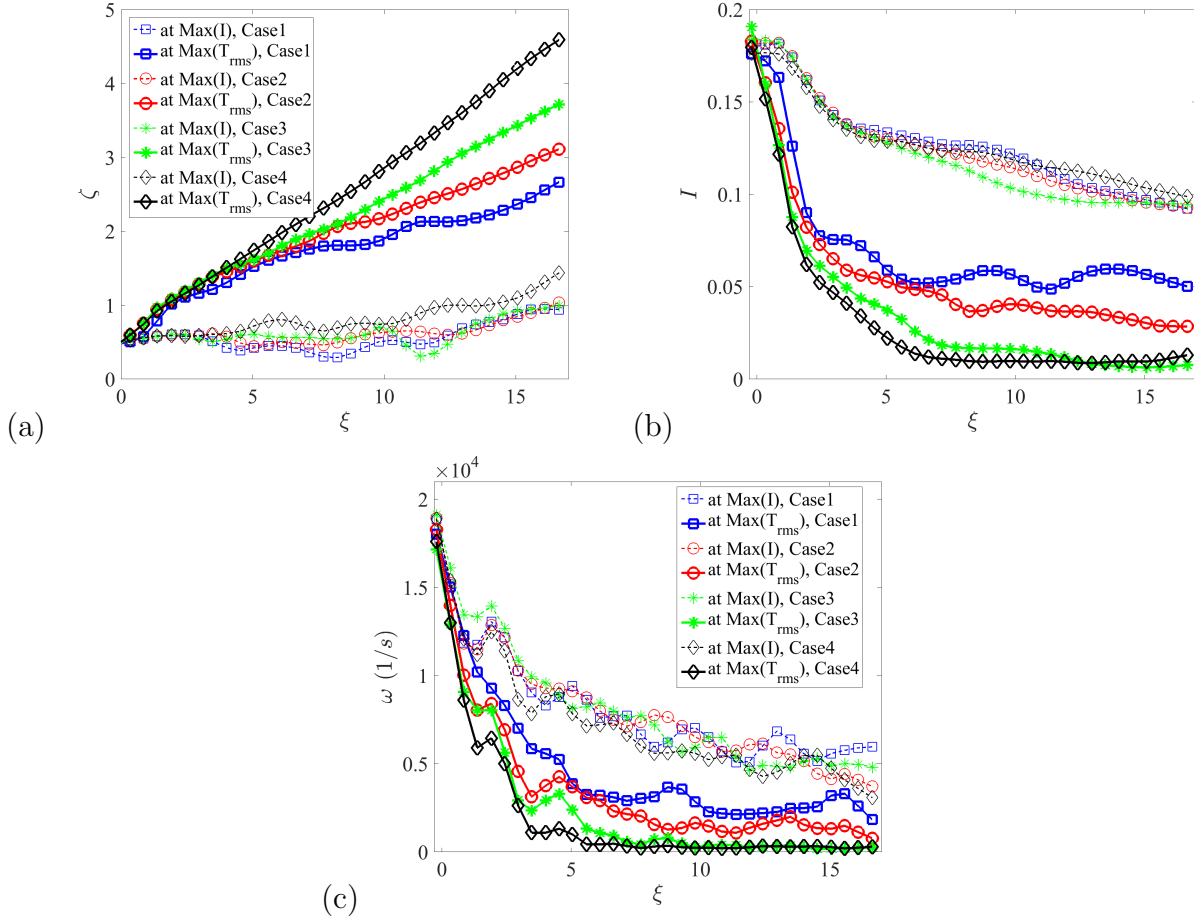


Figure 1.39: (a) Cross-stream location of $\max(T_{rms})$ and $\max(I)$, (b) turbulence intensity, I , values at $\max(T_{rms})$ and $\max(I)$ locations, and (c) vorticity magnitude, ω , at $\max(T_{rms})$ and $\max(I)$ locations, versus streamwise direction, ξ , for four cases represented by (\square) Case1, (\circ) Case2, ($*$) Case3, and (\diamond) Case4. Thick solid and thin dashed lines correspond to $\max(T_{rms})$ and $\max(I)$, respectively.

to very small, close to zero values, due to relatively stronger premixed combustion in these two cases; the higher the coflow equivalence ratio, the lower the I . The higher I values for Case1 and Case2 suggest a stronger interaction of the premixed flame front with the inner jet. The I values at the $\max(I)$ locations similarly decrease in the streamwise direction, however, they are about one order of magnitude higher than those at flame location, which shows the nearly independent behavior of the hydrodynamics. The I values at any locations in the developed region are greater for the cases with higher equivalence ratios, Case4 and

Case3, which, again, confirm the less interactions of the flame with turbulence in these two cases.

In figure 1.39(c), the streamwise variations of vorticity magnitude, $\omega = |\vec{\omega}|$, at maximum T_{rms} and I locations for different cases are compared. The ω levels in the nearfield region are relatively high because of the intense interactions between the incoming jet, thick premixed flames, and turbulence. In the developed region, however, these interaction are less influential on the overall turbulence of the flow. As observed in figure 1.39(c), the vorticity at $\max(T_{rms})$ locations reach to very low values in the cases having very stable and strong combustion (Case3 and Case4); supporting the fact that the combustion has a dissipative effect on turbulence. The simulated hot product jet is highly turbulent with significant flow variable fluctuations at all length (and time) scales, even though the small-scale turbulent structures are depleted by the combustion. High values of ω at maximum I locations indicate that the incoming jet is still effective in the hot product jet zone. In the nearfield region and at $\max(I)$ locations, the vortex stretching and compressibility are the sources of the vorticity production. Further downstream in the developed region, the significant variations in density and pressure cause the Baroclinic torque, $\vec{\beta} = \frac{1}{\rho} \nabla \rho \times \nabla P$, to play a more important role in generating the vorticity. Close to the flame zone at $\max(T_{rms})$ locations, the Baroclinic torque and the vortex stretching are the main sources of generating vorticity. Nevertheless, close to the flame the vorticity field is negatively affected by the reaction because of heat release induced volumetric flow expansion and temperature dependency of viscosity. In the nearfield region, $\vec{\beta}$ is generated mainly due to density difference between the incoming hot jet and coflow and the density/pressure gradient generated in the inner jet core by complex thick flames. In the developed region, however, the dominant mechanisms for the Baroclinic torque generation are the transport and lean premixed combustion in the outer edge of flow.

As reported in [109], vortical structures with the same Baroclinic torque magnitude exist in the flow field, even though the localized maximum β can identify the premixed flame front.

1.6.3 Incoming jet thermo-chemical effects

In this section, the effects of incoming jet thermo-chemical conditions on the TJI-assisted TPJ combustion are investigated considering the results of Case3, Case5, and Case6. In these cases the equivalence ratio of the initial mixture and consequently the incoming jet composition and temperature are different while the coflow conditions are the same. In Case5, the initial mixture equivalence ratio is chosen to be on the lean side with $\phi_{ij} = 0.5$, thus the jet mainly consists of O_2 and H_2O with relatively low temperature of $T_j = 2050$ (K) (tables 1.1 and 1.2). In Case6, the initial mixture considered to be on the rich side so that the incoming jet carries unburned hot fuel along with the products. The main jet species are H_2 and H_2O species with temperature of $T_j = 2350$ (K). The jet hydrodynamic properties are considered to be the same in these three cases.

Figures 1.40(a) and 1.40(b) show the instantaneous OH mass fraction contours at the latest time $t = 17\tau_0$ for Case5 and Case6, respectively. In the nearfield regions of these cases the intense and similar production of OH radical once again show the significance of reaction and strong flow interactions with the combustion. In Case5, the OH mass fraction in the incoming jet is relatively low, around $1.8e-3$ (table 1.2), but high ϕ_{OH} values exist in the developed region, particularly, in the burned-mixed and product jet zones. This level of ϕ_{OH} is mostly due to the products of the nearfield combustion which are transported into the downstream by the turbulent jet. This can be confirmed by the \dot{Q}_e results in figure 1.42, which shows that the heat release in the developed region and the mentioned combustion zones is very small. In Case6, the jet OH mass fraction is equal to $9.9e-4$ which

is the minimum value among all other cases. However, the highest ϕ_{OH} values are seen in the developed region for this case, which is mainly due to the combustion of the unburned fuel inside the incoming jet with the oxygen of the lean coflow mixture. Part of the high ϕ_{OH} is due to the transported and diffused OH radicals from the nearfield region to this region. These results suggest that, the premixed and non-premixed flames in TJI-assisted combustion are somewhat difficult to captured by the OH radical.

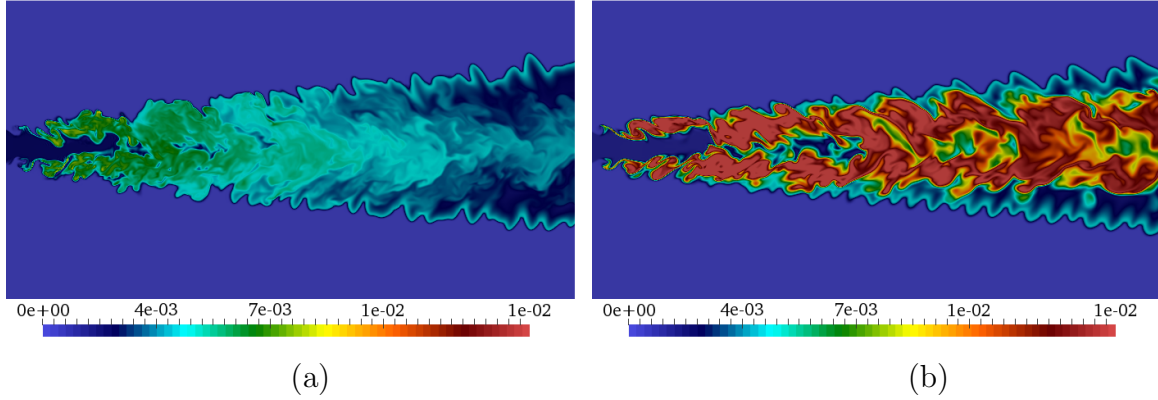


Figure 1.40: Instantaneous contours of the OH mass fraction, ϕ_{OH} , at a middle spanwise plane, $z = 1.5D$, and $t = 17\tau_0$ for (a) Case5 and (b) Case6.

Figures 1.41(a) and 1.41(b) present the H mass fraction contours for Case5 and Case6. The ϕ_H levels in the incoming jets are very low, $1.3e-6$ and $3.3e-4$ (table1.2). Therefore, the main H radicals in the domain are produced by the lean combustion. In the nearfield region, significant H radical is generated by the very complicated, thick, distributed combustion in both cases, even though in the case with extra fuel it is generated much more. In the developed region, the H radical distribution provides useful information concerning flame. In Case5, similar to Case1 to Case4, the maximum value of ϕ_H is located at the premixed lean flame while ϕ_H values are relatively very low in other combustion zones. In Case6, H radical concentration is significant not only at the premixed flame zones, but also inside the hot product zones containing strong diffusion flames. Figure 1.41(b) shows that H

generation is much more significant in the inner jet. This behavior is well correlated with the heat release contours.

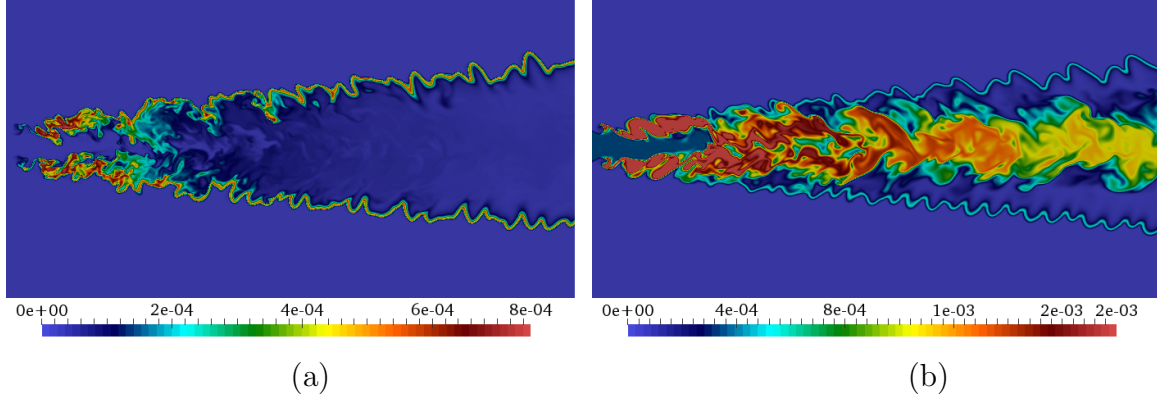


Figure 1.41: Instantaneous contours of the H mass fraction, ϕ_H , at a middle spanwise plane, $z = 1.5D$, and $t = 17\tau_0$ for (a) Case5 and (b) Case6. (Note that the scale limits are set to the available values in each contour and are not the same.)

Figure 1.42(a) and 1.42(b) present the instantaneous contours of heat release rate for Case5 and Case6 at $t = 17\tau_0$. The flame-turbulence structures in the nearfield and developed regions of Case5 are very similar to those shown before for Case3. However, due to lower incoming jet temperature the amount of heat release in the nearfield region is slightly lower, which indicates less heat transfer and the initiation of combustion at lower temperatures. It was observed in figures 1.25(c) and 1.25(e) that the overall combustion zone temperatures in Case5 is lower than that in Case3 due to less heat transfer from the incoming jet to its surroundings. Since the combustion in the developed region is mainly controlled by the coflow, almost the same amount of heat release is generated. This also can be seen in figure 1.42(c), where the mean and the confidence bounds of $y - z$ plane averaged of \dot{Q}_e in the combustion zones are plotted versus streamwise direction.

Despite overall similarities of the thermal half width jet growth in Case6 with that in Case5 and Case3, the flame type and combustion behavior in this case are quite different

than others. For this case the flame-turbulence interactions in the nearfield region are more complex due to the existence of unburned hot fuel in the incoming jet and very significant diffusion flame in the jet zone. The wide and high level of \dot{Q}_e in the nearfield region represents the extensive overlap of thick and distributed premixed flame with the diffusion flame. Marching in the streamwise direction, similar to Case5 and Case3, a spatially continuous and distorted premixed flame is developed which gradually propagates and gets separated from the jet. This is represented by moderate level of \dot{Q}_e at the edge of the flow. However, the high level of \dot{Q}_e values in the inner jet are mostly due to diffusion flames. Figure 1.42(c) shows that the planar averaged heat release values in Case6 are considerably higher than those in other cases even though the coflow conditions are the same. This supports the existence of diffusion combustion of the additional fuel inside the incoming jet. Note that despite the diffusion combustion, some of the extra fuel in the incoming jet could survive and unburned fuel still exists in the combustion zones, which is due to lack of oxygen or long mixing time. The amount of leftover fuel can be controlled by the initial mixture and coflow equivalence ratios, $\phi_{i,j}$ and ϕ_{co} , and the turbulence in the jet and even coflow. Lower (but still greater than one) values of $\phi_{i,j}$ results in lower unburned fuel in the incoming jet and lower ϕ_{co} leads to higher leftover oxidizer after the premixed combustion.

In figures 1.43(a) and 1.43(b) the scatter plot of \dot{Q}_e versus \mathcal{R} are plotted for Case5 and Case6 at different flow sections. Similar to Case3, the maximum heat release occurs at $\mathcal{R} \approx 0.065$ which corresponds to the premixed flame front. The observations and explanations made before for Case3 are also valid for the premixed combustion in Case5 and Case6. However, interestingly, the non-premixed flames in Case6 can also be identified via \mathcal{R} simultaneously with the premixed flames. The non-premixed flame zone of the simulated TJI-assisted combustion system, in which the temperature is relatively high but the equiv-

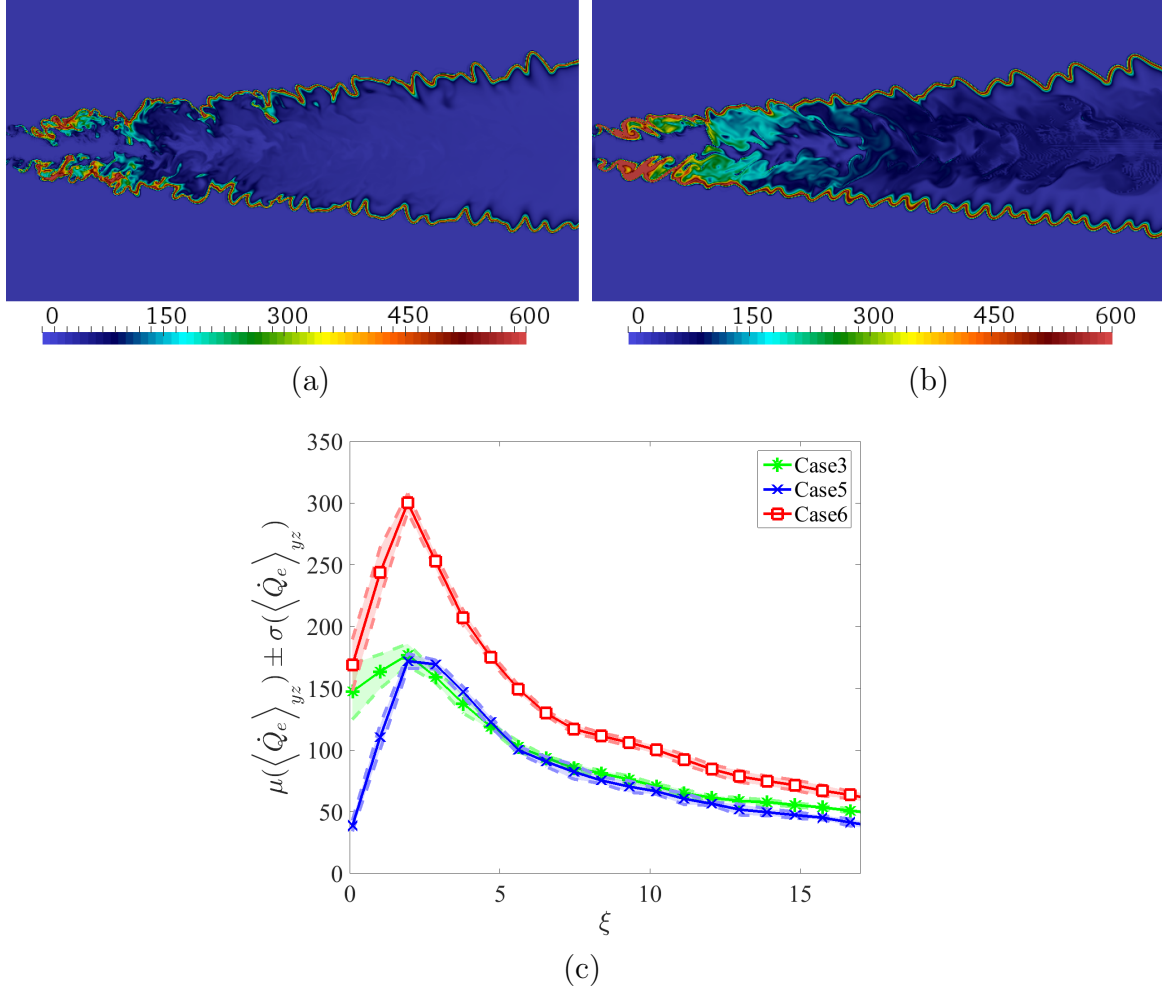


Figure 1.42: Instantaneous contours of the heat release rate, \dot{Q}_e (W), at a middle spanwise plane, $z = 1.5D$, and $t = 17\tau_0$ for (a) Case5 and (b) Case6. (c) Mean and confidence intervals of y - z plane averaged heat release rate, $\mu(\langle \dot{Q}_e \rangle_{yz}) \pm \sigma(\langle \dot{Q}_e \rangle_{yz})$, at $t = 17\tau_0$ versus streamwise direction, ξ , for three cases represented by (*) Case3, (×) Case5, and (▷) Case6.

alence ratio is greater than zero, subsequently leads to larger \mathcal{R} values in Case6 compared to Case3. As it can be seen in figure 1.43(b), the \mathcal{R} values constantly decrease along the streamwise direction, indicating stronger non-premixed combustion in the nearfield region. This was also shown in figure 1.29(i) where the scatter plot of temperature, T , in the combustion zones is plotted versus \mathcal{R} for Case6. Larger \mathcal{R} values at high temperature zones represent the non-premixed combustion.

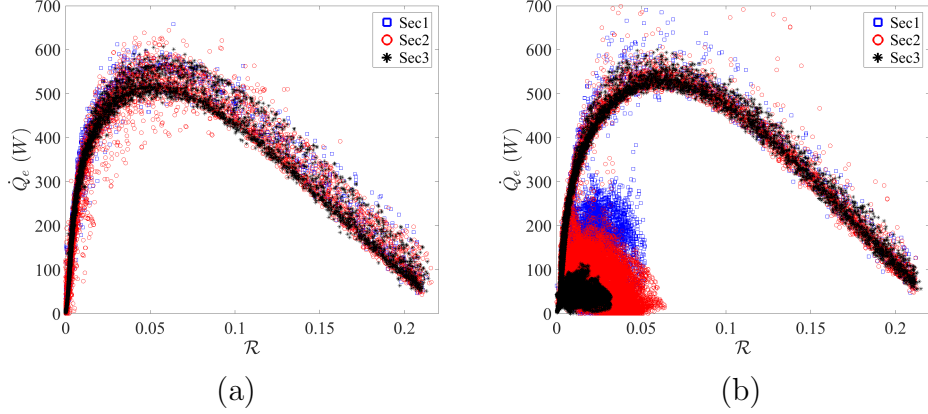


Figure 1.43: Scatter plot of the heat release rate, \dot{Q}_e (W), versus TJI combustion progress variable, \mathcal{R} , for (a) Case5 and (b) Case6 at different streamwise sections represented by (\square) Sec1, (\circ) Sec2, and ($*$) Sec3.

1.7 Chapter conclusions

The thermo-physical processes involved in turbulent jet ignition-assisted combustion systems are explored and studied by direct numerical simulations of a hot product turbulent planar jet injected into a very lean premixed hydrogen-air coflow. The “stationary” jet flow is simulated utilizing high order finite difference methods and detailed chemical kinetics. The simulated TJI-assisted reacting flow can be divided spatially in two *i*) near-field and *ii*) developed regions. In the near-field region, which involves very complex flame/turbulence evolution, the strong interactions and mixing of the premixed coflow with the hot incoming jet lead to a significant autoignition. Stable thick flames are being established in this region, which eventually sustain the ultra-lean combustion downstream. In the developed region, three distinguishable combustion zones are identified: *i*) hot product jet, *ii*) burned-mixed, and *iii*) flame zones. The flame and turbulence structures of these zones have been examined by analyzing various scalar and hydrodynamics quantities. Despite the similarities of simulated flow with “standard” turbulent premixed combustion, the TJI-TPJ flame exhibits significant differences such as higher temperatures and turbulent burning velocities. These differences,

which are due to the interactions of the flame zone with the hot and highly turbulent inner jet, make the TJI-assisted combustion process unique, challenging in combustion safety studies, and rather difficult to model. Even though stable combustion zones are established, the zonal boundaries extensively overlap and oscillate in time throughout the entire flow field. Nevertheless, the flame speed is shown to be well correlated with turbulence intensity in the flame zone. The H radical, the dissipation rate of H radical, the rms of temperature, and the Baroclinic torque are found to consistently identify the flame similar to the heat release rate. Comparison of velocity and temperature statistics indicates that while these two fields are similar in non-reacting flows, the temperature fluctuations are more significant than the velocity fluctuations in reacting flow. These behaviors, particularly in the developed region, show the separation of turbulence in the main jet from the highly wrinkled lean premixed flame. They also confirm that these fields are not very well correlated especially at the flame zone, which is an important factor in developing closure models for these flames.

Direct numerical simulations of various hot product-fuel turbulent planar jets injected into different lean premixed hydrogen-air mixtures (coflows) are performed using detailed chemical kinetics. The thermal jet width is shown to be affected more by the coflow thermochemical conditions and less by the incoming jet composition and properties. However, the combustion zones are highly affected by the jet properties such as temperature and unburned fuel. The unburned hot fuel available in the jet reacting with the remainder oxidizer of the lean premixed combustion creates a complex simultaneous premixed and non-premixed combustion which is hard to model. To identify the flame type and structure, a TJI combustion progress variable is defined which includes the effects of temperature and mixture composition. Further investigations of the combustion regions and zones are performed considering the reaction heat release, temperature, and species concentrations. The low

flammability limit is shown to be lowered by exposing the premixed fuel-air mixture to a hot turbulent jet despite the existence of localized flame extinctions. The interactions between the premixed flame zone and the hot and highly turbulent inner jet are more intense in the ultra-lean coflow mixtures, which may cause localized flame extinction and re-ignition. In the lean mixtures, the premixed flame gets separated from the inner turbulent jet as the flame propagates into the coflow. This affects the inner jet development in the streamwise direction and also the turbulence effects on the flame sheet. Turbulence intensity and vorticity values are shown to be much smaller in the premixed flame propagating faster into the coflow while they always maximize at the edge of the jet located, on average, at the shear layers of the inner jet. It is also found that the temperature and hydrodynamic fields are not well correlated, which is an important factor in modeling of TJI-assisted combustion systems.

Chapter 2

LES/FMDF of Turbulent Jet Ignition assisted Rapid Compression Machines

2.1 Chapter summary

Numerical simulations of turbulent jet ignition (TJI) and combustion in a rapid compression machine (RCM) are conducted by a hybrid Eulerian-Lagrangian large eddy simulation/filtered mass density function (LES/FMDF) computational model. An immersed boundary method is developed and used in the LES to facilitate morphing the complex geometries, to decrease the Monte Carlo (MC) particle search and locate operations in FMDF, and to properly handle finite difference grids and MC particles at the boundaries, while maintaining the high accuracy of the model. TJI is a novel method for initiating combustion in ultra lean mixtures. In TJI-assisted combustion systems, a hot product turbulent jet rapidly propagates from a pre-chamber (PCh) to a main chamber (MCh). Here, for the first time we delineated three main combustion phases in TJI-assisted combustion in a RCM as i) cold fuel jet, ii) turbulent hot product jet, and iii) reverse fuel-air/product jet. The effects of various parameters on these phases are studied numerically, including the igniter timing and location, lean/rich/ N_2 -diluted mixtures, and adiabatic and non-adiabatic walls. It is found that the turbulent jet characteristics and the MCh combustion are highly affected by PCh turbulence intensity as well as the ignition process. Igniting the PCh at the

lower locations close to the nozzle, enforces the PCh charge to fully participate in the PCh ignition/combustion processes and prevents the unburned fuels leaving to the MCh. This also leads to lower velocity hot product jets propagating into the MCh for a longer time, enhancing the MCh combustion. The pressure traces predicted by LES/FMDF are found to be quite well comparable with the available experimental data. Also, the qualitative comparisons of temperature contours with experimental pictures confirm the accuracy and the wealth value of this study.

2.2 Introduction

Turbulent jet ignition (TJI) is an ignition enhancement process which enables the combustion of ultra lean and low temperature mixtures. TJI-assisted combustion systems, typically, consist of a relatively small pre-chamber (PCh), a main chamber (MCh), and a nozzle connecting them. A spark plug and also injectors are installed in the PCh to ignite its charge and provide desired amounts of auxiliary fuel and air. An inflammation zone is, usually, created inside the PCh with a low ignition energy demand which potentially minimizes the requirements of the conventional ignition systems and efficiently initiates and controls the MCh combustion [34]. The combustion processes of different TJI-assisted combustion systems involving PCh-MCh configurations have been reviewed in references [105, 107, 95]. More recently, TJI has been used in rapid compression machines (RCM) [104, 65, 36, 68, 9, 8]. These machines are typically used for interrogating the effects of low-to-intermediate temperature autoignition by compressing fuel-air mixtures, uniformly, to engine-like conditions. In TJI-assisted RCM combustion systems (figure 2.4a), a PCh is installed at the end side of the RCM, referred to as the MCh. The PCh is connected to the MCh through a nozzle

(or several nozzles), allowing the hot product jet(s) to rapidly entering/propagating in the MCh [26]. Ideally, the incoming jet should cause nearly volumetrically and homogeneous combustion, enabling the implementation of lean burned technology in internal combustion (IC) engines. Since the heat release occurs almost simultaneously and rapidly in all the combustion sites, the overall reaction activities are expected to be comparable to those in spark ignition (SI) engines. This allows the TJI-RCM systems to operate at optimum ignition timing, which extends the knock limits. Lean burned TJI-assisted combustion systems, significantly, reduce the pumping loss, improve engine drive cycle efficiency, and decrease carbon emissions since they operate less throttled. The lean homogeneous combustion has also lower temperature and nitrogen oxides emissions.

The performance of TJI-assisted RCM is dependent on the complicated and often coupled effects of various factors such as the initial thermo-chemical conditions, the PCh and MCh geometries, the ignition process (timing, location, amount, and duration of igniter discharged energy), the fuel-air-products mixing, and the fuel chemistry. It is not trivial to experimentally predict the TJI-RCM behavior for various operating conditions. High-fidelity computational models such as those developed based on the large eddy simulation (LES) concept [89, 90, 82, 85, 79, 25, 72] can greatly help with the development and assessment of these systems. However, LES models have not been fully used for this purpose due to the challenges in modeling of sub-grid scales (SGS) correlations. These are more difficult to model, especially, in compressible turbulent reacting flows because of the additional nonlinearity of chemical reactions and the intricate complexities of turbulence/reaction interactions [115]. Additionally, in TJI-assisted combustion systems a broad range of flame types including flamelet type, distributed, premixed, non-premixed, and diffusion flames can exist, simultaneously, in combustion zones [109]. Therefore, the combustion closure models which

are developed based on the assumption of existing one flame type might not be used to predict the overall behavior of such combustion systems, since they may not be able to capture the details of the flame structures accurately. Several reviews and books are available on the advantages and challenges of LES models [89, 90, 82, 85, 79, 25, 72]. The models developed based on the solution of the SGS probability density function (PDF), known as the filtered density function (FDF) [116, 40, 58, 45, 42, 29, 41, 18, 31], are among the most promising models developed for LES of turbulent reacting flows. In the FDF approach, the joint statistics of turbulent variables at the sub-grid level are obtained from the FDF transport equation. The main advantage of the FDF approach is that all terms involving single-point statistics like reaction terms in the FDF equation appear in a closed form. However, the single-point FDF equation is not closed and further modeling for multi-point correlations is needed.

Jaberi et al. [41] developed a FDF model for LES of compressible turbulent reacting flows based on the scalar filtered mass density function (FMDF). This model is basically the mass weighted filtered value of the fine-grained density of energy and species mass fractions. The FMDF model was extended to the velocity-scalar [99, 70] and velocity-scalar-frequency FMDF [100]. The scalar FMDF has been used to simulate a variety of combustion systems [98, 118] without including the effect of pressure on the FMDF, which might be a reasonable assumption for low Mach number and constant pressure combustion. This effect is also included in the FMDF model to accurately simulate high-speed flows [11].

In previous studies [11, 10, 3], successful simulations have been performed by using LES/FMDF along with H-H O-H grid [56] for cylindrical geometries. Despite applicability to flows in complex geometries, the search and locate Monte Carlo (MC) particles in FMDF will be much faster and more accurate for simpler grids. To address this issue and

also incorporate a uniform Cartesian mesh in any geometry, we developed a version of immersed boundary (IB) method [67] compatible with the underlying solver to treat the finite difference (FD) grids and MC particles at the boundaries. The IB method was first introduced by Peskin [76] to compute the blood flow in the cardiovascular systems. There have been numerous efforts [24, 117, 106] to assess its accuracy and stability in a wide range of applications such as compressible [27, 62] and turbulent flows [48, 73]. The LES/FMDF model along with IB methods, in addition of simplifying the grid generation process, requires less calculations in the procedures of searching and locating the MC particles. Also, it allows the maximum use of available computational capacity, since the computational loads are equally divided between all parallel processor. Overall, incorporating IB method in the LES/FMDF model, considerably, decreases the computational cost of simulating turbulent reacting flows in complex geometries, while maintaining the accuracy.

In this study, we use the developed computational model in order to investigate in details the TJI-assisted RCM combustion processes and the effects of various parameters on them. In section 2.3, the governing equations, the compressible single phase FMDF formulation, the numerical approach, and the IB method are described. In section 2.4, the simulated TJI-RCM is described. In section 2.5, the results for both compression and combustion stages are presented and compared with the available experimental data. In section 2.5.2.1, a parametric study is performed, covering the igniter timing and locations, various lean/rich/ N_2 -diluted mixtures, and adiabatic/heat transfer model walls. Section 2.6 summarizes the main findings and conclusions.

2.3 Governing equations

The hybrid compressible LES/FMDF methodology involves two sets of Eulerian and Lagrangian equations, which are solved conjointly for velocity and scalar (species mass fractions and enthalpy) fields. The conservation form of the fully compressible LES equations and the FMDF equation are presented in the following sections.

2.3.1 Filtered compressible Navier-Stokes equations

The standard Favre filtered [6] compressible continuity, momentum, energy, and scalar equations in curvilinear coordinate systems can be combined into the following vector compact form,

$$\frac{\partial (JU)}{\partial \tau} + \frac{\partial (\hat{F} - \hat{F}_v)}{\partial \xi} + \frac{\partial (\hat{G} - \hat{G}_v)}{\partial \eta} + \frac{\partial (\hat{H} - \hat{H}_v)}{\partial \zeta} = J\hat{S}, \quad (2.1)$$

where $U = (\bar{\rho}, \bar{\rho}\tilde{u}, \bar{\rho}\tilde{v}, \bar{\rho}\tilde{w}, \bar{\rho}\tilde{E}, \bar{\rho}\tilde{\phi})$ and $J = \frac{\partial(x,y,z,t)}{\partial(\xi,\eta,\zeta,\tau)}$ are the solution vector and the Jacobian transformation, respectively. The primary variables are the filtered density, $\bar{\rho}$, the Favre filtered velocity components, $\tilde{u}, \tilde{v}, \tilde{w}$, the Favre filtered total energy $\tilde{E} = \tilde{e} + \frac{1}{2}\tilde{u}_i\tilde{u}_i$, and the Favre filtered scalar mass fraction, $\tilde{\phi}$. The coordinate transformation between the physical domain, (x, y, z) , and computational domain, (ξ, η, ζ) , is defined by

$$x = x(\xi, \eta, \zeta), \quad y = y(\xi, \eta, \zeta), \quad z = z(\xi, \eta, \zeta). \quad (2.2)$$

The spatial filtering operation is defined as

$$\bar{f}(x, t) = \langle f(x, t) \rangle_\ell = \int_{-\infty}^{+\infty} f(x', t) h(x', x) dx', \quad (2.3)$$

where $\bar{f}(x, t)$ (or $\langle f(x, t) \rangle_\ell$) represents the filtered value of the transport variable, $f(x, t)$, for the filter function h . However, in compressible flows it is more convenient to consider the Favre filtered variables, where $\tilde{f}(x, t) = \langle f(x, t) \rangle_L = \langle \rho f \rangle_\ell / \langle \rho \rangle_\ell$. In equation 2.1, the inviscid flux vectors are defined as

$$\hat{F} = \begin{bmatrix} \bar{\rho}\hat{U} \\ \bar{\rho}\tilde{u}\hat{U} + \bar{p}\hat{\xi}_x \\ \bar{\rho}\tilde{v}\hat{U} + \bar{p}\hat{\xi}_y \\ \bar{\rho}\tilde{w}\hat{U} + \bar{p}\hat{\xi}_z \\ (\bar{\rho}\tilde{E} + \bar{p})\hat{U} - \hat{\xi}_t \end{bmatrix}, \quad \hat{G} = \begin{bmatrix} \bar{\rho}\hat{V} \\ \bar{\rho}\tilde{u}\hat{V} + \bar{p}\hat{\eta}_x \\ \bar{\rho}\tilde{v}\hat{V} + \bar{p}\hat{\eta}_y \\ \bar{\rho}\tilde{w}\hat{V} + \bar{p}\hat{\eta}_z \\ (\bar{\rho}\tilde{E} + \bar{p})\hat{V} - \hat{\eta}_t \end{bmatrix}, \quad \hat{H} = \begin{bmatrix} \bar{\rho}\hat{W} \\ \bar{\rho}\tilde{u}\hat{W} + \bar{p}\hat{\zeta}_x \\ \bar{\rho}\tilde{v}\hat{W} + \bar{p}\hat{\zeta}_y \\ \bar{\rho}\tilde{w}\hat{W} + \bar{p}\hat{\zeta}_z \\ (\bar{\rho}\tilde{E} + \bar{p})\hat{W} - \hat{\zeta}_t \end{bmatrix} \quad (2.4)$$

where

$$\begin{cases} \hat{F} = \hat{\xi}_x \vec{F} + \hat{\xi}_y \vec{G} + \hat{\xi}_z \vec{H} \\ \hat{G} = \hat{\eta}_x \vec{F} + \hat{\eta}_y \vec{G} + \hat{\eta}_z \vec{H} \\ \hat{H} = \hat{\zeta}_x \vec{F} + \hat{\zeta}_y \vec{G} + \hat{\zeta}_z \vec{H} \end{cases} \quad \text{and} \quad \begin{cases} \hat{U} = \hat{\xi}_t + \hat{\xi}_x \tilde{u} + \hat{\xi}_y \tilde{v} + \hat{\xi}_z \tilde{w} \\ \hat{V} = \hat{\eta}_t + \hat{\eta}_x \tilde{u} + \hat{\eta}_y \tilde{v} + \hat{\eta}_z \tilde{w} \\ \hat{W} = \hat{\zeta}_t + \hat{\zeta}_x \tilde{u} + \hat{\zeta}_y \tilde{v} + \hat{\zeta}_z \tilde{w} \end{cases} \quad (2.5)$$

The viscous fluxes F_v, G_v , and H_v in curvilinear coordinate systems can be written as

$$\begin{aligned}
\hat{F}_v &= \begin{bmatrix} 0 \\ \mu_e \left\{ 2L_1 [\tilde{u}] - \frac{2}{3} (L_1 [\tilde{u}] + L_2 [\tilde{v}] + L_3 [\tilde{w}]) \right\} \\ \mu_e (L_1 [\tilde{v}] + L_2 [\tilde{u}]) \\ \mu_e (L_1 [\tilde{w}] + L_3 [\tilde{u}]) \\ \tilde{u}F_{\nu 2} + \tilde{v}F_{\nu 3} + \tilde{w}F_{\nu 4} + \lambda L_1 [\tilde{T}] + \frac{\bar{\rho}\nu_t}{Pr_t} L_1 [\tilde{H}] \end{bmatrix}, \\
\hat{G}_v &= \begin{bmatrix} 0 \\ \mu_e (L_1 [\tilde{v}] + L_2 [\tilde{u}]) \\ \mu_e \left\{ 2L_2 [\tilde{v}] - \frac{2}{3} (L_1 [\tilde{u}] + L_2 [\tilde{v}] + L_3 [\tilde{w}]) \right\} \\ \mu_e (L_2 [\tilde{w}] + L_3 [\tilde{v}]) \\ \tilde{u}G_{\nu 2} + \tilde{v}G_{\nu 3} + \tilde{w}G_{\nu 4} + \lambda L_2 [\tilde{T}] + \frac{\bar{\rho}\nu_t}{Pr_t} L_2 [\tilde{H}] \end{bmatrix}, \\
\hat{H}_v &= \begin{bmatrix} 0 \\ \mu_e (L_1 [\tilde{w}] + L_3 [\tilde{u}]) \\ \mu_e (L_2 [\tilde{w}] + L_3 [\tilde{v}]) \\ \mu_e \left\{ 2L_3 [\tilde{w}] - \frac{2}{3} (L_1 [\tilde{u}] + L_2 [\tilde{v}] + L_3 [\tilde{w}]) \right\} \\ \tilde{u}H_{\nu 2} + \tilde{v}H_{\nu 3} + \tilde{w}H_{\nu 4} + \lambda L_3 [\tilde{T}] + \frac{\bar{\rho}\nu_t}{Pr_t} L_3 [\tilde{H}] \end{bmatrix}.
\end{aligned} \tag{2.6}$$

in which the operators are

$$\begin{cases} L_1 = \left[\xi_x \frac{\partial}{\partial \xi} + \eta_x \frac{\partial}{\partial \eta} + \zeta_x \frac{\partial}{\partial \zeta} \right] \\ L_2 = \left[\xi_y \frac{\partial}{\partial \xi} + \eta_y \frac{\partial}{\partial \eta} + \zeta_y \frac{\partial}{\partial \zeta} \right] \\ L_3 = \left[\xi_z \frac{\partial}{\partial \xi} + \eta_z \frac{\partial}{\partial \eta} + \zeta_z \frac{\partial}{\partial \zeta} \right] \end{cases} \quad . \tag{2.7}$$

Here, the metric coefficients $\hat{\xi}_t, \hat{\xi}_x, \dots, \hat{\xi}_z$ are defined as $\hat{\xi}_t = J\partial\xi/\partial t$, $\hat{\xi}_x = J\partial\xi/\partial x, \dots, \hat{\xi}_z = J\partial\xi/\partial z$. In the proceeding equations, λ , ν_t , and Pr_t are the thermal conductivity, SGS viscosity, and SGS turbulent Prandtl number. The quantities $F_{\nu n}$, $G_{\nu n}$, and $H_{\nu n}$ are the n^{th} components of F_v , G_v , and H_v vectors.

For the temperature, the Favre filtered internal energy equation is solved, while the SGS part of the kinetic energy is neglected. Furthermore, the subgrid stress terms in equation 2.1 are modeled by a gradient diffusion type closure, in which the effective viscosity, μ_e , is a function of molecular viscosity, μ , and the turbulent kinematic viscosity, ν_t (i.e. $\mu_e = \mu + \bar{\rho}\nu_t$). Turbulent kinematic viscosity is modeled by either the Smagorinsky closure model (primarily used in this study),

$$\nu_t = (C_s \Delta_G)^2 |\tilde{S}|, \quad (2.8)$$

or the modified kinematic energy velocity (MKEV) model,

$$\nu_t = C_m \Delta_G \sqrt{|\tilde{u}_i^* \tilde{u}_i^* - \langle \tilde{u}_i^* \rangle_{l'} \langle \tilde{u}_i^* \rangle_{l'}|}. \quad (2.9)$$

In the Smagorinsky model, C_s is the model constant and $|\tilde{S}|$ is the magnitude of filtered strain rate tensor calculated by

$$|\tilde{S}| = \sqrt{2\tilde{S}_{ij}\tilde{S}_{ij}}. \quad (2.10)$$

Similarly, in the MKEV model C_m is the model coefficient and $\langle \tilde{u}_i^* \rangle$ is defined as $\langle \tilde{u}_i^* \rangle = \tilde{u}_i - u_{ref}$ (u_{ref} is added to ensure the Galilean invariance and l' denotes the secondary filter function). In both models, Δ_G is the characteristic size of the filter function. In non-reacting simulations, the source term \hat{S} in equation 2.1 is a null vector, whereas in reacting simulations it is obtained from the FMDF. Favre filtered heat flux is defined as $\tilde{H} = \tilde{E} + \frac{\tilde{p}}{\bar{\rho}}$

and the subgrid heat flux closure, H_{ij}^{SGS} , is calculated based on a gradient diffusion model

$$H_i^{SGS} = \frac{-\bar{\rho}\nu_t}{Pr_t} \frac{\partial \tilde{H}}{\partial x_i}. \quad (2.11)$$

2.3.2 Compressible single phase scalar FMDF equations

The scalar FMDF is the joint PDF of the scalar vector at sub-grid level and is defined as

$$P_L(\Psi; x, t) = \int_{-\infty}^{+\infty} \rho(x', t) \sigma[(\Psi, \Phi(x', t))] \mathbf{G}(x' - x) dx', \quad (2.12)$$

where \mathbf{G} represents the filter function, Ψ is the scalar vector in the sample space. σ is the fine-grained density defined based on a series of delta functions, δ , by

$$\sigma[(\Psi, \Phi(x', t))] = \prod_{\alpha=1}^{N_s+1} \delta(\psi_\alpha - \phi_\alpha(x, t)). \quad (2.13)$$

N_s represents the number of the species and the scalar vector, $\Phi \equiv \phi_\alpha$, ($\alpha = 1, \dots, N_s + 1$), includes the species mass fractions and the specific enthalpy ($\phi_{\alpha=N_s+1}$). The transport equation for the FMDF can be derived from the following unfiltered scalar equation in Cartesian coordinate system:

$$\rho \frac{\partial \phi_\alpha}{\partial t} + \rho u_i \frac{\partial \phi_\alpha}{\partial x_i} = \frac{\partial}{\partial x_i} \left(\Gamma \frac{\partial \phi_\alpha}{\partial x_i} \right) + \rho (S_\alpha^R + S_\alpha^{cmp}). \quad (2.14)$$

The source term, $S_\alpha^R = \dot{\omega}_\alpha$, represents the production or consumption of species α ($\alpha = 1, \dots, N_s$) due to reaction. For Energy (or Enthalpy) equation ($\alpha = N_s + 1$), the source term $S_\alpha^R = \dot{Q}$ is the combustion heat and $S_\alpha^{cmp} = \frac{1}{\rho} \left(\frac{\partial p}{\partial t} + u_i \frac{\partial p}{\partial x_i} + \tau_{ij} \frac{\partial u_i}{\partial x_j} \right)$ is compressibility term. The exact

FMDF equation can be derived from the time derivative of FMDF equation 2.12 as

$$\frac{\partial P_L(\Psi; x, t)}{\partial t} = -\frac{\partial}{\partial \psi_\alpha} \left[\left\langle \frac{\partial \phi_\alpha}{\partial t} | \Psi \right\rangle_l P_L(\Psi; x, t) \right], \quad (2.15)$$

where $\langle f | \Psi \rangle_l$ represents the conditional filtered value of function f . The FMDF transport equation can be obtained by inserting equation 2.14 into equation 2.15 as

$$\begin{aligned} \frac{\partial P_L}{\partial t} + \frac{\partial (\langle u_i | \Psi \rangle_l P_L)}{\partial x_i} - \left\langle \left(\frac{1}{\rho} \left[\frac{\partial \rho}{\partial t} + \frac{\partial (\rho u_i)}{\partial x_i} \right] \right) | \psi \right\rangle_l P_L \\ = \frac{\partial}{\partial \psi_\alpha} \left[\left\langle - \left(\frac{1}{\rho} \frac{\partial}{\partial x_i} \Gamma \frac{\partial \phi_\alpha}{\partial x_i} \right) | \Psi \right\rangle_l P_L \right] \end{aligned} \quad (2.16)$$

$$- \frac{\partial}{\partial \psi_\alpha} [\langle S_\alpha^R | \Psi \rangle_l P_L] - \frac{\partial}{\partial \psi_\alpha} [\langle S_\alpha^{cmp} | \Psi \rangle_l P_L].$$

The species and energy source terms in equation 2.16 are defined as

$$\begin{cases} S_\alpha^R = \dot{\omega}_\alpha, & S_\alpha^{cmp} = 0, & \alpha \equiv 1, \dots, N_s \\ S_\alpha^R = \dot{Q}, & S_\alpha^{cmp} = \frac{1}{\rho} \left(\frac{\partial p}{\partial t} + u_i \frac{\partial p}{\partial x_i} + \tau_{ij} \frac{\partial u_i}{\partial x_j} \right), & \alpha \equiv N_{s+1} \end{cases}. \quad (2.17)$$

The chemical reaction source term, $-\frac{\partial}{\partial \psi_\alpha} [\langle S_\alpha^R | \Psi \rangle_l P_L]$, is closed when the SGS pressure fluctuation effects are ignored. This term in the filtered scalar equation and conventional LES methods is not closed, therefore, the FMDF equation cannot be solved directly due to presence of three unclosed terms: $\frac{\partial (\langle u_i | \Psi \rangle_l P_L)}{\partial x_i}$, $\frac{\partial}{\partial \psi_\alpha} \left[\left\langle - \left(\frac{1}{\rho} \frac{\partial}{\partial x_i} \Gamma \frac{\partial \phi_\alpha}{\partial x_i} \right) | \Psi \right\rangle_l P_L \right]$, and $-\frac{\partial}{\partial \psi_\alpha} [\langle S_\alpha^R | \Psi \rangle_l P_L]$.

The unclosed convection term, $\frac{\partial (\langle u_i | \Psi \rangle_l P_L)}{\partial x_i}$, can be decomposed into two large and SGS

convection terms as

$$\langle u_i | \Psi \rangle_l P_L = \langle u_i \rangle_L P_L + (\langle u_i | \Psi \rangle_l P_L - \langle u_i \rangle_L P_L). \quad (2.18)$$

The SGS convection term is modeled via a gradient type closure as

$$(\langle u_i | \Psi \rangle_l P_L - \langle u_i \rangle_L P_L) = \Gamma_t \frac{\partial (P_L / \langle \rho \rangle_l)}{\partial x_i}, \quad (2.19)$$

where $\Gamma_t = \langle \rho \rangle_l \nu_t / Pr_t$ is the turbulent diffusivity and Pr_t is the turbulent Prandtl number.

The second unclosed term is decomposed in two molecular and SGS dissipation terms as

$$\begin{aligned} & \frac{\partial}{\partial \psi_\alpha} \left[\left\langle - \left(\frac{1}{\rho} \frac{\partial}{\partial x_i} \Gamma \frac{\partial \phi_\alpha}{\partial x_i} \right) | \Psi \right\rangle_l P_L \right] \\ &= \frac{\partial}{\partial x_i} \left[\Gamma \frac{\partial (P_L / \langle \rho \rangle_l)}{\partial x_i} \right] + \frac{\partial}{\partial \psi_\alpha} [\Omega_m (\psi_\alpha - \langle \phi_\alpha \rangle_l) P_L]. \end{aligned} \quad (2.20)$$

The SGS dissipation is modeled via the linear mean square estimation (LMSE) or the interaction by exchange with the mean model (IEM) with the Ω_m to be the SGS mixing frequency, which can be obtained from the molecular and SGS turbulent diffusivity (Γ and Γ_t) and the filter size (Δ_G) as

$$\Omega_m = C_\omega \frac{\Gamma + \Gamma_t}{\Delta_G \langle \rho \rangle_l}. \quad (2.21)$$

The Reynolds-averaged Navier Stokes (RANS) PDF method for compressible flows was extended by Delarue and Pope [19], in which pressure is considered as one of the random variables in the PDF formulation and a set of modeled stochastic equations is solved for the joint velocity-frequency-energy-pressure PDF. In this study, the pressure is not directly

included in the FMDF formulation and only the effect of filtered pressure on the scalar FMDF is considered. The last term in equation 2.16 represents the effects of pressure and viscosity on the scalars, where the temporal derivative of pressure can be written as

$$\left\langle \left(\frac{1}{\rho} \frac{\partial p}{\partial t} \right) | \Psi \right\rangle_l P_L = \frac{1}{\langle \rho \rangle_l} \frac{\partial \langle p \rangle_l}{\partial t} P_L \quad \alpha \equiv N_{s+1}. \quad (2.22)$$

The spatial derivative part is decomposed into the resolved and SGS parts,

$$\begin{aligned} \left\langle \left(\frac{1}{\rho} u_i \frac{\partial p}{\partial x_i} \right) | \Psi \right\rangle_l P_L &= \frac{1}{\langle \rho \rangle_l} \langle u_i \rangle_L \frac{\partial \langle p \rangle_l}{\partial x_i} P_L \\ + \left(\left\langle \left(\frac{1}{\rho} u_i \frac{\partial p}{\partial x_i} \right) | \Psi \right\rangle_l P_L - \frac{1}{\langle \rho \rangle_l} \langle u_i \rangle_L \frac{\partial \langle p \rangle_l}{\partial x_i} P_L \right) &\quad \alpha \equiv N_{s+1}. \end{aligned} \quad (2.23)$$

Similarly, the viscous dissipation part is decomposed into the resolved and SGS parts,

$$\begin{aligned} \left\langle \left(\frac{1}{\rho} \tau_{ij} \frac{\partial u_i}{\partial x_j} \right) | \Psi \right\rangle_l P_L &= \frac{1}{\langle \rho \rangle_l} \langle \tau_{ij} \rangle_L \frac{\partial \langle u_i \rangle_l}{\partial x_j} P_L \\ + \left(\left\langle \left(\frac{1}{\rho} \tau_{ij} \frac{\partial u_i}{\partial x_j} \right) | \Psi \right\rangle_l P_L - \frac{1}{\langle \rho \rangle_l} \langle \tau_{ij} \rangle_L \frac{\partial \langle u_i \rangle_l}{\partial x_j} P_L \right) &\quad \alpha \equiv N_{s+1}. \end{aligned} \quad (2.24)$$

However, the SGS pressure term in equation 2.23 and the SGS viscous term in equation 2.24 are ignored. By inserting equations 2.18-2.24 into equation 2.14, the final form of the FMDF

transport equation for single-phase compressible reacting system can be derived as

$$\begin{aligned}
& \frac{\partial P_L}{\partial t} + \frac{\partial (\langle u_i \rangle_L P_L)}{\partial x_i} \\
&= \frac{\partial}{\partial x_i} \left[(\Gamma + \Gamma_t) \frac{\partial (P_L / \langle \rho \rangle_L)}{\partial x_i} \right] \\
&+ \frac{\partial}{\partial \psi_\alpha} [\Omega_m (\psi_\alpha - \langle \phi_\alpha \rangle_L) P_L] \\
&- \frac{\partial}{\partial \psi_\alpha} [S_\alpha^R (\psi) P_L] - \frac{\partial}{\partial \psi_\alpha} [\tilde{S}_\alpha^{cmp} (\psi) P_L],
\end{aligned} \tag{2.25}$$

where

$$\begin{cases} S_\alpha^R = \dot{\omega}_\alpha, & \tilde{S}_\alpha^{cmp} = 0, & \alpha \equiv 1, \dots, N_s \\ S_\alpha^R = \dot{Q}, & \tilde{S}_\alpha^{cmp} = \frac{1}{\langle \rho \rangle_L} \left(\frac{\partial \langle p \rangle_L}{\partial t} + \langle u_i \rangle_L \frac{\partial \langle p \rangle_L}{\partial x_i} + \langle \tau_{ij} \rangle_L \frac{\partial \langle u_i \rangle_L}{\partial x_j} \right), & \alpha \equiv N_{s+1} \end{cases} \tag{2.26}$$

The scalar field can be obtained from the modeled scalar FMDF transport equation, which is closed and provides all single-point spatial and temporal statistics of species and temperature. However, to check the mathematical consistency between the FMDF and the conventional LES methods, the transport equations for the filtered scalar variables can also be solved directly by FD methods. Here, we only solve the FD equation for one of the reactive species.

2.3.3 Numerical approach

The attributes of the hybrid LES/FMDF model are shown in figure 2.1. In this model, the filtered velocity and pressure are obtained by solving equation 2.1 with the conventional FD methods, while the species mass fractions and temperature are computed using the FMDF-MC approach. In this approach, the modeled FMDF equation is solved by the Lagrangian MC procedure with the known filtered velocity and pressure fields. In this procedure, equation 2.20 is solved indirectly via equivalent stochastic (diffusion) equations. Each MC particle is spatially transported in the physical space due to the large scale convection, and sub-grid and molecular diffusion. This is implemented through a set of SDEs as

$$dX_i^+ = \left[\langle U_i \rangle_L \frac{1}{\langle \rho \rangle_l} \frac{\partial (\Gamma + \Gamma_t)}{\partial x_i} \right] dt + \left[\sqrt{\frac{2 (\Gamma + \Gamma_t)}{\langle \rho \rangle_l}} \right] dW_i(t), \quad (2.27)$$

where W_i denotes the Wiener process. The change in the composition space occurs due to SGS and molecular mixing, chemical reaction, viscous dissipation, and pressure variation in time and space, which is described by the following SDEs:

$$d\phi_\alpha^+ = -\Omega_m (\phi_\alpha^+ - \langle \phi_\alpha \rangle_L) dt + (S_\alpha^R(\phi^+) + \tilde{S}_\alpha^{cmp}) dt \quad \alpha \equiv 1, \dots, N_{s+1}. \quad (2.28)$$

The combination of all processes described by equations 2.27 and 2.28 yields a Fokker-Planck equation, which is identical to the FMDF transport equation (equation 2.25). This equation governs the PDFs of stochastic processes, in which the large scale, SGS, molecular mixing, and the chemical reactions are incorporated. The number of MC particles are managed via a procedure involving the use of nonuniform weights. The variable weighting allows the particle number to vary between certain minimum and maximum numbers. MC

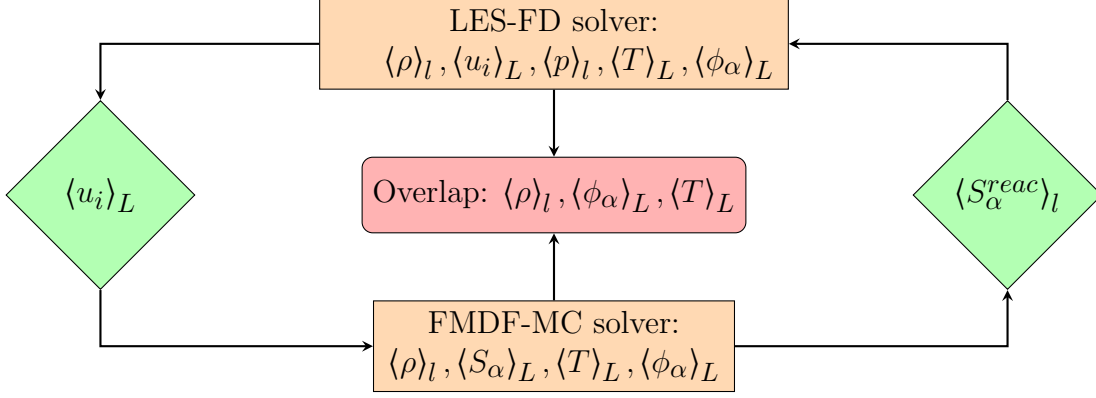


Figure 2.1: The attributes of the hybrid LES/FMDF model.

particles are weight averaged over a box of size Δ_E centered at the point of interest to calculate the Favre filtered values of variables at a given point. It can be shown that the summation of weights within the ensemble averaging domain, Δ_E , is related to the filtered fluid density as

$$\langle \rho \rangle_l \approx \frac{\Delta_m}{V_E} \sum_{n \in \Delta_E} w^{(n)}, \quad (2.29)$$

where V_E is the domain volume, Δ_m is the MC particle mass with a unit weight, and $w^{(n)}$ represents the MC particle weight within the ensemble domain. The Favre-filtered value of any function of scalars, $\langle Q \rangle_L$, is obtained from the following weighted averaging operation,

$$\langle Q \rangle_L \approx \frac{\sum_{n \in \Delta_E} w^{(n)} Q(\phi)}{\sum_{n \in \Delta_E} w^{(n)}}. \quad (2.30)$$

The discretization of filtered gas dynamics equations is based on the compact FD scheme [57], which yields up to sixth (or higher) order spatial accuracy. In order to avoid numerical instabilities and remove the numerical noises generated by the growth of numerical errors at high wave number modes, a low pass, high order, spatial implicit filtering operator is used [57]. The time differencing is based on a third order low storage Runge Kutta method [10].

2.3.4 MC particle tracking and parallelization

The search and locate procedure of MC particles could become computationally intensive in the LES/FMDF method [11, 10, 3]. Here, an effective method has been developed to reduce its cost by using a structured, orthogonal, uniform, and multi-block Eulerian grid system. Figure 2.2 shows the FD mesh (solid yellow lines), MC particles (small purple circles), and imaginary control volumes (dashed green lines) around the grid points. The procedure is three-dimensional but to better describe it, a two dimensional schematic is considered. In figure 2.2, the quadrilateral $qrst$ is formed around the FD grid point O , which is a good representative for this cell. The particles within the $qrst$ are used in ensemble averaging. To perform ensemble averaging and interpolation for MC particles, this quadrilateral has to be determined. For all the particles located inside the $qrst$, the values at the corners are used.

A general form of this procedure for non-orthogonal grid is described here. In order to locate the MC particle, initially, the corresponding computational processor index is identified. Thereafter, the quadrilateral $qrst$ is specified by the 3 indexes of point p . To determine the i^{th} component of point q , the auxiliary vectors \vec{sp} , \vec{sq} , and \vec{A} are defined. \vec{A} is the normal vector to \vec{st} , where its direction could be either way. Therefore, $G(q)$ is defined as

$$G(q) = (\vec{sp} \cdot \vec{A})(\vec{sq} \cdot \vec{A}). \quad (2.31)$$

The sign of the $G(q)$ identifies whether the particle p and point q lie on the same side of \vec{st} or not. Sweeping start point is assumed to be $i = 1$ and is performed in the direction of increasing i . Point q is the first point with positive G value. The particles are tracked in three different grid line directions, separately, and a similar procedure is used in other three grid line directions as shown in figure 2.2. As the i^{th} component of q is determined, the

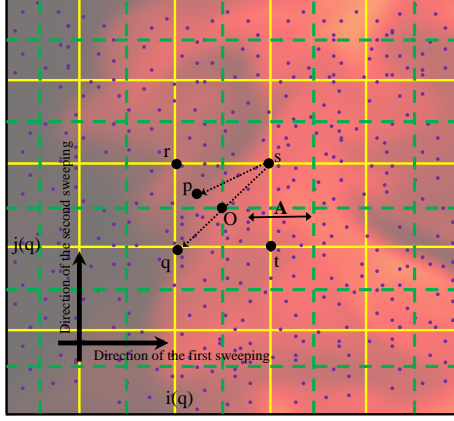


Figure 2.2: Schematic of the grid points, large black circles; MC particles, small purple circles; control volumes, dashed green lines around the grid points; FD mesh, solid yellow line; and sweeping directions to determine i^{th} and j^{th} components of the point q .

k^{th} component could be specified by searching in a grid plane. By knowing the i^{th} and k^{th} components, j^{th} component is determined simply by sweeping in a segment formed by grid lines. To interpolate the properties to the particle location, a linear interpolation is used. Since the uniform grid is used here, no further interpolation is needed from the physical domain to the computational domain. Therefore, the velocity of the particle p is computed by an interpolation of the values at the corner of the quadrilateral $qrst$. This scheme has been successfully implemented in the underlying LES/FMDF solver. Reflecting boundary condition is used for MC particles at the boundaries as described below.

2.3.5 Immersed boundary method for LES/FMDF

A version of immersed boundary (IB) method compatible with the LES/FMDF computational model is developed and used here. For this, the solution algorithm is modified locally by enforcing the desired boundary conditions for both FD grids and MC particles. Therefore, a Cartesian mesh is used and it is not required to morph the computational mesh to the physical boundaries. With the IB method, the LES/FMDF model retains most of the favor-

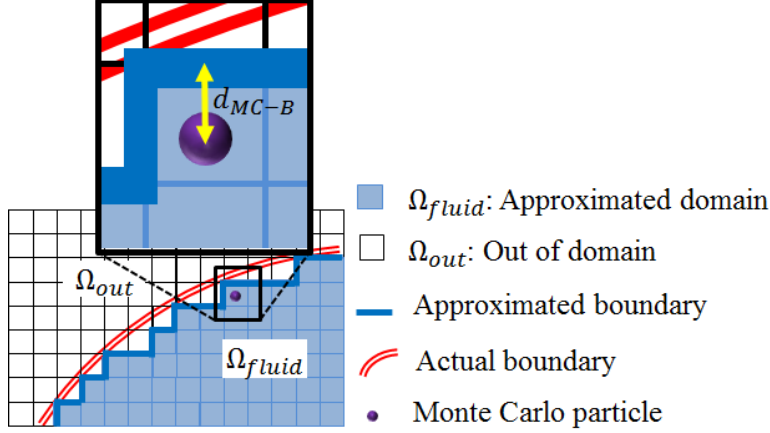


Figure 2.3: Schematic of approximated domain using IB method. Ω_{fluid} , out of domain Ω_{out} , approximated boundary (thick line), actual boundary (parallel lines), and Monte Carlo particles • .

able properties of structured grids and also provides a high level of flexibility in tackling flows and MC particles for two reasons. First, the procedure of search and locate MC particles requires less calculations. Second, the computational load is almost equally divided between the processors, which facilitates the maximum utilization of available parallel computational processors with simple and less expensive communication procedures.

Figure 2.3 shows the actual boundaries, approximated fluid domain (shaded area, Ω_{fluid}), approximated boundary (thick line), and the out of domain area (Ω_{out}). The conservation of mass is satisfied within the Ω_{fluid} and Dirichlet boundary condition is used for velocity components at the approximated boundaries. The parameter d_{MC-B} denotes the distance between a MC particle and the associate boundary. Reflecting conditions with new d_{MC-B} equals to 1×10^{-6} (m) are used to relocate the particles hitting the boundaries.

2.4 TJI-RCM setup and computational domain

The simulated TJI-RCM is similar to the optically accessible TJI-RCM experiment at Michigan State University, operating with a compression ratio of 8.5 [26]. This machine is mainly

composed of three separate pneumatic, hydraulic, and combustion cylinder pistons, which are mechanically coupled. Initially, the RCM cylinder is evacuated before filling it with a fuel and air mixture at a specific equivalence ratio, and preheating to $353K$. The mixture is then rapidly compressed to the desired elevated temperature and pressure. At the end of the compression process, the fuel and air mixture is well and (ideally) homogeneously mixed. This mixture is held at a constant volume, while the PCh igniter is being charged for a duration of about $5ms$. The PCh combustion is initiated by a spark plug. The PCh is a relatively small chamber with about 2% of the MCh volume and separate fuel and air injectors, igniter, and a pressure transducer (figure 2.4a). After a successful ignition, a hot product turbulent jet is generated and injected into the MCh, which starts the MCh combustion. The entire process is described in more details in section 2.5.

The LES/FMDF equations are solved on the orthogonal uniform mesh along with IB method to simulate the the curved surfaces. A Neumann boundary condition is imposed for the density, ($\frac{\partial \rho}{\partial n} = 0$, where n is the direction normal to the immersed surface) and no-slip boundary condition is used for the velocity components at the approximated boundaries. According to the previous studies [63, 10, 11], moderate heat transfer occurs at the combustion chamber wall, which has some effects on the temperature distribution in both PCh and MCh. Here, we primarily use adiabatic walls, however, a conductive heat transfer model is also developed and used.

In order to ensure the grid quality throughout the domain, all simulations are conducted with a uniform grid spacing equals to 2.5×10^{-4} (m) in all directions. In figure 2.4(b) and table 2.1, the specifications of the simulated three-dimensional mesh and computational domain are presented. In generating the computational geometry, the volumes occupied by the igniter and fuel and air injectors inside the PCh are subtracted from the actual volume

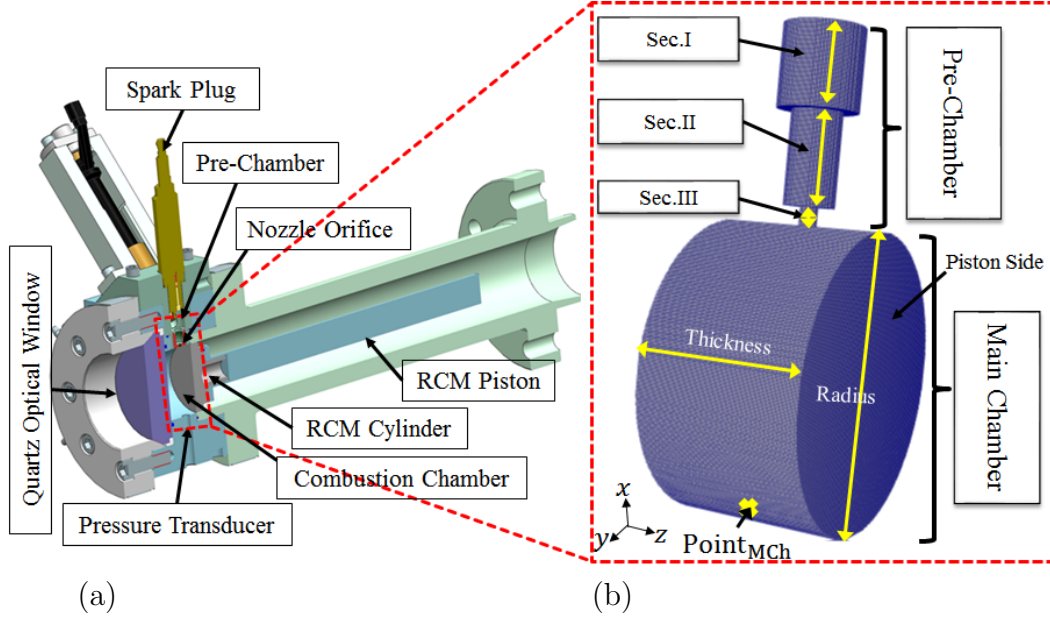


Figure 2.4: (a) TJI-RCM combustion system and (b) 3D view of the TJI-RCM mesh.

to make the computational volume equal to the experimental volume. The computational domain is massively partitioned in two streamwise and cross-stream directions. In order to maintain the accuracy across the parallel processors and grid block boundaries, 5 overlap grids are used using fifth order compact FD scheme [57]. The computational resources are provided by high performance computing center at Michigan State University [1] and University of Texas at Austin [2]. A typical simulation on 100 Intel processors for about $1ms$ of combustion and compression stages requires 3.0×10^3 and 1.5×10^3 service unit (SU), respectively.

Table 2.1: Specifications of TJI-assisted RCM computational domain.

Chamber		Radius (mm)	Height/Width (mm)
PCh	Sec. I	6.75	14.00
	Sec. II	4.25	16.00
	Sec. III	1.50	3.00
MCh		25.35	26.70

2.5 Results and discussions

The flow/combustion in the TJI-assisted RCM can be divided in two main *i*) compression and *ii*) combustion stages, which are described in details in the following subsections.

2.5.1 Compression stage

Here, the compression stage of TJI-RCM is simulated incorporating a static mesh and imposing the available experimental pressure traces, $p = p_{\text{experiment}}$, and Neumann boundary conditions for temperature and filtered velocity components, i.e. $\frac{dT}{dz} = 0$ and $\frac{d\bar{u}_i}{dz} = 0$, on the piston side of the RCM (figure 2.4b). Figure 2.5(a) presents the three-dimensional iso-surfaces of velocity magnitude, $|\vec{U}|$ (m/s), inside the TJI-RCM at the end of the compression stage, where piston stays at the top dead center (TDC). In figure 2.5(b), the contour plots of vorticity magnitude, $|\vec{\omega}|$ ($1/s$), at the middle of the RCM are plotted in xy and zy planes. For a better representation of the flow structures, the velocity contours in half of the domain are plotted. As it can be observed in this figure a highly distorted low velocity turbulent flow is generated during the compression stage. The generated turbulent field inside the PCh facilitates the combustion by enhancing the burning velocity.

The temporal evolution of the PCh flow during the compression stage is shown through contour plots of velocity and vorticity magnitudes in figures 2.6 and 2.7. Initially, the relatively low pressure difference between MCh and PCh, gently, pushes the premixed fuel-air mixture into the initially stagnant PCh (figures 2.6(a)-(c) and 2.7(a)-(c)). However, after about 14 (ms), a well developed unsteady turbulent round jet penetrates into the PCh (figures 2.6d and 2.7d). The piston acceleration, which occurs approximately in the time frame of $17\ (ms) \lesssim t \lesssim 27\ (ms)$, significantly, increases the jet velocity and vorticity

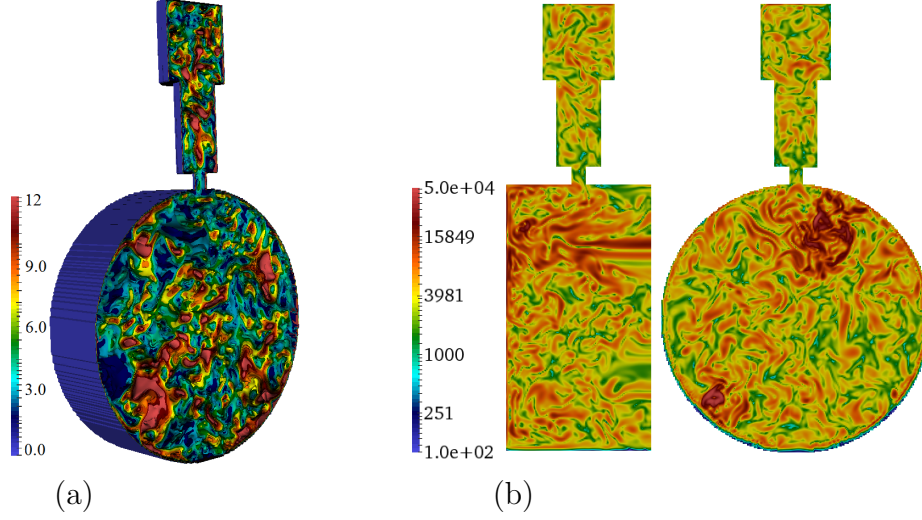


Figure 2.5: TJI-RCM flow structures at the end of the compression stage: (a) Contour plot of iso-surfaces of velocity magnitude, $|\vec{U}|$ (m/s), and (b) Contour plot of vorticity magnitude, $|\vec{\omega}|$ (1/s), in the middle of the domain at xy and xz planes.

magnitudes (figures 2.6e-g and 2.7e-g). While the fuel-air jet penetrates into the PCh and reaches the surrounding wall strong vortices are appeared, initiating an intense turbulent flow inside the PCh. The piston begins decelerating around $27 \text{ (ms)} \lesssim t$ and as it can be observed in figures 2.6(h)-(i) and 2.7(h)-(i), the PCh flow speed decreases and the jet vanishes when the piston reaches the TDC at $t = 30 \text{ (ms)}$. At this point, a somewhat homogeneous turbulent flow dominates the PCh (figures 2.6j and 2.7j), which may cause difficulties in stabilizing the flame in the PCh during ignition. In the experiments, about 5 (ms) after the piston reaches the TDC, the igniter is discharged. This delay helps to stabilize the flame, however, it affects other processes including PCh turbulence intensity, flame speed, and, eventually, the characteristics of the generated hot product jet.

The compression stage is simulated incorporating two adiabatic and non-adiabatic wall conditions. Thus, a heat transfer model is developed based on the energy balance between the flow, inner and outer walls to calculate the inner wall temperature. Figure 2.8 shows a schematic of the model and the related quantities. Here, T_g is the mean temperature of

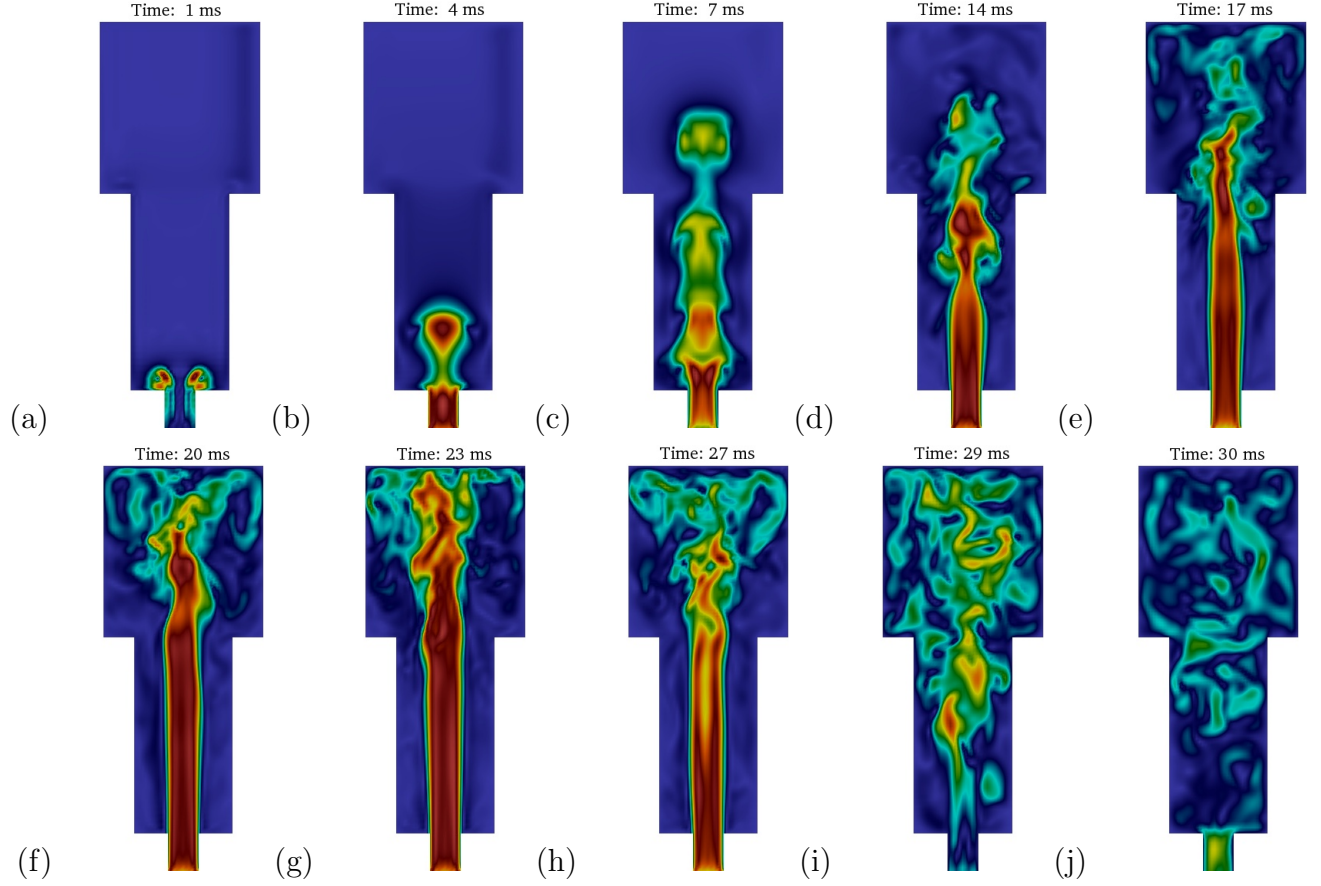


Figure 2.6: Time evolution of the PCh flow field during the compression stage considering contour plots of velocity magnitude, $|\vec{U}|$ (m/s).

the inside flow, T_{w_i} is the temperature of the inner wall, T_{w_o} is the assigned temperature of the outer wall, h_{cg} is the mean convection heat transfer coefficient, k_{cw} is the thermal conductivity for the wall, Δx_w is the wall thickness, and Q is the heat flux. By applying the energy balance, it is obtained that

$$Q = \frac{k_{cw}A(T_{w_i} - T_{w_o})}{\Delta x_w} = h_{cg}A(T_g - T_{w_i}). \quad (2.32)$$

Thus, the temperature of the inner wall is given by

$$T_{w_i} = \frac{h_{cg}T_g + (k_{cw}/\Delta x_w)T_{w_o}}{h_{cg} + (k_{cw}/\Delta x_w)}, \quad (2.33)$$

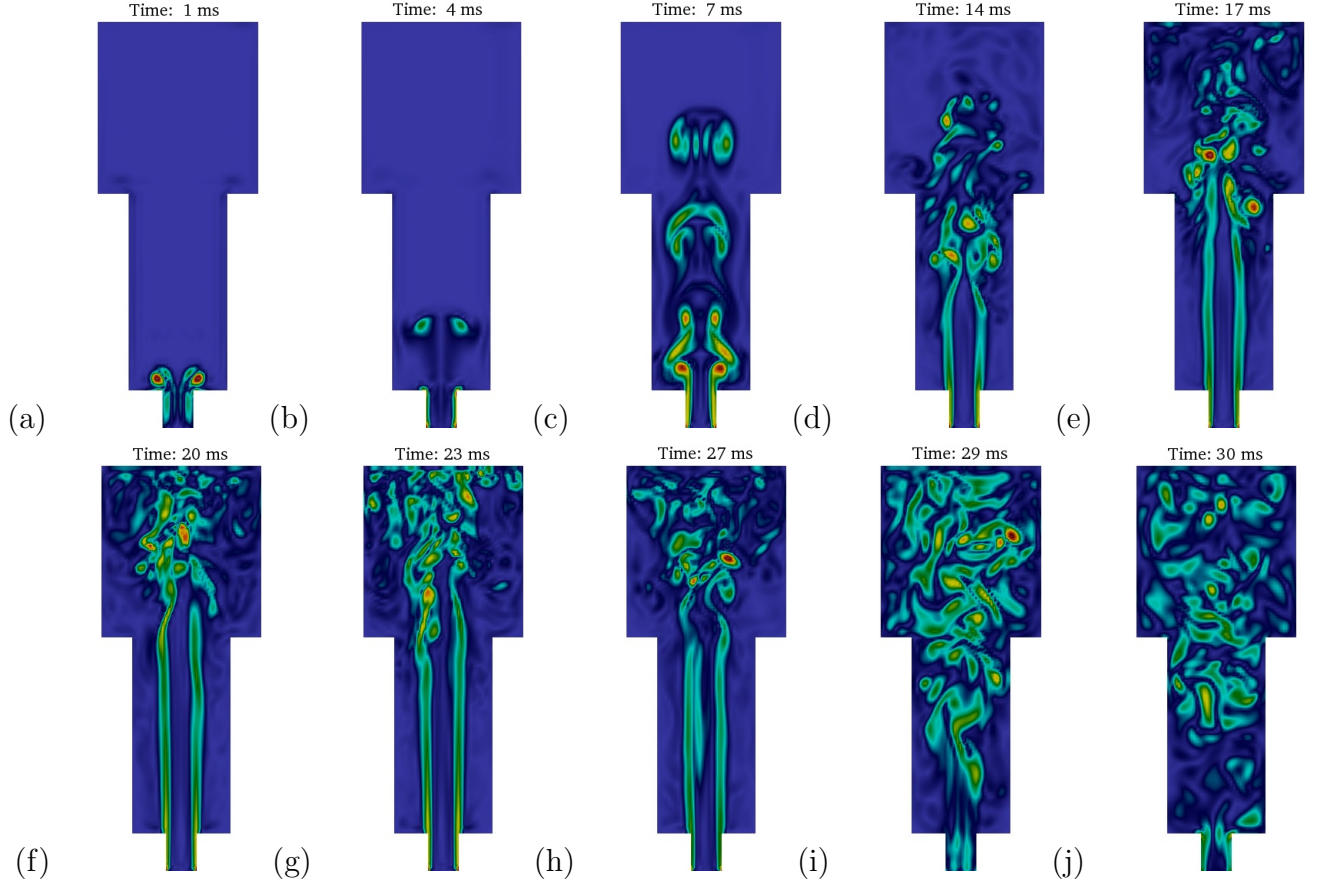


Figure 2.7: Time evolution of the PCh flow field during the compression stage considering contour plots of vorticity magnitude, $|\vec{\omega}|$ (1/s).

where the mean convective heat transfer coefficient is calculated as

$$h_{cg} = \frac{Nu_g k_{cg}}{D}. \quad (2.34)$$

Here, k_{cg} represents the gas thermal conductivity, D is the PCh or MCh diameter based on the location of the wall. Nu_g is the mean Nusselt number calculated as $Nu_g = 0.035Re^{0.8}$, where Re is the mean Reynolds number. The outer wall temperature is set equals to 353K. The heat transfer from the walls to the interior flow gas was not allowed.

Figures 2.9(a) and 2.9(b) show the predicted temperature contours at the end of the compression stage for cases with adiabatic and conductive walls. As it can be seen in these

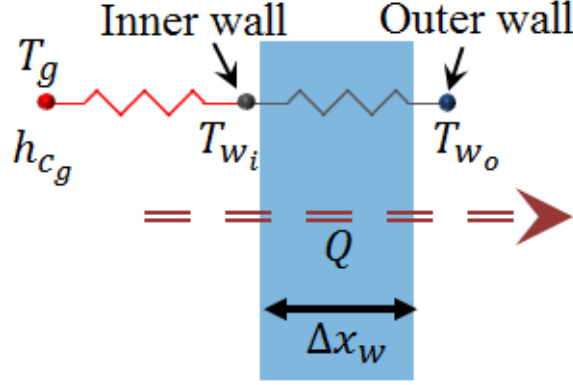


Figure 2.8: Schematic of the wall heat transfer model and related quantities.

two figures, the MCh gas temperature distributions are nearly homogeneous with mean values equal to $754K$ and $742K$. Homogeneous temperature distributions are also observed in the PCh. However, the PCh mean temperature for the case with conductive walls is lower than that for the case with adiabatic walls. This difference is because of the high ratio of the PCh wall-surfaces area to volume, which increases the heat loss.

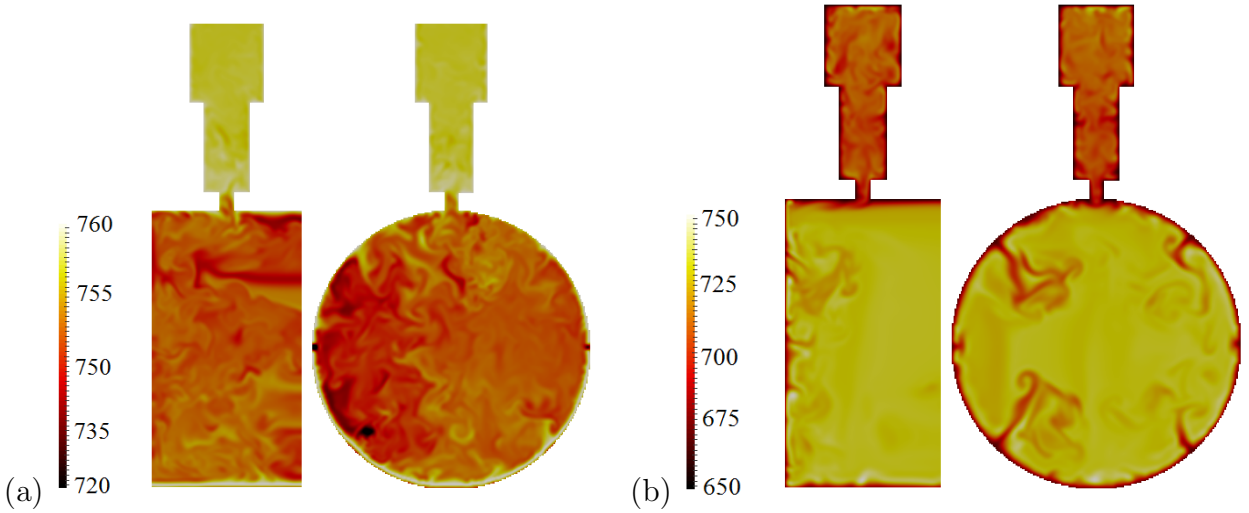


Figure 2.9: Temperature contours of TJI-assisted RCM at the end of the compression stage, piston located at TDC, for the cases with (a) adiabatic and (b) conductive walls.

In figure 2.10 the predicted MCh and PCh pressure traces during the compression stage are compared with the available experimental data [26]. It can be observed that the numerical

and experimental pressure values are very close throughout the compression phase before TDC ($t \approx 28 \text{ ms}$). This trend continues up to the ignition point ($t \approx 36 \text{ ms}$) when the conductive walls are used. As expected, the pressure stays constant between TDC and ignition when adiabatic walls are used. The experimental and numerical pressures at the ignition point are less than 2% different for the case with adiabatic walls and less than 0.3% different for the case with conductive walls.

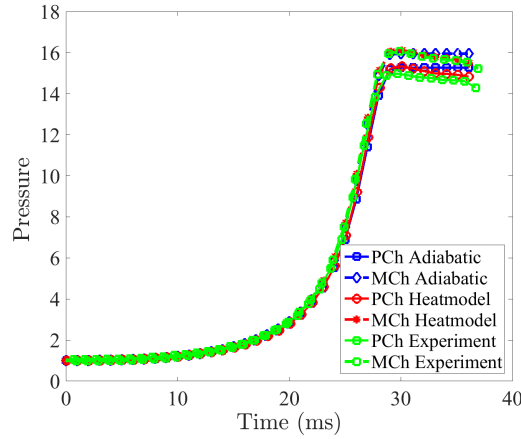


Figure 2.10: Quantitative comparison of the predicted pressures of both cases using adiabatic and conductive walls with available experimental data during the compression stage of the TJI-RCM.

2.5.2 Combustion phase

In the TJI-assisted RCM, the transition from a (non-reacting) compressed flow to a reacting flow is very fast and complex. The combustion is usually initiated by a spark plug installed inside the PCh. The PCh ignition process is a crucial phase in stabilizing a flame and it depends, rather very significantly, on the turbulence intensity and mixture homogeneity levels [54]. A successful flame kernel initiation does not necessarily lead to a stable flame and a successful TJI-assisted combustion. For instance, flame kernels may be generated, but then the flame in the PCh may be blown off due to intensive flow/turbulence and high strain

rate structures [5]. Here, the igniter is modeled by an energy deposition model (EDM) [54], in which the following source term, Q_{ig} , an exponential function of both space and time, is used in the energy equation.

$$Q_{ig} = \bar{\rho} \frac{\varepsilon}{4\pi^2 \Delta_{ig}^3 \tau_{ig}} \exp\left(-\frac{1}{2} \frac{(X_i^+ - X_{ig})^2}{\Delta_{ig}^2}\right) \exp\left(-\frac{1}{2} \frac{(t - t_m)^2}{\tau_{ig}^2}\right). \quad (2.35)$$

Here, ε is the total amount of energy deposited in the vicinity of the spark plug with the diameter Δ_{ig} for the time period of τ_{ig} and X_i^+ and X_{ig} are the MC particle and spark plug locations, respectively. In the FD-based LES, sub-grid scale (SGS) models have to capture the spark effects on the gas mixture as the ignition energy has to be discharged in an area smaller than the LES filter size. However, in the LES/FMDF model this energy is deposited on the MC particles, which can capture the local effects. The modeled igniter diameter Δ_{ig} is suggested [54] to be set equal to three times of the experimental spark plug clearance gap ($3 \times 0.8mm$). It is found that the same amount of energy reported to be generated by the spark plug in the experiments is sufficient for a successful ignition. The duration of the deposition is $200\mu s$. The main experimental spark and the EDM parameters are provided in table 2.2.

Table 2.2: Igniter parameters used in experiment and energy deposition model (EDM).

	Energy amount (mJ)	Duration (μs)	Spark width (mm)
Experimental	150	200	0.8
EDM	150	200	2.4

Figure 2.11 shows the variations of zy -plane averaged temperature (solid blue line), and fuel mass fraction (dashed red line), at the orifice in time marked by the direction of the streamwise filtered velocity component, \bar{u} . The jet moving from the PCh into the MCh (i.e. $\bar{u} \geq 0.0$) is shown by yellow squares ■ and the jet going in opposite direction from the MCh

into the PCh (i.e. $\bar{u} \leq 0.0$) is shown by green circles ●. The streamwise jet velocity values at the orifice are also displayed on the temperature plot. The results in this figure represent the overall behavior of TJI-RCM flow, as well as the mixture composition and directions of the developed jets passing through the orifice from/to the MCh. Note that figure 2.11 and also figures 2.12-2.14 represent the results corresponding to Case1 with the thermo-chemical conditions shown in table 2.3. Three main phases are delineated in the TJI-assisted RCM combustion stage. The detailed features of each phase may vary for different thermo-chemical conditions, but the overall characteristics are believed to remain the same. These combustion phases have been identified as i) cold fuel jet phase, ii) turbulent hot product jet phase, and iii) reverse fuel-air/product jet phase. The important features of each phase are described below.

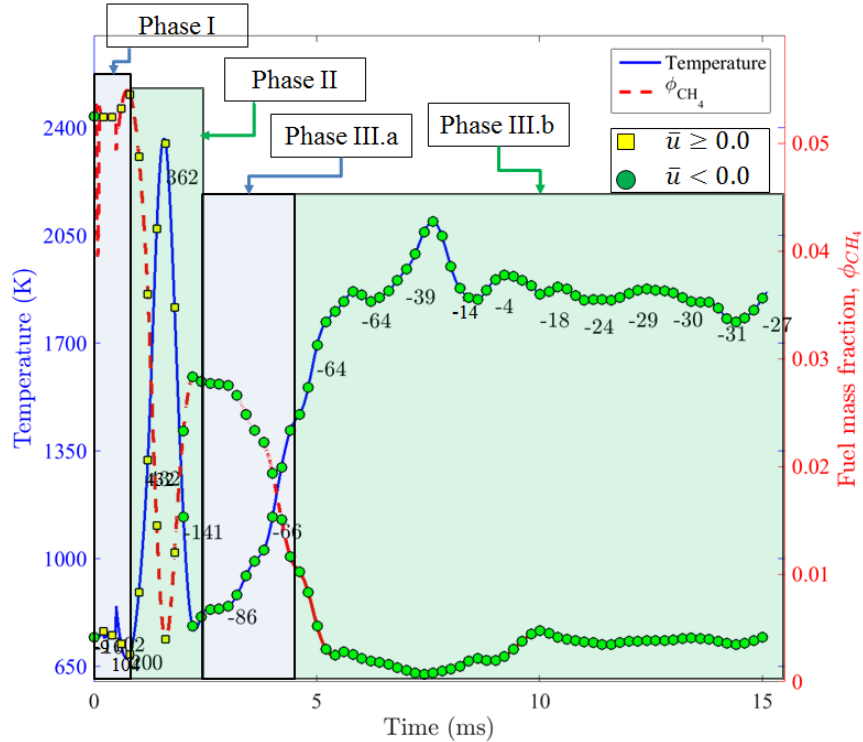


Figure 2.11: TJI-RCM combustion phases based on the composition and direction of the flow at the nozzle.

I. Cold fuel jet phase:

The first phase of the TJI-RCM combustion stage consists of the ignition, expansion of gas, and formation of the unburned fuel jet. It can be observed in figure 2.11(Phase I) that at early part of this phase, while the energy is being discharged by the igniter, sudden temperature and density changes cause some flow and fluctuations in the mixture variables as a low velocity stream at the orifice from the MCh to the PCh is generated. These insignificant fluctuations which are mainly dependent on the amount and the duration of the discharged energy, vanish rapidly and may not affect the main combustion. Having a successful ignition process, turbulent flames form and propagate throughout the PCh and, accordingly, the PCh pressure rise causes the cold fuel jet to push through the orifice into the MCh. Figure 2.11(Phase I) shows the properties of the cold fuel jet at the orifice; temperature of $T \simeq 750K$, fuel mass fraction of $\phi_{CH_4} \simeq 0.05$, and streamwise velocity of $0.0 \leq \bar{u} \leq 200$ (m/s). This is also observed in figures 2.12(a) and 2.12(b), where the velocity magnitude iso-surfaces colored by the fuel mass fraction and temperature are shown. Evidently, a relatively cold and high fuel concentration jet (in comparison to the MCh) indeed passes the orifice. As it can be observed in figure 2.12(a), the fuel mass fraction in PCh is higher than that in MCh. Since the fuel mass fraction of the cold fuel jet is the same as the PCh fuel mass fraction, it can be easily distinguished from the MCh in figure 2.12(a). However, the temperature of PCh and MCh are almost the same and tracking the cold fuel jet based on its temperature (figure 2.12b) may not be trivial. The main characteristics of this jet are dependent on the PCh composition and turbulence intensity as well as the parameters involved in the ignition. For example, higher equivalence ratio and turbulence intensity in the PCh generally lead to higher velocity of the cold fuel jet.

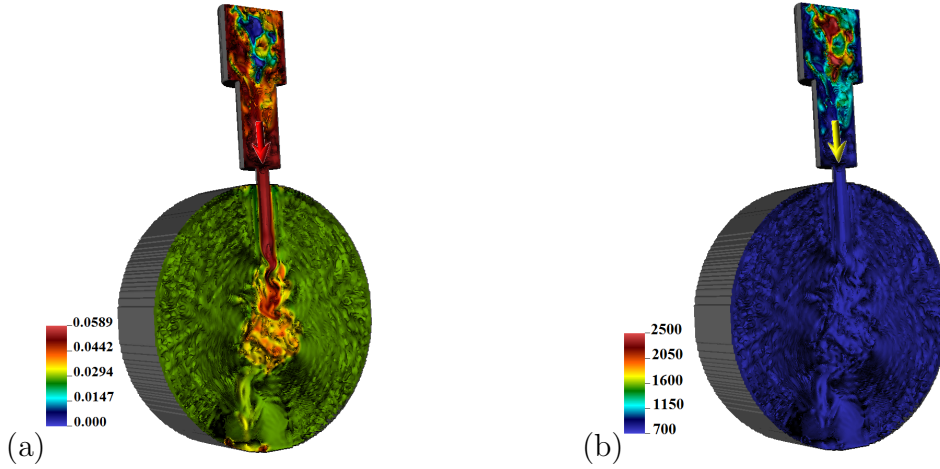


Figure 2.12: The first phase of the TJI-assisted RCM combustion stage. Instantaneous iso-surfaces of velocity magnitude colored by (a) fuel mass fraction, ϕ_{CH_4} , and (b) Temperature, T , at $t = 1.0$ (ms)

The amount of fuel leaving the PCh to the MCh is an important factor in designing the auxiliary air and fuel injectors. The main role of the auxiliary fuel injector is to improve the PCh combustion initiation by increasing the equivalence ratio. Ideally, all the existing fuel inside the PCh has to participate in the PCh combustion. However, in practice some of the auxiliary fuel does not participate in the PCh combustion and is simply added to the MCh charge. This fuel might help the combustion in MCh, but it usually has little effect and it is better to be burned inside the PCh. As explained in the next section, locating the igniter close to the nozzle inside the PCh prevents cold fuel leaving the PCh, which enables the ultra-lean premixed combustion and lowers the low flammability limit of premixed combustion.

II. Turbulent hot product jet phase:

After a successful ignition, during the evolution of the PCh combustion, a turbulent hot product/fuel jet is developed passing through the orifice from the PCh to the MCh. The features of this jet, which are effected by various parameters including PCh and MCh

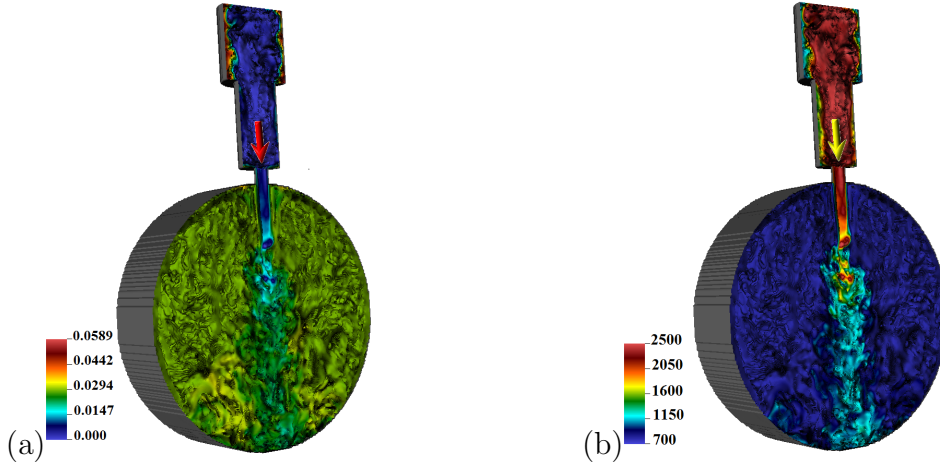


Figure 2.13: The second phase of the TJI-assisted RCM combustion stage. Instantaneous iso-surfaces of velocity magnitude colored by (a) fuel mass fraction, ϕ_{CH_4} , and (b) Temperature, T , at $t = 2.5$ (ms)

thermo-chemical conditions, are important to the MCh combustion. Unlike the cold fuel jet, the hot product jet can also be identified by the velocity magnitude iso-surfaces colored by temperature. It can be seen in figure 2.11 that the jet temperature, rapidly, increases from $T \simeq 750$ K up to $T \simeq 2400$ K and the fuel mass fraction drops to zero in Phase II. Initially, the jet velocity, rapidly, increases and reaches to very high values (about $500(m/s)$) at the orifice due to the high PCh-MCh pressure differences. Later on when the MCh combustion is initiated, the jet confronts relatively higher pressure zones in the MCh, while the PCh combustion becomes less effective, therefore, the driving force to sustain the high velocity hot product jet is, quickly, weakened. Figures 2.13(a) and 2.13(b) show the jet composition and temperature, when it hits the lower section of the MCh.

III. Reverse fuel-air/product jet phase.

The hot product turbulent jet developed in the phase II provides high energy content ignition sites throughout the MCh. Since the fuel-air mixture residence time is

relatively higher at the lower section of the MCh, combustion mainly starts at this location. During the MCh combustion, expectedly, MCh temperature and consequently its pressure increase, unevenly, in all directions; developing inverse jets from the MCh to the PCh. This phase can be divided into two sub-phases, based on the composition and temperature of the reverse jets. Ideally, the entire amount of the available fuel must be consumed in the main chamber. However, as it also can be observed in Phase III.a part of figure 2.11, an unburned fuel stream with relatively low temperature and velocity of about -100 m/s is passing the orifice from the MCh to the PCh. This sub-phase is also shown in figures 2.14(a) and 2.14(b). The inverse jet properties changes in time to higher temperatures and lower fuel mass fractions; as indications of a reverse hot product jet leaking into the PCh. The temporal variations of the composition, the temperature, and the velocity of this jet are shown in Phase III.b part of figure 2.11. As it can also be observed in figures 2.14(c) and 2.14(d), the transition from one inverse jet to the other depends on the MCh combustion.

It is expected that all the fuel in the MCh to be burned by the end of this phase, however, some of the unburned fuel leaked from the MCh to the PCh stay unburned for a long time and, negatively, affect the performance of the TJI-RCM system. Interestingly, at the very end of the TJI-RCM combustion stage, the remnant unburned fuel-air trapped in the PCh during the previous phases might generate a mixture of unburned fuel-air and product stream from the PCh to the MCh. Since the temperature of this jet is relatively high and its residence time is short, it burns quickly as it gets into the MCh. This jet might help with the combustion sustainability at the later times, however, it also stretches the end of TJI-RCM combustion stage. Preventing the fuel from escaping may not be trivial by controlling the thermo-chemical parameters.

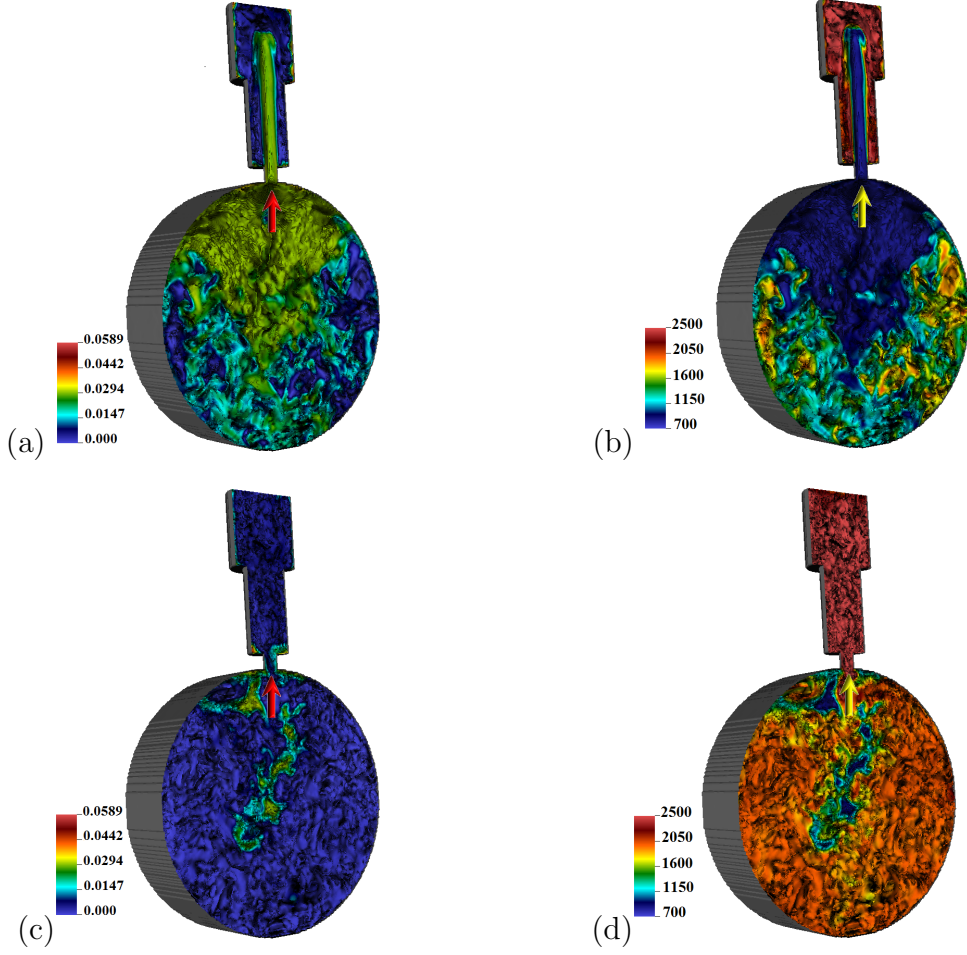


Figure 2.14: The reverse unburned fuel jet of the third phase of the TJI-assisted RCM combustion stage; instantaneous iso-surfaces of velocity magnitude colored by (a) fuel mass fraction, ϕ_{CH_4} , and (b) Temperature, T at $t = 4.0$ (ms). The reverse hot product jet of the third phase of the TJI-assisted RCM combustion stage; instantaneous iso-surfaces of velocity magnitude colored by (c) fuel mass fraction, ϕ_{CH_4} , and (d) Temperature, T , at $t = 8.0$ (ms).

However, as it is studied in Case10 to Case13 of table 2.3, lowering the location of the igniter shortens the combustion duration and also prevents the unburned fuel at the upper section of the MCh leaks into the PCh.

Here, we study the effects of various thermo-chemical and physical parameters as provided in table 2.3, which are categorized in three sets as a) initial condition and wall heat transfer model (Case1 to Case5), b) N_2 dilution and MCh and PCh equivalence ratios (Case6

to Case9), and c) igniter location (Case10 to Case13). The reference MCh and PCh compositions, $\phi_{MCh} = 0.485$ and $\phi_{PCh} = 0.787$, and the igniter location, $d_{ig} = 4$ (mm), have been chosen in the LES/FMDF simulations based on the available experimental data [110]. In the experiments after the piston reaches the TDC, the RCM is held untouched while the igniter is being charged. The effective time of the igniter energy discharge is observed to be about TDC+6 (ms), therefore, the simulation of the compression phase was continued. Accordingly, the thermo-hydrodynamics fields at TDC+6 (ms) are used as the initial conditions in the simulations, except in Case5 which the related fields at TDC are used.

Table 2.3: Thermo-chemical and physical parameters of simulated TJI-assisted RCM.

Case#	ϕ_{MCh}	ϕ_{PCh}	IC at t_{ig}	Wall HT	t_{ig} (ms)	$N_2\%$	d_{ig} (mm)
1	0.485	0.787	ideal	adiabatic	$t_{TDC}+6$	0.0	4
2	0.485	0.787	ideal	model	$t_{TDC}+6$	0.0	4
3	0.485	0.787	realistic	adiabatic	$t_{TDC}+6$	0.0	4
4	0.485	0.787	realistic	model	$t_{TDC}+6$	0.0	4
5	0.485	0.787	realistic	adiabatic	t_{TDC}	0.0	4
6	0.485	0.787	realistic	adiabatic	$t_{TDC}+6$	20.0	4
7	0.485	0.787	realistic	adiabatic	$t_{TDC}+6$	30.0	4
8	0.3	0.787	realistic	adiabatic	$t_{TDC}+6$	00.0	4
9	0.3	2.0	realistic	adiabatic	$t_{TDC}+6$	00.0	4
10	0.485	0.787	realistic	adiabatic	$t_{TDC}+6$	00.0	13
11	0.485	0.787	realistic	adiabatic	$t_{TDC}+6$	00.0	25
12	0.3	0.787	realistic	adiabatic	$t_{TDC}+6$	00.0	25
13	0.2	0.787	realistic	adiabatic	$t_{TDC}+6$	00.0	25

2.5.2.1 Comparison with experiment and parametric analysis

The corresponding simulation results in Case1 are utilized in figure 2.15 for a qualitative comparison between the available experimental data [110] and LES/FMDF temperature contours. The experimental images shown in figures 2.15(a_1)-(a_3) present the MCh luminosity for different time. Here, t_j is defined as the time where the tip of the hot product jet (both in experiments and numerics) reaches the middle of the MCh as it can be observed in figures 2.15(a_1), 2.15(b_1), and 2.15(c_1). The contrast and brightness of the color images

were enhanced using Image-J software [96]. In the experimental images the entire MCh in spanwise direction is captured. For the sake of better comparisons, figures 2.15(b_1)-(b_3) show the spanwise averaged of the simulated temperature contours, which are more similar to the experimental images. It might be challenging to capture the flow in a particular plane inside the MCh experimentally, but this can be easily done numerically. Figures 2.15(c_1)-(c_3) show the temperature contours in a plane located at the middle of the MCh which present more details of the highly turbulent hot product jet. It can be seen in figures 2.15(a_2), 2.15(b_2), and 2.15(c_2) that at the time $t_j + 0.2$ (ms) both the predicted and experimental hot product jets are reached to the lower part of the MCh. The predicted tip jet velocity, consistent with experiments, is about 125 (m/s) on average. After about $t_j + 0.4$, combustion is already initiated and propagated in both spanwise and cross stream directions (figures 2.15 a_3 , 2.15 b_3 , and 2.15 c_3). The qualitative comparison of these figures reveals the high accuracy of our numerical approach.

A quantitative comparison has also been made between the available experimental pressure data [110] and LES/FMDF pressures obtained from Case1 and Case2 provided in table 2.3. In figure 2.16, the experimental pressure trace is shown by (\diamond). The pressure transducer in the experimental setup is located at the lower section of the MCh. The simulated pressure values at the location of the pressure transducer, $Point_{MCh}$, are shown by (\circ) for Case1 and by (\square) for Case2. During the early phases of the TJI-RCM combustion, both experimental and numerical pressure values are reasonably in an accurate agreement. In the later phases, these two pressure traces deviate from each other. In the numerical point of view, this behavior might be due to the chemical kinetics model and/or wall condition used in the simulations. The discrepancies between the reported and actual initial experimental conditions including the initial fuel equivalence ratio, temperature, pressure, and auxiliary

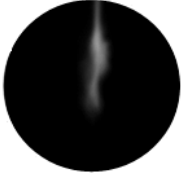
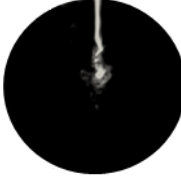

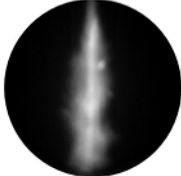
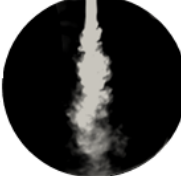

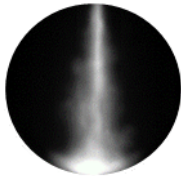
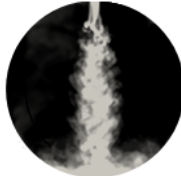
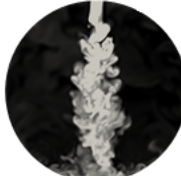
Time (ms)	Experimental image	LES/FMDF spanwise averaged	LES/FMDF mid-plane
t_j	 (a_1)	 (b_1)	 (c_1)
$t_j + 0.2$	 (a_2)	 (b_2)	 (c_2)
$t_j + 0.4$	 (a_3)	 (b_3)	 (c_3)

Figure 2.15: Qualitative comparison between LES/FMDF and experimental results: (a_1)-(a_3): Experimental pictures; (b_1)-(b_3): LES/FMDF span-wised averaged temperature contours at; and (c_1)-(c_3): LES/FMDF temperature contours in the middle of the MCh.

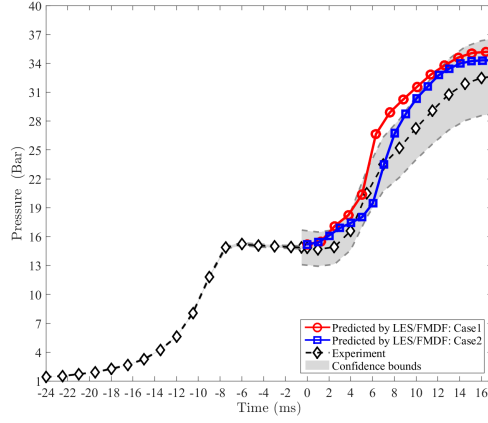


Figure 2.16: Comparing the experimental (\diamond) and simulated pressure traces at Point_{MCh} in Case1 (\circ) and Case2 (\square).

amount of fuel, as well as the possible leakage in the experimental setup might cause the pressure differences. The repeatability of the experimental pressure traces was examined repeating the experiments with the same conditions; an uncertainty factor equals to 10% from the mean values, reasonably, represent the possible aleatory and epistemic uncertainties. The experimental pressure confidence (uncertainty) bounds are shown by shaded gray area in figure 2.16. Despite of pressure differences, the simulated pressure traces, acceptably, follow the corresponding experimental values within the defined confidence bounds. In Case1 the adiabatic walls are used and the generated heat of combustion stays in the system and expectedly the predicted pressure is relatively higher. In Case2 where the heat transfer wall model is used, the maximum predicted pressure is lower than it in Case1 and closer to the experimental results. It can be seen that the TJI-assisted RCM combustion process is sensitive to the heat transfer model at the walls even for the same initial thermo-chemical conditions. More details are provided below.

Figure 2.17 shows the contours of temperature, fuel mass fraction, and velocity magnitude for Case1. In these and similar figures for all cases, the contours of each quantity at the

middle and side planes of the TJI-RCM are shown at different times, e.g. $t = t_{ig} + 0.5 \text{ (ms)}$, $t_{ig} + 02.0 \text{ (ms)}$, $t_{ig} + 05.0 \text{ (ms)}$, and $t_{ig} + 10.0 \text{ (ms)}$ in the same row. In Case1, the initial thermo-chemical conditions are set based on the experimental results. However, since the mixture is held at rest for a fairly long time, stagnant condition in MCh might be a reasonable assumption, however, due to the high turbulence level inside the PCh, turbulent fluctuations are initially added. These fluctuations are generated by solving the governing equations with periodic boundary conditions and an initially random, solenoidal, and Gaussian velocity field for a long time [116]. The maximum values of the velocity components are within the 10% of the initial hot product jet velocity passing the nozzle (e.g. 300 (m/s)). The walls are assumed to be adiabatic. It can be seen that within 0.5 (ms) the ignition process is completed and the cold fuel jet is reached to the middle section of the MCh, suggesting that less amount of cold fuel is exiting out to the MCh and more fuel participates in the PCh ignition processes. After 2 (ms) a highly turbulent hot product jet is already developed and reached the lower section of the MCh initiating its combustion. The MCh combustion generates vortex shape structures which eventually propagate in the entire domain and lead to a nearly volumetric combustion. As it can be seen after 10 (ms) the MCh and PCh combustion are completed.

The thermo-chemical and hydrodynamic conditions used in simulating Case2 are the same as those used in simulating Case1. However, in this case the conductive heat transfer model (equation 2.33) is used to calculate the wall temperatures. It can be seen in figure 2.18 that even though the combustion is completed by 10 (ms) , it is generally delayed. The jet is already reached to the lower section of the MCh and combustion is initiated by 2 (ms) after ignition, but the flame propagates less in comparison to Case1. Also after 5 (ms) the reverses cold fuel jet is developed, but high temperature zones in the MCh are less developed.

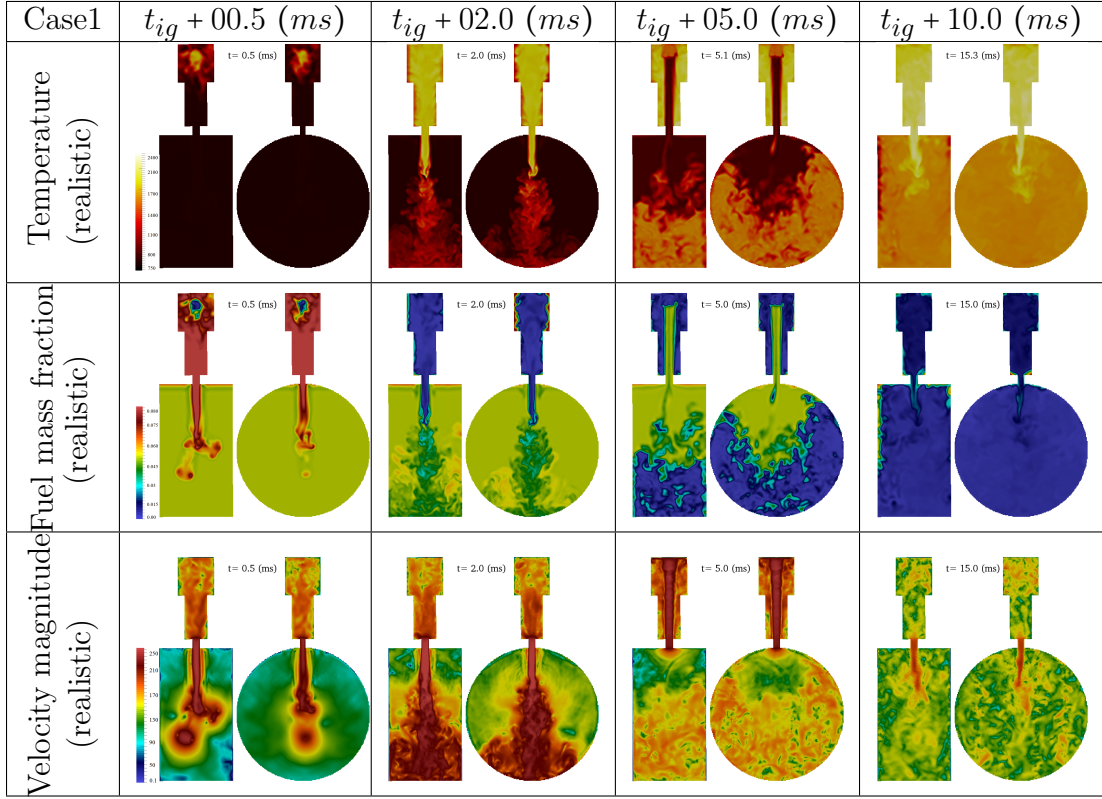


Figure 2.17: Temporal evolution of simulated temperature, T , fuel mass fraction, ϕ_{CH_4} , and velocity magnitude, $|\vec{U}|$ (m/s), contours for Case1.

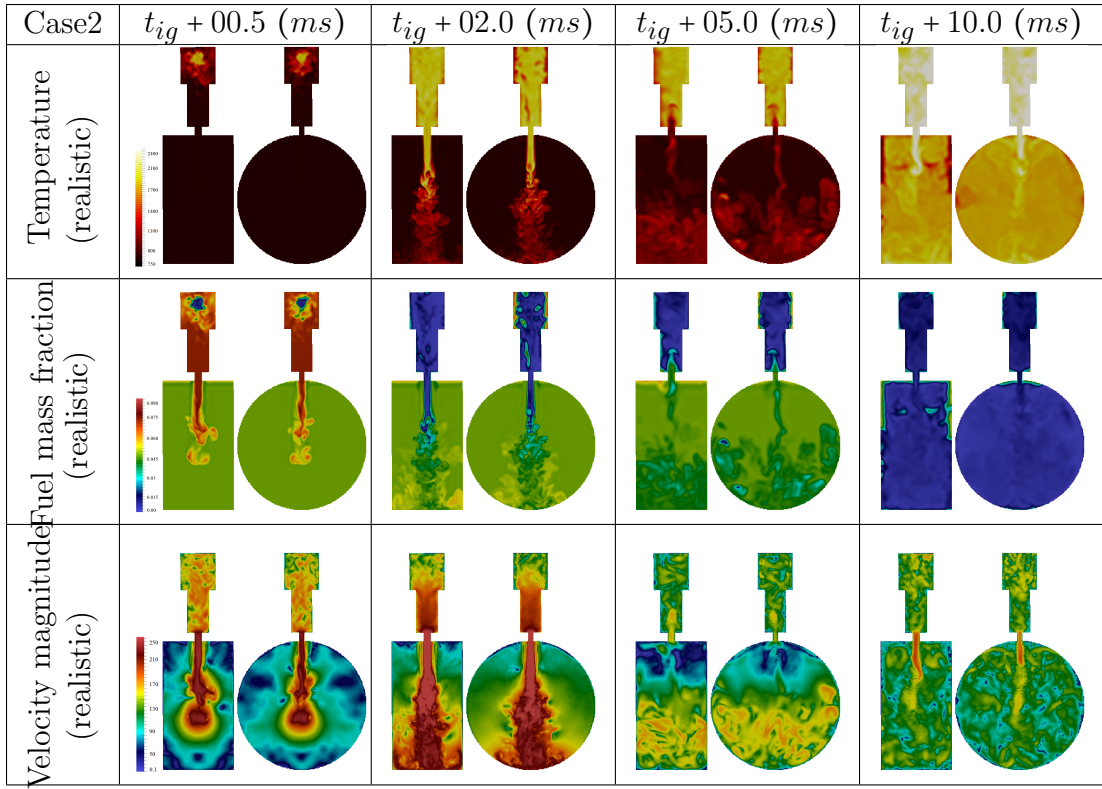


Figure 2.18: Temporal evolution of simulated temperature, T , fuel mass fraction, ϕ_{CH_4} , and velocity magnitude, $|\vec{U}|$ (m/s), contours for Case2.

Figure 2.19 shows the contours of temperature, fuel mass fraction, and velocity magnitude for Case3. In this case, consistent with the experiments, the simulation of the compression phase is continued for another 6 (*ms*) after the piston reaches to the TDC. Within this time-lag the MCh and PCh turbulences relax, which might allow the spark plug to better ignite the PCh charge, but it negatively affects the flame speed and pressure rise inside the PCh during the ignition process. After 0.5 (*ms*) the PCh ignition process is not completed and the cold fuel jet is exiting out to the MCh. About 2 (*ms*) after ignition, a hot product turbulent jet hits the lower part of the MCh and initiates the main combustion. Due to the pressure rise of the MCh a reverse cold fuel jet is getting into the PCh at about 5 (*ms*). Within 10 (*ms*) the combustion is fairly completed and all available fuel inside the system is consumed. As it can be seen in $|\vec{U}|$ (*m/s*) contours there are fluctuations at the nozzle between MCh and PCh which balance the pressure of both chambers.

Figure 2.20 shows the contours of temperature, fuel mass fraction, and velocity magnitude for Case4. In this case the wall temperatures are calculated based on the conductive heat transfer model (equation 2.33). The compression simulation using wall heat transfer model was continued for extra 6 (*ms*) after the piston reaches the TDC and the final flow field is used as the initial hydrodynamics condition. The fuel mass fraction inside the MCh and PCh are the same as them in Case3. As it can be seen in temperature and fuel mass fraction contours in figure 2.20, the PCh ignition process takes longer about 2 (*ms*) mainly due to the heat loss of the PCh. The combustion was already initiated before 5 (*ms*) but at this time, compare to previous cases, less amount of the MCh charge participated in the combustion, confirming the effects of the heat loss of the MCh. Even though the combustion is completed after 10 (*ms*), the entire process of combustion is, reasonably, delayed in this case due heat loss across the MCh and PCh walls.

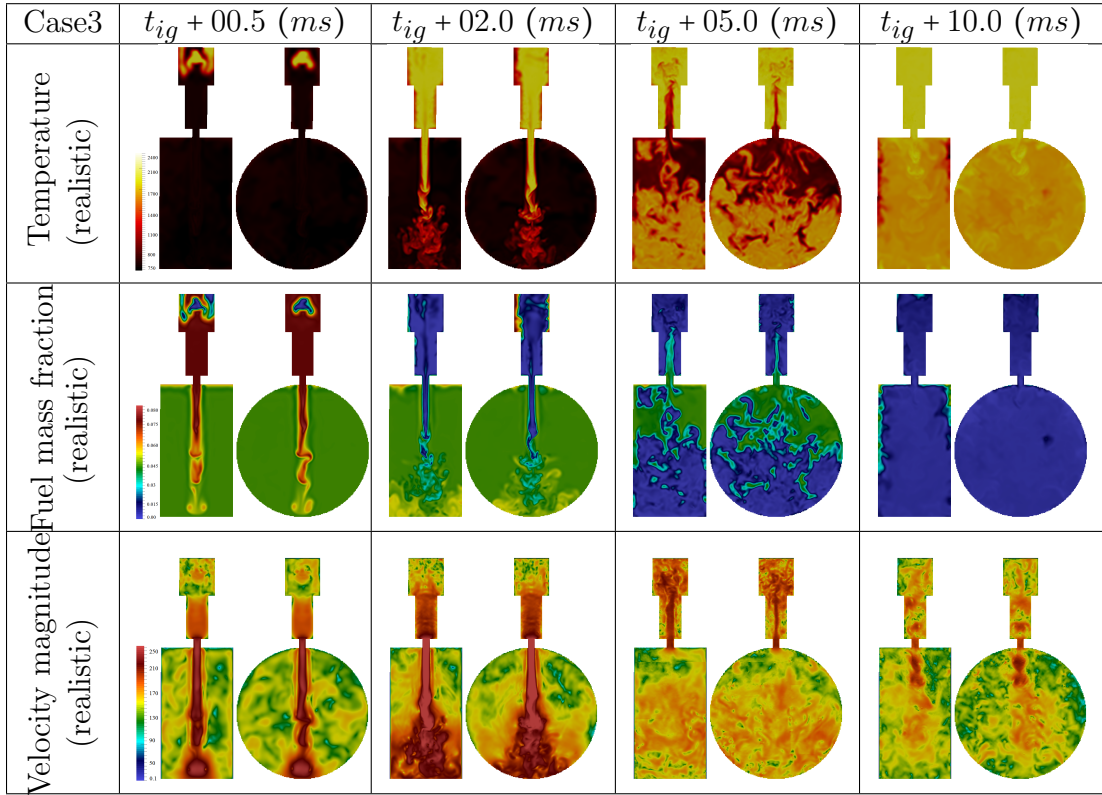


Figure 2.19: Temporal evolution of simulated temperature, T , fuel mass fraction, ϕ_{CH_4} , and velocity magnitude, $|\vec{U}|$ (m/s), contours for Case3.

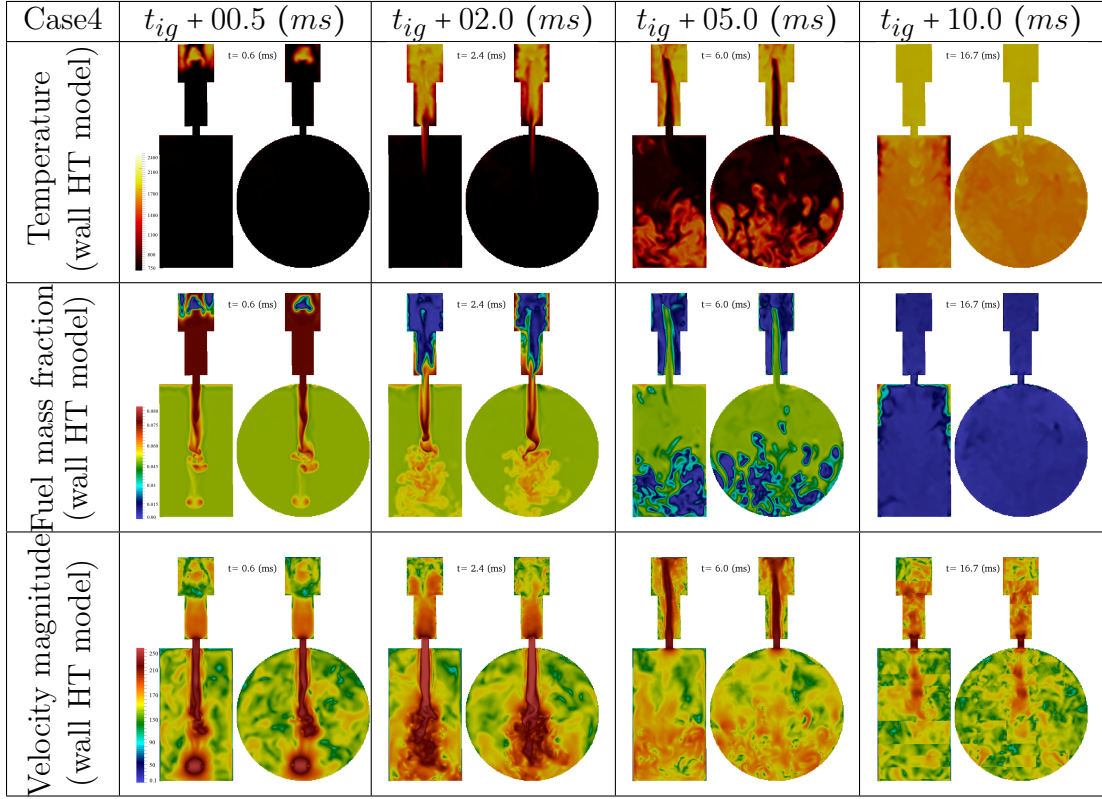


Figure 2.20: Temporal evolution of simulated temperature, T , fuel mass fraction, ϕ_{CH_4} , and velocity magnitude, $|\vec{U}| \text{ (m/s)}$, contours for Case4.

Figure 2.21 shows the contours of temperature, fuel mass fraction, and velocity magnitude for Case5. In this case the ignition timing is shifted to the time when the piston stops at the TDC. At this time, the initial turbulence inside both MCh and PCh is relatively higher than it in Case3 which, ultimately, generates higher velocity hot product jet at the earlier times and combustion is initiated faster. However, conducting this case might be difficult experimentally, since the spark plug must initiate the PCh combustion in a higher level turbulence. This issue might be addressed by discharging more energy for a longer time during the PCh ignition process. As it can be seen in figure 2.21, the PCh ignition process in the upper section of the PCh is completed within 0.5 (*ms*) and the MCh combustion is initiated by 2 (*ms*). The hot product jet velocity is relatively higher than it in Case3 due to faster ignition processes and rapid pressure rise in the PCh. Expectedly, the MCh combustion is completed by 10.0 (*ms*).

The main difference in Case2 to Case5 is the initial hydrodynamics condition, therefore the corresponding results for these simulations are analyzed together. In figure 2.22(a) the simulated pressure traces in Pch (dashed thin lines) and Mch (solid thick lines) versus time for Case3 (◻), Case4 (◻), and Case5 (✱) are shown. In figures 2.22(b)-(e) the simulated temperature (blue solid lines) and fuel mass fraction (red dashed lines) at one point located at a point in the nozzle exit in the MCh side versus time for Case2 to Case5 are presented which the streamwise velocity values are assigned to the temperature plot. This format is also used later in figures 2.27 and 2.32 for Case6 to Case9 and Case10 to Case13. Initially a local pressure rise can be observed in PCh pressure during the ignition process. This pressure rise, which determines the velocity of both cold fuel and hot product jets, is highly dependent on the initial PCh turbulence and wall heat transfer. In Case5, since the PCh turbulence is relatively higher, the larger pressure rises in the PCh are observed.

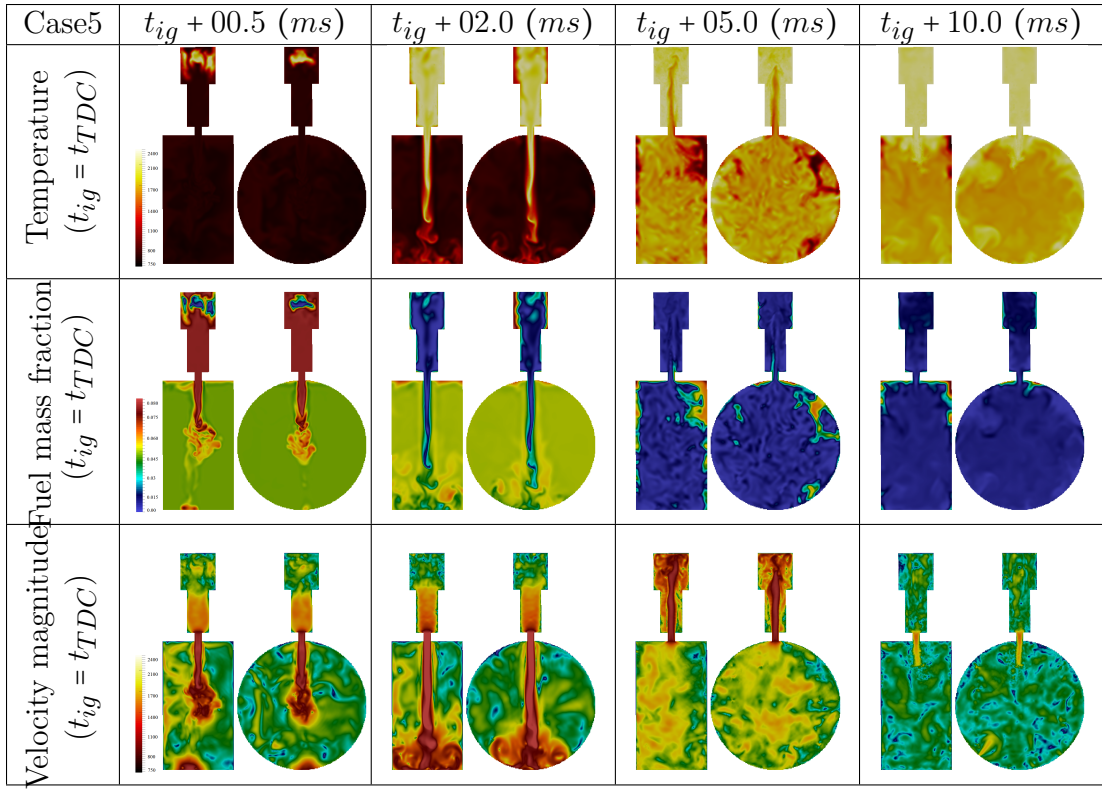


Figure 2.21: Temporal evolution of simulated temperature, T , fuel mass fraction, ϕ_{CH_4} , and velocity magnitude, $|\vec{U}|$ (m/s), contours for Case5.

When the hot jet reaches the lower sections of the MCh and initiates the main combustion, expectedly, the MCh pressure rises. The pressure difference between MCh and PCh drives the MCh mixture at the upper sections (unburned mixture) into the PCh. Eventually, when combustion is completed, both pressures reaches to the same level. As it can be observed in figures 2.22(b)-(e), this behavior is valid in all cases, except in Case2 and Case4 which the heat loss is more than it in other cases and, accordingly, the final temperature and pressure are slightly lower. The initial cold fuel jet can be delineated by the flow characteristics at a point inside the domain close to the nozzle. It can be observed in figures 2.22(b)-(e) that the high level ϕ_{CH_4} and low temperature (≈ 750 (K)) passes through this point with relatively low magnitude negative streamwise velocity values. The duration of this phase, expectedly, is shorter in Case2 and Case5 and longer in Case4. After the completion of the PCh ignition process, the hot turbulent jet exits out to the MCh. The velocity of this jet is dependent on the ignition process. The highest velocity magnitudes, 509 (m/s) and 418 (m/s), occurred in the Case2 and Case5 in which the PCh ignition timing is shorter. Due to the same thermo-chemical conditions, the MCh combustion takes place, fairly, in the same time, except for Case4 which occurs over a longer period of time due to MCh heat release through the walls.

In the second set of the simulations we study the effects of initial thermo-chemical conditions on the combustion processes by diluting the original mixture with 20% N_2 and 30% N_2 in Case6 and Case7 and lowering the MCh equivalence ratio to 0.3 in Case8. Also the effect of rich PCh and unburned fuel inside the hot product jet is studied in Case9 by adding extra fuel to the PCh composition and provide a rich PCh with $\phi_{PCh} = 2.0$. Figures 2.23 and 2.24 show the contours of temperature, fuel mass fraction, and velocity magnitude for Case6 and Case7, respectively. Fairly similar PCh ignition process and MCh combustion initiation is

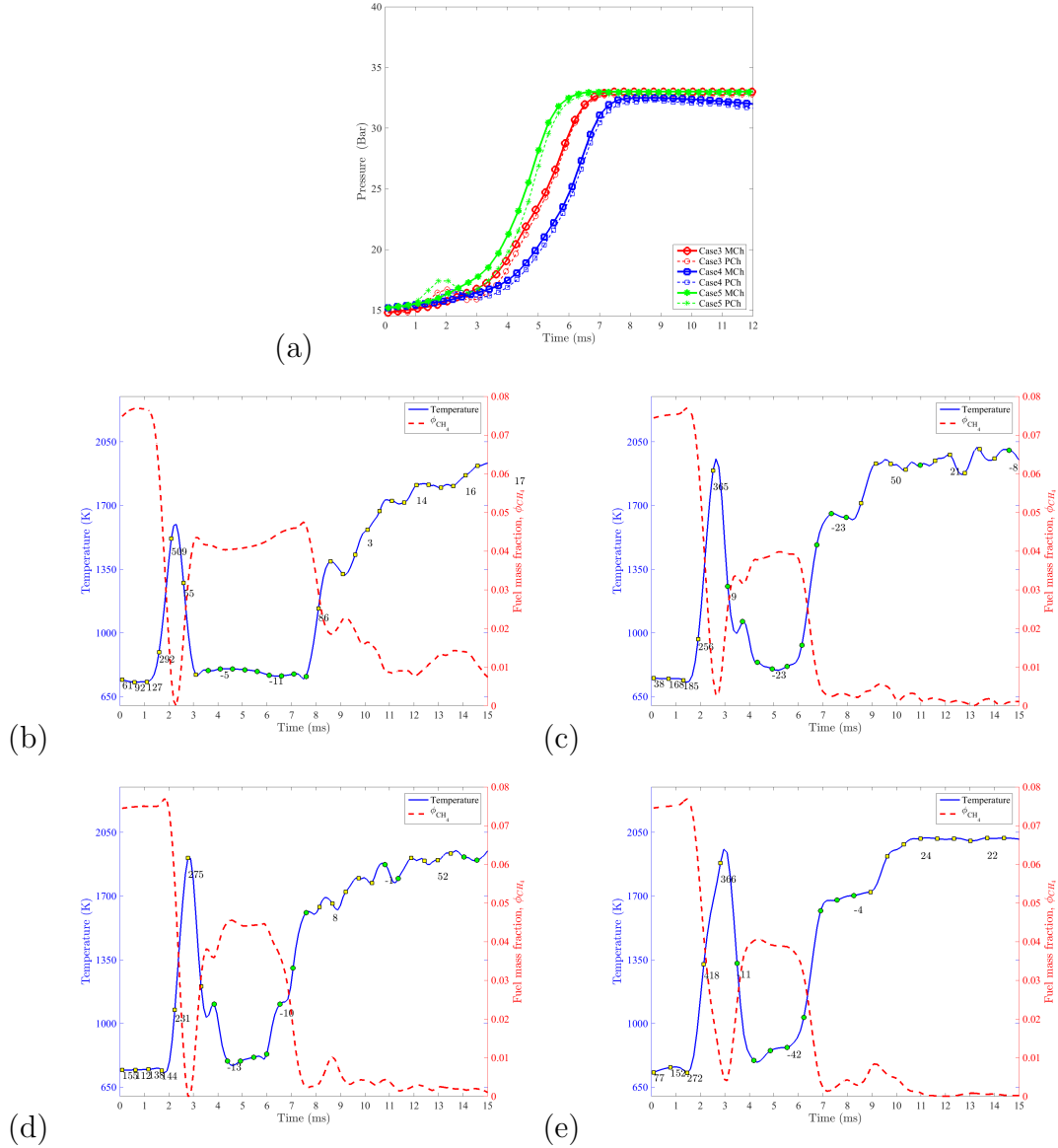


Figure 2.22: (a) Simulated pressure traces in Pch (dashed thin lines) and Mch (solid thick lines) versus time for Case3 (\circ), Case4 (\square), and Case5 (\times). (b)-(e) Simulated temperature (blue solid lines) and fuel mass fraction (red dashed lines) at a point in the nozzle exit in the MCh side versus time for Case2 to Case5. The streamwise velocity values are also shown.

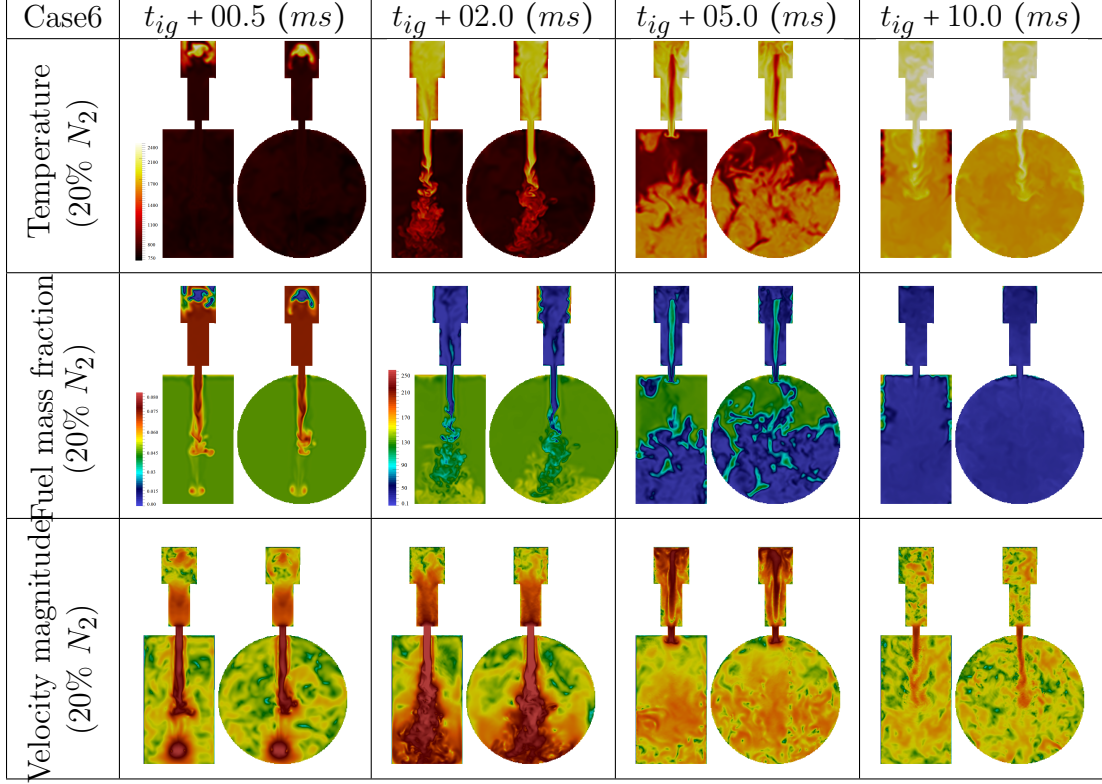


Figure 2.23: Temporal evolution of simulated temperature, T , fuel mass fraction, ϕ_{CH_4} , and velocity magnitude, $|\vec{U}|$ (m/s), contours for Case6.

observed in these cases, however, the MCh combustion process is delayed more in Case7, due to existence of more N_2 in the MCh. It can be seen in figure 2.23 after 5 (ms) the flame propagates throughout the MCh leading to the combustion completion. However, figure 2.24 for the same time reveals that the flame propagates in the lower side of the MCh and sustains the combustion in this area. It also can be seen that the combustion is completed in both cases after 10 (ms).

Figure 2.25 shows the contours of temperature, fuel mass fraction, and velocity magnitude for Case8, in which the MCh equivalence ratio is equal to 0.3. Since the PCh thermo-chemical and hydrodynamics is the same as Case3, the similar ignition process occurs. However, the lean MCh affects on the initiation of the MCh combustion. As it can be seen after 5 (ms) ignition, a weak combustion is initiated and most of the MCh charge stays unburned.

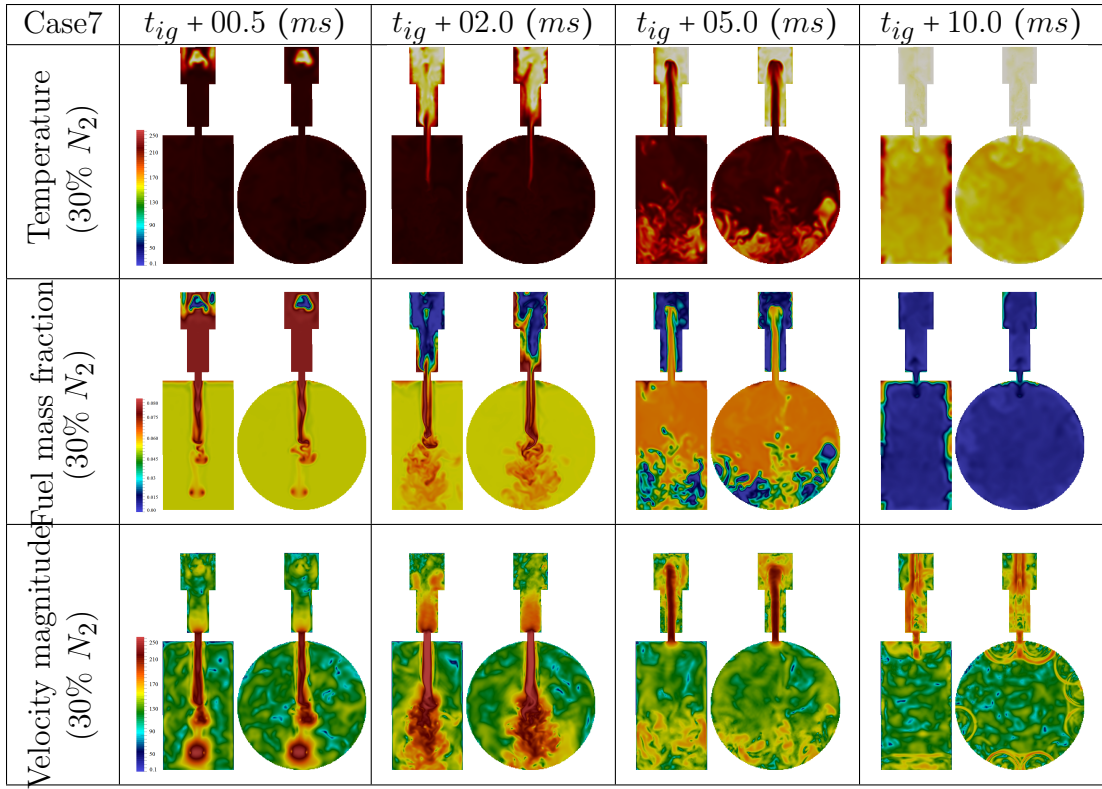


Figure 2.24: Temporal evolution of simulated temperature, T , fuel mass fraction, ϕ_{CH_4} , and velocity magnitude, $|\vec{U}|$ (m/s), contours for Case7.

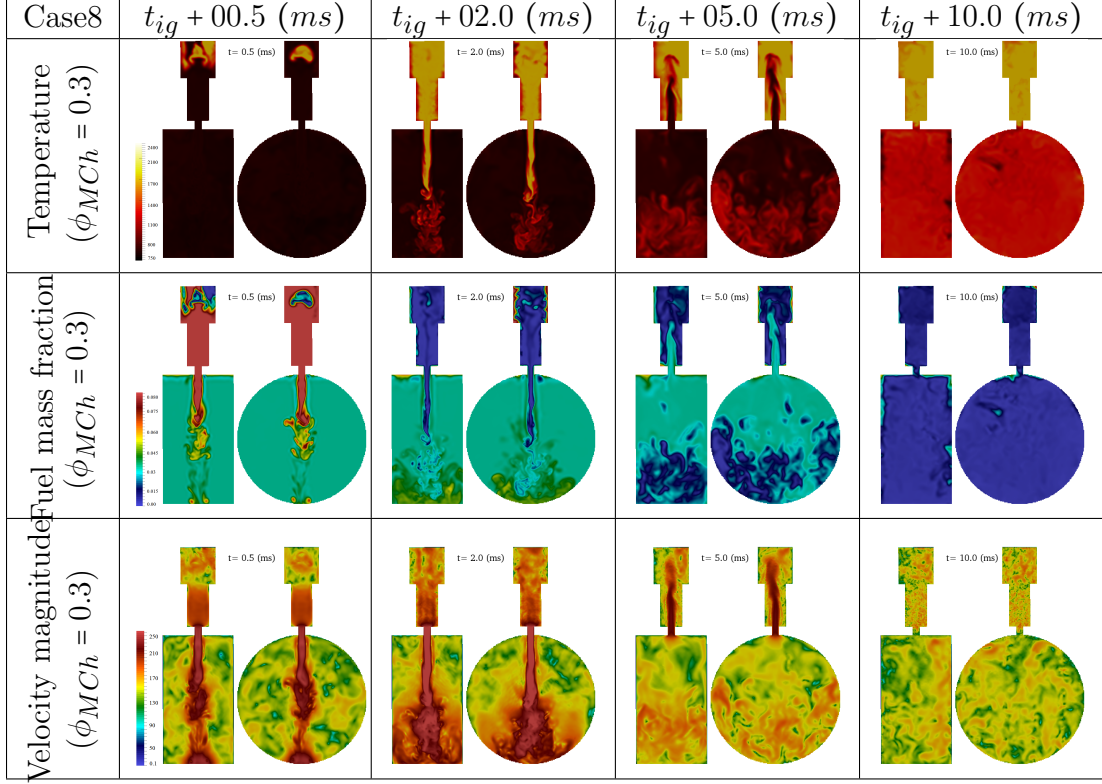


Figure 2.25: Temporal evolution of simulated temperature, T , fuel mass fraction, ϕ_{CH_4} , and velocity magnitude, $|\vec{U}|$ (m/s), contours for Case8.

However the combustion is completed after 10 (ms), expectedly, with lower temperature.

Figure 2.26 shows the associated contours for Case9. In this case the PCh composition consists of a rich premixed fuel-air mixture, $\phi_{PCh} = 2.0$. The ignition process takes more than it in the other cases since the flame temperature of the rich mixture is relatively lower. It can be seen in figure 2.26 that after 2 (ms) the hot product jet is not yet developed. Fuel contours reveal that the most of the fuel inside the PCh exits out to the MCh during the ignition process, which may change the leanness of the MCh composition. It can be seen after 5 (ms) of the ignition the hot jet is developed and getting into the MCh. However, the composition of this jet consists of products and also unburned fuel. This amount of fuel might help to initiate the MCh combustion, but the jet temperature is relatively lower and delays the MCh combustion. It can be seen that after 5 (ms) the MCh combustion is

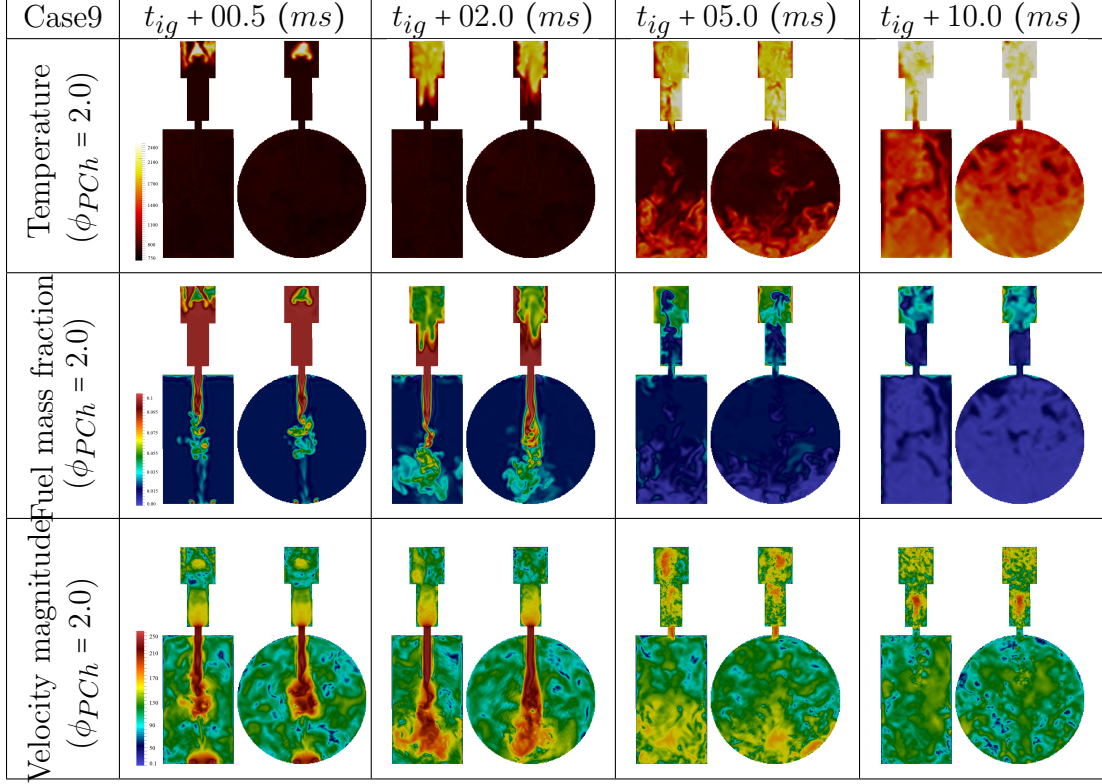


Figure 2.26: Temporal evolution of simulated temperature, T , fuel mass fraction, ϕ_{CH_4} , and velocity magnitude, $|\vec{U}|$ (m/s), contours for Case9.

initiated at the lower sections with considerable amount of unburned fuel inside the PCh and MCh. Eventually, the entire fuel participates in either PCh or MCh combustion.

Since the initial hydrodynamics conditions are the same in Case6 to Case9 and the main differences are related to their compositions, the results of these cases are analyzed here. In figure 2.27(a) the simulated pressure traces in Pch (dashed thin lines) and Mch (solid thick lines) versus time for Case6 (\square), Case7 (\circ), Case8 (\star), and Case9 (\times) are shown. It can be observed that the initial pressure rise in PCh is the same in Case6 to Case8 and it is delayed in Case9. The MCh combustion and pressure rise is also delayed in all cases. The maximum pressure drops in Case6 to Case9. However, maximum pressure in Case9 is slightly higher than it in Case8, since the extra amount of fuel inside the PCh, eventually, participates in the combustion processes. In figures 2.27(b)-(e) the simulated temperature

(blue solid lines) and fuel mass fraction (red dashed lines) at a point in the nozzle exit in the MCh side versus time for Case6 to Case9 are presented which the streamwise velocity values are assigned to the temperature curves. Fairly similar behavior are observed for Case6 to Case9. And in Case9 the fuel mass fraction of the cold fuel jet is considerably higher than it in other cases and it is exiting out to the MCh for slightly longer time.

The main idea of TJI-assisted combustion is, constantly, exposing a lean mixture to a hot jet. As we have seen in the previous cases, initially, during the ignition process a cold fuel jet is developed and exits out to the MCh and might change the leanness of the lean MCh. This fuel, ideally, must participate in the PCh ignition and combustion processes. This jet is a cold jet and it unlikely helps the initiation of the MCh combustion, however, it participates in the MCh combustion later if the combustion is sustained. In order to prevent the cold fuel jet from getting into the MCh and also force it to participate in the PCh combustion process, we suggest to change the location of the igniter, which is also possible experimentally. Lowering the igniter location leads to combustion initiation in the middle (or low) sections of the PCh. The mixture at the upper sections of the PCh is trapped in by the premixed flames around the igniter location and gradually is fed to the reacting zones developed during the PCh ignition and combustion processes. At the same time, a hot product jet gets out of the PCh into MCh. In this approach the main goal of TJI-assisted combustion is satisfied by developing a hot jet for a longer time, which, eventually, allows to lower the low flammability limit of the premixed combustion.

Here, we study the combustion processes of the TJI-assisted RCM by changing the igniter locations. Figures 2.28 and 2.29 show the contours of temperature, fuel mass fraction, and velocity magnitude for Case10 and Case11, in which the igniter distances from the top of the PCh are $d_{ig} = 13 \text{ (mm)}$ and $d_{ig} = 25 \text{ (mm)}$, respectively. As it can be seen in figure 2.28

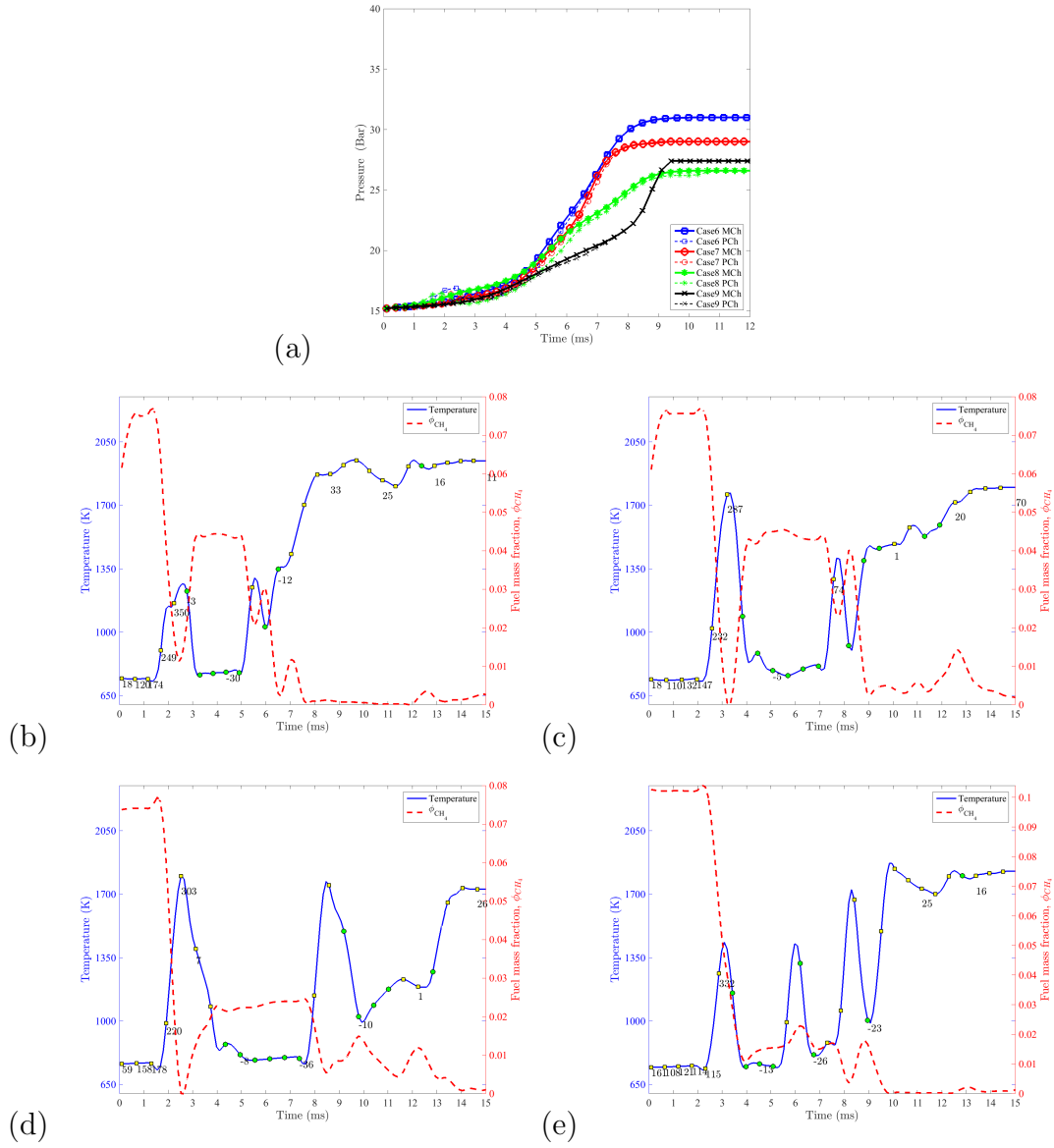


Figure 2.27: (a) Simulated pressure traces in Pch (dashed thin lines) and Mch (solid thick lines) versus time for Case6 (\square), Case7 (\circ), Case8 (\times), and Case9 (\times). (b)-(e) Simulated temperature (blue solid lines) and fuel mass fraction (red dashed lines) at a point in the nozzle exit in the MCh side versus time for Case6 to Case9. The streamwise velocity values are also shown.

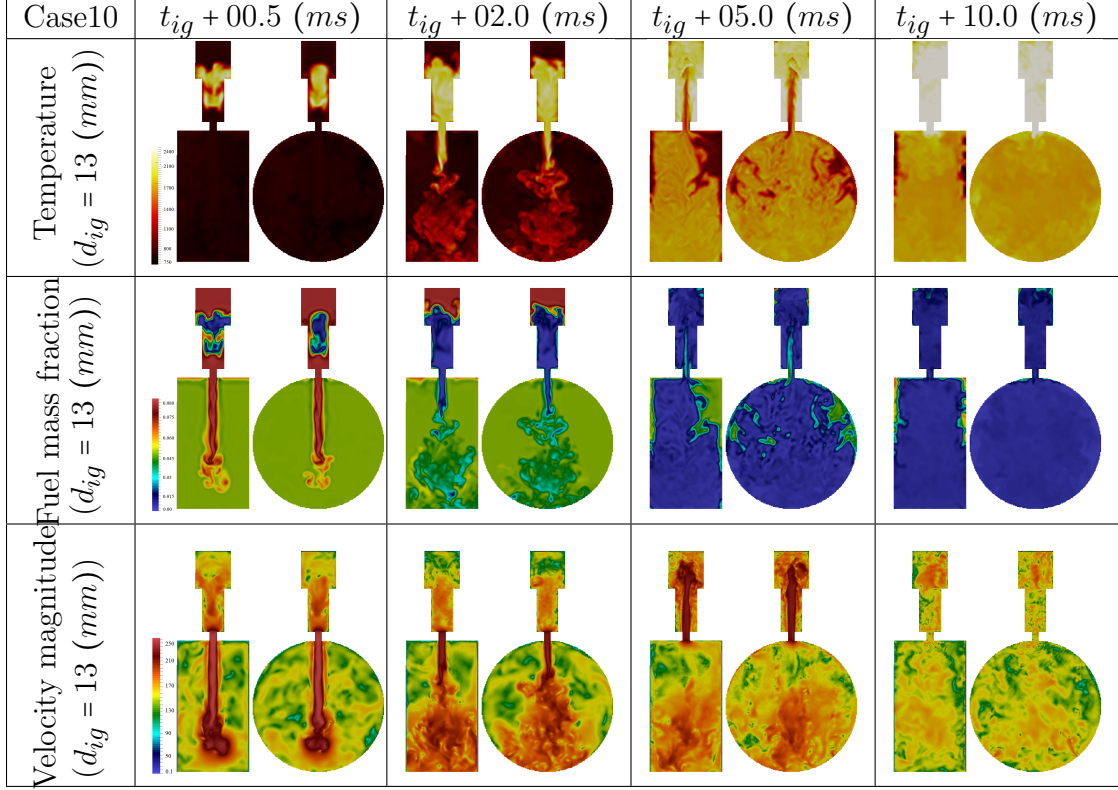


Figure 2.28: Temporal evolution of simulated temperature, T , fuel mass fraction, ϕ_{CH_4} , and velocity magnitude, $|\vec{U}| \text{ (m/s)}$, contours for Case10.

after 0.5 (ms) a stable reacting zone in the middle of the PCh is developed and the mixture above it is trapped and stayed unburned, while, still, a cold fuel jet is being injected into the MCh. Combustion is already initiated after 2.0 (ms) but an unburned fuels still can be seen after 5.0 (ms). However, it can be seen in figure 2.29 that after 0.5 (ms), the cold fuel jet is virtually vanished and a hot product jet is already developed and being injected into the MCh and combustion is completed after 5.0 (ms).

To further analyze the effects of the igniter location on the lean and ultra-lean premixed combustion processes, it is fixed at the same location as it in Case11 and the MCh equivalence ratio are changed to 0.3 and 0.2 in Case12 and Case13, respectively. The contours of temperature, fuel mass fraction, and velocity magnitude for these cases are shown in figures 2.30 and 2.31. The PCh ignition processes are, fairly, similar to them in Case11. It can be

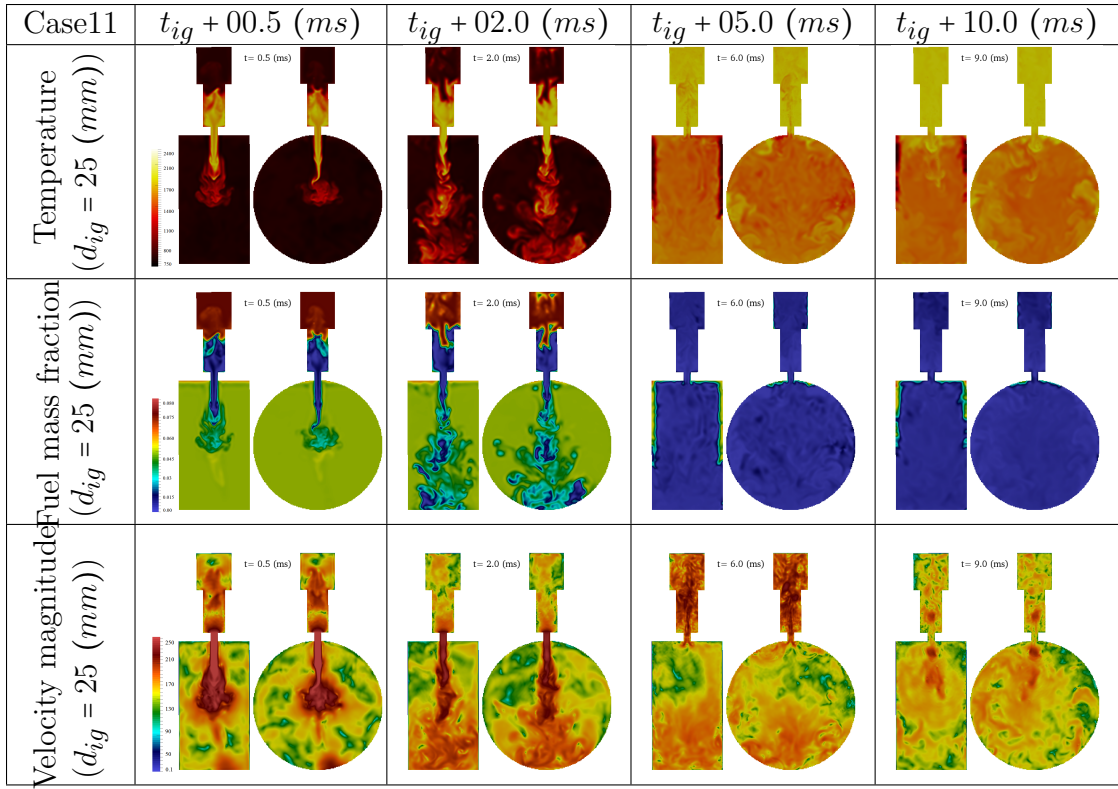


Figure 2.29: Temporal evolution of simulated temperature, T , fuel mass fraction, ϕ_{CH_4} , and velocity magnitude, $|\vec{U}|$ (m/s), contours for Case11.

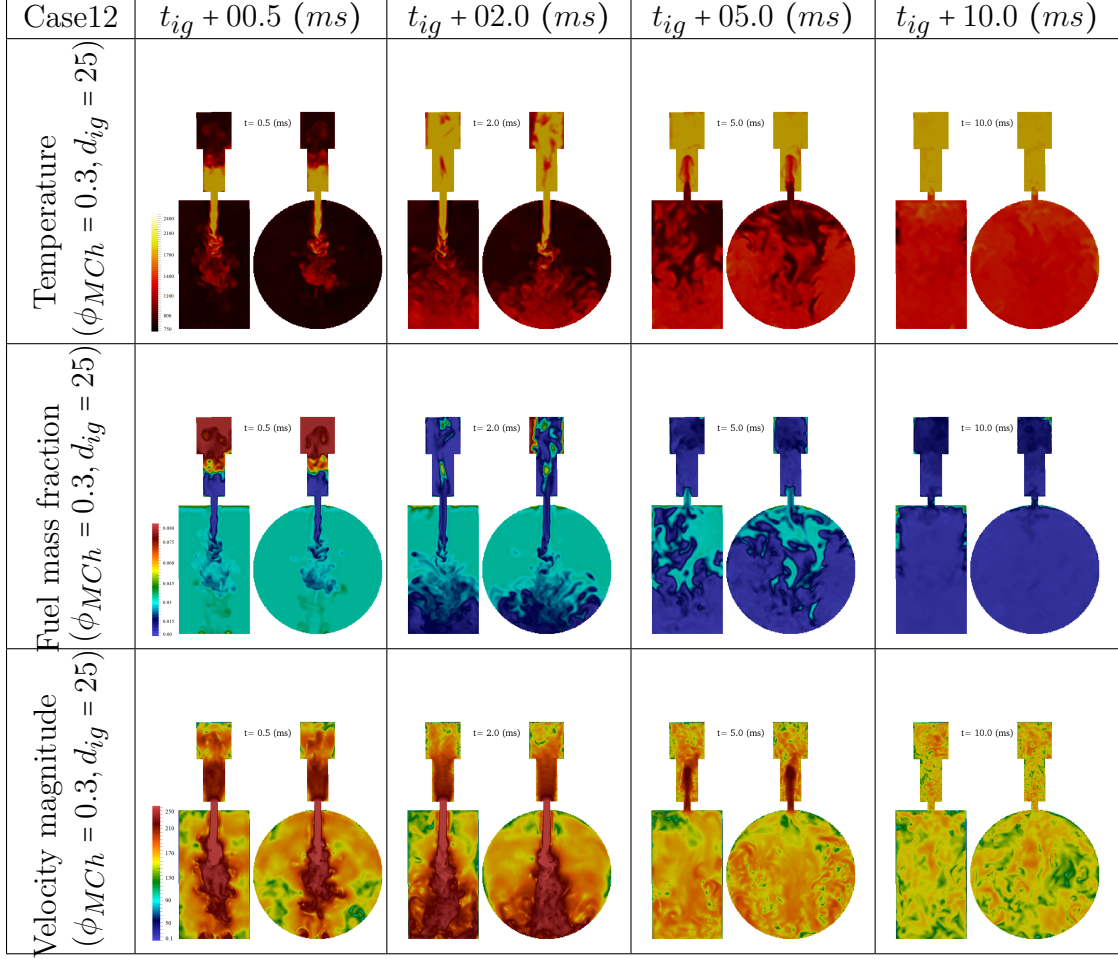


Figure 2.30: Temporal evolution of simulated temperature, T , fuel mass fraction, ϕ_{CH_4} , and velocity magnitude, $|\vec{U}|$ (m/s), contours for Case12.

seen in figure 2.30 that after 5 (ms) most of the MCh mixture is burned (compare to the results shown for Case8 in figure 2.25 after 5 (ms)). It also can be seen in figure 2.31 that the combustion of an ultra lean mixture is initiated and completed by 10 (ms).

The main difference in Case10 to Case13 is the location of the igniter and to evaluate its effects on the entire combustion process the results of these cases are analyzed together. In figure 2.32(a) the simulated pressure traces in Pch (dashed thin lines) and Mch (solid thick lines) versus time for Case10 (\square), Case11 (\circ), Case12 (\ast), and Case13 (\times) are shown. As it can be seen the MCh combustions are, generally, advanced. As it was shown

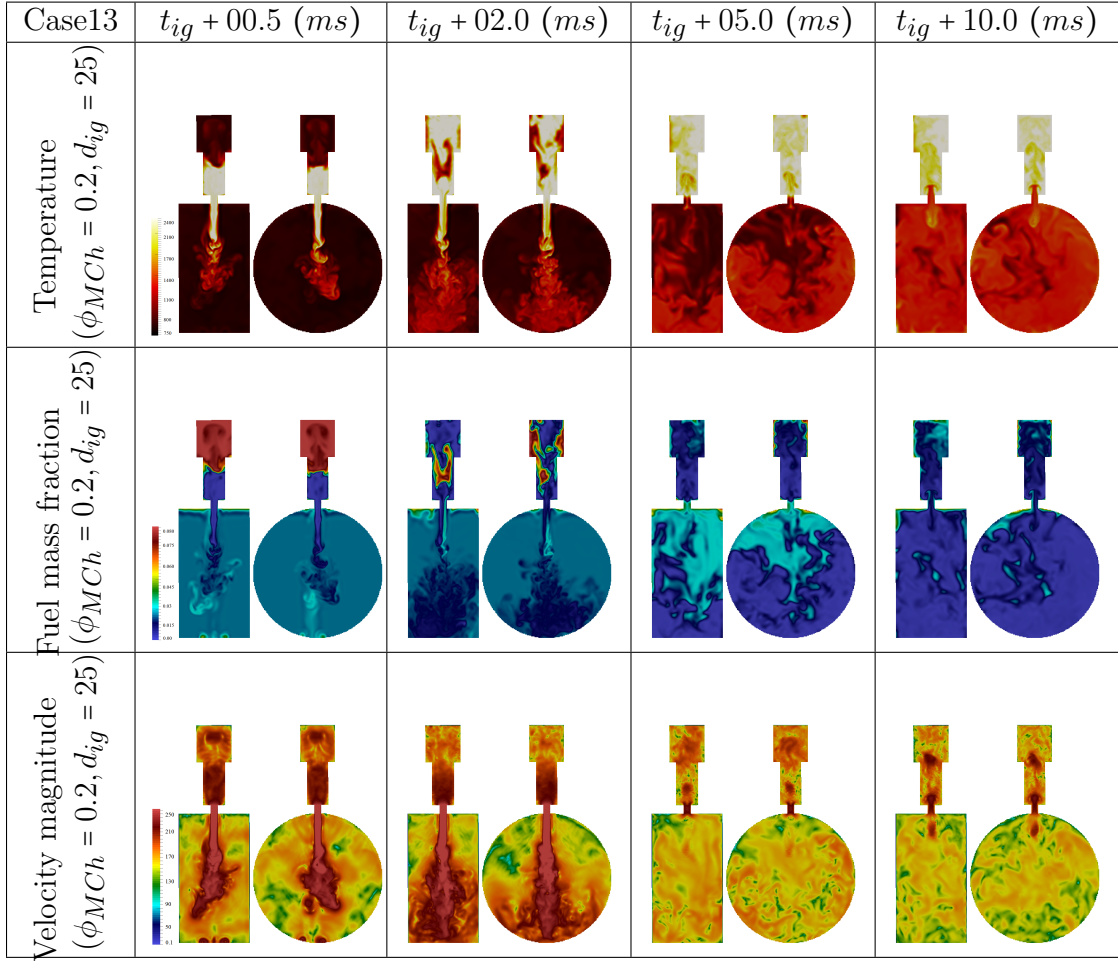


Figure 2.31: Temporal evolution of simulated temperature, T , fuel mass fraction, ϕ_{CH_4} , and velocity magnitude, $|\vec{U}|$ (m/s), contours for Case13.

for Case3 in figure 2.22(a), the combustion was completed within 10 (*ms*), while for the same thermo-chemical and hydrodynamics condition but lower igniter location in Case10 it is completed within 7 (*ms*). It can be observed in Case11 (the same conditions but lower igniter location close to the nozzle) that the main combustion duration can be decreased more to less than 5 (*ms*). The effect of the igniter location is investigated more in leaner and ultra-lean MCh compositions in Case12 and Case13, which combustion is initiated and completed in a short period of time. In figures 2.32(b)-(e) the simulated temperature (blue solid lines) and fuel mass fraction (red dashed lines) at a point in the nozzle exit in the MCh side versus time for Case10 to Case13 are presented which the streamwise velocity values are assigned to the temperature curves. It can be seen that in Case10 (figures 2.32b), still, for a shorter period of time a cold fuel jet is passing through the nozzle into the MCh, but, immediately after that a hot product jet is getting into the MCh and the MCh combustion is initiated and completed faster. It can be observed in figure 2.32(c) for Case11 that it is unlikely to develop a cold fuel jet since the premixed flame behaves as a barrier and traps the mixture at the upper section of the PCh. It can be seen that immediately after discharging the igniter energy a hot product jet is developed propagating into the MCh. Similar behavior can be seen in figures 2.32(d) and 2.32(e) but with lower final temperature since the MCh charge is lean and ultra-lean. Using this approach allows the ultra-lean combustion to burn nearly volumetric within a very short period of time.

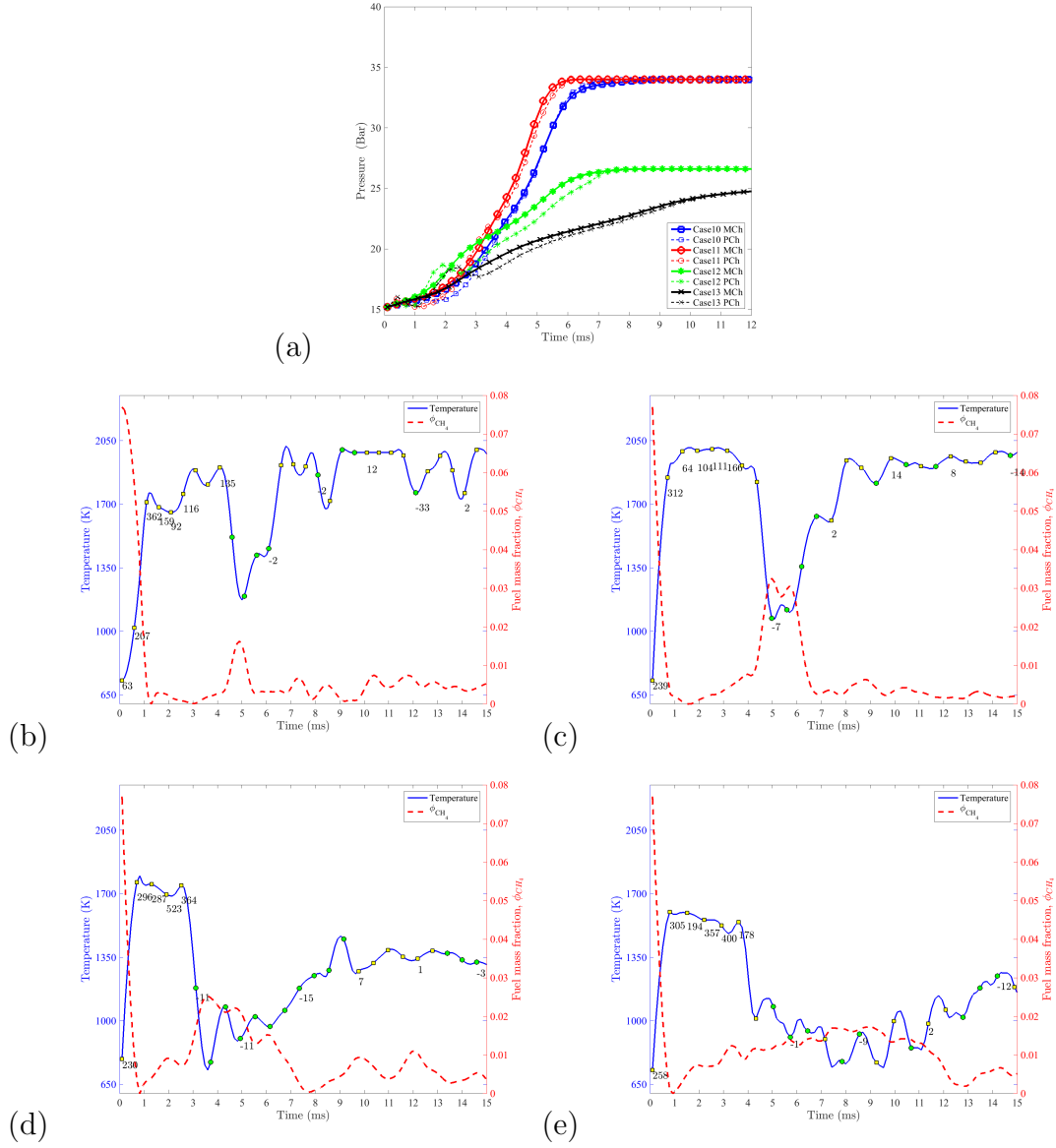


Figure 2.32: (a) Simulated pressure traces in Pch (dashed thin lines) and Mch (solid thick lines) versus time for Case10 (\square), Case11 (\circ), Case12 (\times), and Case13 (\times). (b)-(e) Simulated temperature (blue solid lines) and fuel mass fraction (red dashed lines) at a point in the nozzle exit in the MCh side versus time for Case10 to Case13. The streamwise velocity values are also shown.

2.6 Chapter conclusions

Turbulent jet ignition assisted rapid compression machines (TJI-assisted RCM) are simulated for various thermo-chemical and hydrodynamics conditions by large eddy simulation/ filtered mass density mass function (LES/FMDF) modeling approach using an immersed boundary (IB) method. The hybrid LES/FMDF equations for the compressible reacting flows which involves two sets of Eulerian and Lagrangian equations, are solved, conjointly, for velocity and scalar fields. The simulation results are in a good agreement with available experimental data, quantitatively and qualitatively. Three main combustion phases are delineated in a TJI-assisted RCM combustion system as i) cold fuel jet, ii) turbulent hot product/fuel jet, and iii) reverse fuel-air/product jet. As the results of a successful pre-chamber (PCh) ignition/combustion process, a turbulent hot product/fuel jet is being developed propagating into the main chamber (MCh) and initiating its combustion by providing hot ignition sites throughout the chamber. The MCh combustion initiation and duration features are dependent on the PCh and MCh initial thermo-chemical and hydrodynamics conditions, as well as the amount of heat transferring through the walls. Higher turbulence level inside the PCh leads to faster hot jet and shorter MCh combustion duration. In the process of PCh ignition, a jet of unburned fuel exits out to the MCh, which is an undesirable effect of locating the igniter far away from the nozzle. We suggested and studied a remedy to control and eliminate this jet by changing the location of the igniter. Igniting the PCh charge close to the nozzle prevents the unburned fuel getting out into the MCh, since the developed premixed flames inside the PCh act as barriers trapping the PCh charge in the upper side, which later they are, constantly and gradually, fed into the PCh combustion during the MCh combustion. Lowering the igniter location, which can be done experimen-

tally, causes the MCh charge getting exposed to a hot jet for a relatively longer time. This can decrease the low flammability limit of the premixed combustions and allow the fast and nearly volumetric combustion in ultra-lean premixed mixtures.

BIBLIOGRAPHY

BIBLIOGRAPHY

- [1] Institute for Cyber-Enabled Research (ICER) at Michigan State University. <http://icer.msu.edu/>.
- [2] Texas Advanced Computing Center (TACC) at the University of Texas at Austin. <http://www.tacc.utexas.edu>.
- [3] A. Afshari, F. Jaber, and T.P. Shih. Large-eddy simulations of turbulent flows in an axisymmetric dump combustor. *AIAA Journal*, 46(7), 2008.
- [4] D. Ahlman, G. Velter, G. Brethouwer, and A. Johansson. Direct numerical simulation of nonisothermal turbulent wall jets. *Physics of Fluids*, 21(3), 2009.
- [5] S. Ahmed and E. Mastorakos. Spark ignition of lifted turbulent jet flames. *Combustion and Flame*, 146(12):215 – 231, 2006.
- [6] A. Aldama. Filtering techniques for turbulent flow simulations. *Lecture Notes in Engineering, SpringerVerlag*, 49, 1990.
- [7] C. Arndt, R. Schiel, J. Gounder, W. Meier, and M. Aigner. Flame stabilization and auto-ignition of pulsed methane jets in a hot coflow: Influence of temperature. *Proceedings of the Combustion Institute*, 34(1):1483–1490, 2013.
- [8] W. Attard and H. Blaxill. A single fuel pre-chamber jet ignition powertrain achieving high load, high efficiency and near zero nox emissions. *SAE Int. J. Engines*, 5:734–746, 08 2011.
- [9] W. Attard and P. Parsons. Flame kernel development for a spark initiated pre-chamber combustion system capable of high load, high efficiency and near zero nox emissions. *SAE Int. J. Engines*, 3:408–427, 10 2010.
- [10] A. Banaeizadeh, A. Afshari, H. Schock, and F. Jaber. Large-eddy simulations of turbulent flows in internal combustion engines. *International Journal of Heat and Mass Transfer*, 60:781 – 796, 2013.
- [11] A. Banaeizadeh, Z. Li, and F. Jaber. Compressible scalar filtered mass density function model for high-speed turbulent flows. *AIAA Journal*, 49(10), 2011.

- [12] D. Beerer, V. McDonell, P. Therkelsen, and R. K. Cheng. Flashback and turbulent flame speed measurements in hydrogen/methane flames stabilized by a low-swirl injector at elevated pressures and temperature. *Journal of Engineering for Gas Turbines and Power*, 136:20242 – 20254, 2014.
- [13] L. Bezgin, V. Kopchenov, A. Sharipov, N. Titova, and A. Starik. Evaluation of prediction ability of detailed reaction mechanisms in the combustion performance in hydrogen/air supersonic flows. *Combustion Science and Technology*, 185(1):62–94, 2013.
- [14] M. Boger, D. Veynante, H. Boughanem, and A. Trouv. Direct numerical simulation analysis of flame surface density concept for large eddy simulation of turbulent premixed combustion. *Symposium (International) on Combustion*, 27(1):917 – 925, 1998.
- [15] P. Boivin, A. Dauplain, C. Jimnez, and B. Cuenot. Simulation of a supersonic hydrogen/air autoignition-stabilized flame using reduced chemistry. *Combustion and Flame*, 159(4):1779 – 1790, 2012.
- [16] J. Carpio, I. Iglesias, M. Vera, A. Snchez, and A. Lin. Critical radius for hot-jet ignition of hydrogen/air mixtures. *International Journal of Hydrogen Energy*, 38(7):3105 – 3109, 2013.
- [17] P. Clavin. Dynamic behavior of premixed flame fronts in laminar and turbulent flows. *Progress in Energy and Combustion Science*, 11(1):1 – 59, 1985.
- [18] P. Colucci, F. Jaberi, P. Givi, and S. Pope. Filtered density function for large eddy simulation of turbulent reacting flows. *Physics of Fluids*, 10(2):449–515, 1998.
- [19] B. Delarue and S. Pope. Application of pdf methods to compressible turbulent flows. *Physics of Fluids*, 9(9), 1997.
- [20] N. Djebaili, R. Lisbet, G. Dupre , and C. Patillard. Ignition of a combustible mixture by a hot unsteady gas jet. *Combustion Science and Technology*, 104:273–285, 1995.
- [21] L. F. Donovan and C. A. Todd. *Computer program for calculating isothermal turbulent jet mixing of two gases*, 1968.
- [22] S. Dorofeev, A.V. Bezmelnitsin, V.P. Sidorov, J.G. Yankin, and I.D. Matsukov. Turbulent jet initiation of detonation in hydrogen-air mixtures. *Shock Waves*, 6(2):73–78, 1996.

- [23] James F. Driscoll. Turbulent premixed combustion: Flamelet structure and its effect on turbulent burning velocities. *Progress in Energy and Combustion Science*, 34(1):91 – 134, 2008.
- [24] E. Fadlun, R. Verzicco, P. Orlandi, and J. Mohd-Yusof. Combined immersed-boundary finite-difference methods for three-dimensional complex flow simulations. *Journal of Computational Physics*, 161(1):35 – 60, 2000.
- [25] R. Fox. *Computational Models for Turbulent Reacting Flows*. Cambridge University Press, New York, 2003.
- [26] G. Gentz, B. Thelen, M. Gholamisheeri, P. Litke, A. Brown, J. Hoke, and E. Toulson. A study of the influence of orifice diameter on a turbulent jet ignition system through combustion visualization and performance characterization in a rapid compression machine. *Applied Thermal Engineering*, 81:399 – 411, 2015.
- [27] R. Ghias, R. Mittal, and H. Dong. A sharp interface immersed boundary method for compressible viscous flows. *Journal of Computational Physics*, 225(1):528 – 553, 2007.
- [28] A. Ghorbani, G. Steinhilber, D. Markus, and U. Maas. Ignition by transient hot turbulent jets: An investigation of ignition mechanisms by means of a pdf/redim method. *Proceedings of the Combustion Institute*, 35(2):2191 – 2198, 2015.
- [29] L. Gicquel, P. Givi, F. Jaber, and S. Pope. Velocity filtered density function for large eddy simulation of turbulent flows. *Physics of Fluids*, 14(3):1196–1213, 2002.
- [30] O. Gicquel, N. Darabiha, and D. Thvenin. Liminar premixed hydrogen/air counter-flow flame simulations using flame prolongation of {ILDm} with differential diffusion. *Proceedings of the Combustion Institute*, 28(2):1901 – 1908, 2000.
- [31] P. Givi. Filtered density function for subgrid scale modeling of turbulent combustion. *AIAA Journal*, 44(1):16–23, 2006.
- [32] S.V. Gordeyev and F. O. Thomas. Coherent structure in the turbulent planar jet. part 1. extraction of proper orthogonal decomposition eigenmodes and their self-similarity. *Journal of Fluid Mechanics*, 414:145 – 194, 2000.
- [33] R. Griffiths, J. Chen, H. Kolla, R. Cant, and W. Kollmann. Three-dimensional topology of turbulent premixed flame interaction. *Proceedings of the Combustion Institute*, 35(2):1341 – 1348, 2015.

- [34] P. Grogan, S. Goldsborough, and M. Ihme. Ignition regimes in rapid compression machines. *Combustion and Flame*, 162(8):3071 – 3080, 2015.
- [35] H. Gunnar. Hot-wire measurements in a plane turbulent jet. *Journal of Applied Mechanics*, 32(4):721–734, 1965.
- [36] D. Hensinger, J. Maxson, K. Hom, and A. Oppenheim. Jet plume injection and combustion. In *SAE Technical Paper*. SAE International, 02 1992.
- [37] G. Heskestad. Hot-wire measurements in a plane turbulent jet1. *Journal of Applied Mechanics*, 32:721–734, 1965.
- [38] J. Hinze. *Turbulence*. McGraw-Hill, New York, 1975.
- [39] I. Iglesias, M. Vera, A. L. Sanchez, and A. Linan. Numerical analyses of deflagration initiation by a hot jet. *Combustion Theory and Modelling*, 16(6):994–1010, 2012.
- [40] F. Jaber. Temperature fluctuations in particle-laden homogeneous turbulent flows. *International Journal of Heat and Mass Transfer*, 41(24):4081 – 4093, 1998.
- [41] F. Jaber, P. Colucci, S. James, P. Givi, and S. Pope. Filtered mass density function for large eddy simulation of turbulent reacting flows. *Journal of Fluid Mechanics*, 40(1):85–121, 1999.
- [42] F. Jaber, D. Livescu, and C. Madnia. Characteristics of chemically reacting compressible homogeneous turbulence. *Physics of Fluids*, 12(5), 2000.
- [43] F. Jaber and C. Madnia. Effects of heat of reaction on homogeneous compressible turbulence. *Journal of Scientific Computing*, 13(2):201–228, 1998.
- [44] F. Jaber, R.S. Miller, F. Mashayek, and P. Givi. Differential diffusion in binary scalar mixing and reaction. *Combustion and Flame*, 109(4):561 – 577, 1997.
- [45] S. James and F. Jaber. Large scale simulations of two-dimensional nonpremixed methane jet flames. *Combustion and Flame*, 123(4):465 – 487, 2000.
- [46] T. Jin, K. Luo, S. Lu, and J. Fan. DNS investigation on flame structure and scalar dissipation of a supersonic lifted hydrogen jet flame in heated coflow. *International Journal of Hydrogen Energy*, 38(23):9886 – 9896, 2013.

- [47] Y. Ju and T. Niioka. Reduced kinetic mechanism of ignition for nonpremixed hydrogen/air in a supersonic mixing layer. *Combustion and Flame*, 99:240–246, 1994.
- [48] S. Kang, G. Iaccarino, F. Ham, and P. Moin. Prediction of wall-pressure fluctuation in turbulent flows with an immersed boundary method. *Journal of Computational Physics*, 228(18):6753 – 6772, 2009.
- [49] R. Kee, F. Rupley, and J. Miller. *Chemkin-II: A Fortran chemical kinetics package for the analysis of gas-phase chemical kinetics*. Sep 1989.
- [50] C. Kennedy, M. Carpenter, and R. Lewis. Low-storage, explicit rungekutta schemes for the compressible navierstokes equations. *Applied Numerical Mathematics*, 35(3):177 – 219, 2000.
- [51] A. Kerstein. Linear-eddy modeling of turbulent transport. part 4. structure of diffusion flames. *Combustion Science and Technology*, 81(1-3):75–96, 1992.
- [52] A.Y. Klimenko and R.W. Bilger. Conditional moment closure for turbulent combustion. *Progress in Energy and Combustion Science*, 25(6):595 – 687, 1999.
- [53] N. E. Kotsovinos. A note on the spreading rate and virtual origin of a plane turbulent jet. *Journal of Fluid Mechanics*, 77:305 – 311, 1976.
- [54] G. Lacaze, E. Richardson, and T. Poinso. Large eddy simulation of spark ignition in a turbulent methane jet. *Combustion and Flame*, 156(10):1993 – 2009, 2009.
- [55] D. Lee and K. Huh. DNS analysis of propagation speed and conditional statistics of turbulent premixed flame in a planar impinging jet. *Proceedings of the Combustion Institute*, 33(1):1301 – 1307, 2011.
- [56] S. Leicher, W. Fritz, J. Grashof, and J. Longo. *Eighth International Conference on Numerical Methods in Fluid Dynamics: Proceedings of the Conference, Rheinisch-Westfälische Technische Hochschule Aachen, Germany, June 28 – July 2, 1982*, chapter Mesh generation strategies for CFD on complex configurations, pages 329–334. Springer Berlin Heidelberg, Berlin, Heidelberg, 1982.
- [57] S. Lele. Compact finite difference schemes with spectral-like resolution. *Journal of Computational Physics*, 103(1):16 – 42, 1992.
- [58] Z. Li, A. Banaeizadeh, S. Rezaeiravesh, and F. Jaber. Advanced modeling of high speed turbulent reacting flows. *50th AIAA Aerospace Sciences Meeting*, 2012.

- [59] Y. Lin, P. Jansohn, and K. Boulouchos. Turbulent flame speed for hydrogen-rich fuel gases at gas turbine relevant conditions. *International Journal of Hydrogen Energy*, 39(35):20242 – 20254, 2014.
- [60] A. Lipatnikov and J. Chomiak. Effects of premixed flames on turbulence and turbulent scalar transport. *Progress in Energy and Combustion Science*, 36(1):1 – 102, 2010.
- [61] A. Lipatnikov, J. Chomiak, V. Sabelnikov, S. Nishiki, and T. Hasegawa. Unburned mixture fingers in premixed turbulent flames. *Proceedings of the Combustion Institute*, 35(2):1401 – 1408, 2015.
- [62] Q. Liu and O. Vasilyev. A brinkman penalization method for compressible flows in complex geometries. *Journal of Computational Physics*, 227(2):946 – 966, 2007.
- [63] G. Lodier, C. Merlin, P. Domingo, L. Vervisch, and F. Ravet. Self-ignition scenarios after rapid compression of a turbulent mixture weakly-stratified in temperature. *Combustion and Flame*, 159(11):3358 – 3371, 2012.
- [64] S. Lu, J. Fan, and K. Luo. High-fidelity resolution of the characteristic structures of a supersonic hydrogen jet flame with heated co-flow air. *International Journal of Hydrogen Energy*, 37(4):3528 – 3539, 2012.
- [65] J. Maxson, D. Hensinger, K. Hom, and A. Oppenheim. Performance of multiple stream pulsed jet combustion systems. In *SAE Technical Paper*. SAE International, 02 1991.
- [66] G. Mittal, M. Raju, and C. Sung. CFD modeling of two-stage ignition in a rapid compression machine: Assessment of zero-dimensional approach. *Combustion and Flame*, 157(7):1316 – 1324, 2010.
- [67] R. Mittal and G. Iaccarino. Immersed boundary methods. *Annual Review of Fluid Mechanics*, 37(1):239–261, 2005.
- [68] E. Murase, S. Ono, K. Hanada, and Antoni K. Oppenheim. Pulsed combustion jet ignition in lean mixtures. In *SAE Technical Paper*. SAE International, 10 1994.
- [69] H. Najm, P. Paul, C. Mueller, and P. Wyckoff. On the adequacy of certain experimental observables as measurements of flame burning rate. *Combustion and Flame*, 113(3):312 – 332, 1998.
- [70] M. Nik, S. Yilmaz, M. Sheikhi, P. Givi, and S. Pope. Simulation of sandia flame d using velocity-scalar filtered density function. *AIAA Journal*, 48(7):1513–1522, 2010.

- [71] Z. Nikolaou and N. Swaminathan. Heat release rate markers for premixed combustion. *Combustion and Flame*, 161(12):3073 – 3084, 2014.
- [72] E. Oran and J. Boris. *Numerical Simulation of Reactive Flows*. Cambridge University Press, New York, 2001.
- [73] J. Park, K. Kwon, and H. Choi. Numerical solutions of flow past a circular cylinder at reynolds numbers up to 160. *KSME International Journal*, 12(6):1200–1205, 1998.
- [74] M. Pathak, A. Dewan, and A. Dass. Computational prediction of a slightly heated turbulent rectangular jet discharged into a narrow channel crossflow using two different turbulence models. *International Journal of Heat and Mass Transfer*, 49(2122):3914 – 3928, 2006.
- [75] P. Paul and H. Najm. Planar laser-induced fluorescence imaging of flame heat release rate. *Symposium (International) on Combustion*, 27(1):43 – 50, 1998.
- [76] C. Peskin. The fluid dynamics of heart valves: Experimental, theoretical, and computational methods. *Annual Review of Fluid Mechanics*, 14(1):235–259, 1982.
- [77] N. Peters. Laminar diffusion flamelet models in non-premixed turbulent combustion. *Progress in Energy and Combustion Science*, 10(3):319 – 339, 1984.
- [78] N. Peters. Twenty-first symposium (international on combustion) laminar flamelet concepts in turbulent combustion. *Symposium (International) on Combustion*, 21(1):1231 – 1250, 1988.
- [79] N. Peters. *Turbulent Combustion*. Cambridge University Press, New York, 2000.
- [80] H. Phillips. Ignition in a transient turbulent jet of hot inert gas. *Combustion and Flame*, 19(2):187 – 195, 1972.
- [81] C. Pierce and P. Moin. Progress-variable approach for large-eddy simulation of non-premixed turbulent combustion. *Journal of Fluid Mechanics*, 504:73–97, 4 2004.
- [82] H. Pitsch, O. Desjardins, G. Balarac, and M. Ihme. Large-eddy simulation of turbulent reacting flows. *Progress in Aerospace Sciences*, 44(6):466 – 478, 2008.
- [83] W. Pitts. Importance of isothermal mixing processes to the understanding of lift-off and blowout of turbulent jet diffusion flames. *Combustion and Flame*, 76(2):197 – 212, 1989.

- [84] T. Poinso and S. Lele. Boundary conditions for direct simulations of compressible viscous flows. *Journal of Computational Physics*, 101(1):104 – 129, 1992.
- [85] T. Poinso and D. Veynante. *Theoretical and Numerical Combustion*. R. T. Edwards, Philadelphia, 2001.
- [86] S. Pope. Calculations of a plane turbulent jet. *AIAA Journal*, 22(7), 1983.
- [87] S. Pope. Pdf methods for turbulent reactive flows. *Progress in Energy and Combustion Science*, 11(2):119 – 192, 1985.
- [88] S. Pope. Turbulent premixed flames. *Annual Review of Fluid Mechanics*, 19:237–270, 1987.
- [89] S. Pope. *Turbulent Flows*. Cambridge University Press, New York, 2000.
- [90] W. Qin, M. Xie, M. Jia, T. Wang, and D. Liu. Large eddy simulation of in-cylinder turbulent flows in a DISI gasoline engine. *Applied Mathematical Modelling*, 38(24):5967 – 5985, 2014.
- [91] J. Rehm and N. Clemens. The relationship between vorticity/strain and reaction zone structure in turbulent non-premixed jet flames. *Symposium (International) on Combustion*, 27(1):1113 – 1120, 1998.
- [92] D. Rowinski and S. Pope. An investigation of mixing in a three-stream turbulent jet. *Physics of Fluids (1994-present)*, 25(10):–, 2013.
- [93] C.J. Rutland and A. Trouv. Direct simulations of premixed turbulent flames with nonunity lewis numbers. *Combustion and Flame*, 94(12):41 – 57, 1993.
- [94] R. Sadanandan, D. Markus, R. Schiel, U. Maas, J. Olofsson, H. Seyfried, M. Richter, and M. Aldn. Detailed investigation of ignition by hot gas jets. *Proceedings of the Combustion Institute*, 31(1):719 – 726, 2007.
- [95] S. Schlatter, B. Schneider, Y. Wright, and K. Boulouchos. Comparative study of ignition systems for lean burn gas engines in an optically accessible rapid compression expansion machine. In *SAE Technical Paper*. SAE International, 09 2013.
- [96] C. Schneider, W. Rasband, and K. Eliceiri. Nih image to imagej: 25 years of image analysis. *Nature Methods*, 9(7):671 – 675, 2012.

- [97] Jerry Seitzman and Timothy Lieuwen. Turbulent flame propagation characteristics of high hydrogen content fuels.
- [98] M. Sheikhi, T. Drozda, P. Givi, F. Jaber, and S. Pope. Large eddy simulation of a turbulent nonpremixed piloted methane jet flame (sandia flame d). *Proceedings of the Combustion Institute*, 30(1):249–556, 2005.
- [99] M. Sheikhi, P. Givi, and S. Pope. Velocity-scalar filtered mass density function for large eddy simulation of turbulent flows. *Physics of Fluids*, 19(9):95–106, 2007.
- [100] M. Sheikhi, P. Givi, and S. Pope. Frequency-velocity-scalar filtered mass density function for large eddy simulation of turbulent flows. *Physics of Fluids*, 21(7):75–102, 2009.
- [101] N. Soulopoulos, Y. Hardalupas, and A. M. K. P. Taylor. Mixing and scalar dissipation rate statistics in a starting gas jet. *Physics of Fluids*, 27(12), 2015.
- [102] G. Stahl and J. Warnatz. Numerical investigation of time-dependent properties and extinction of strained methane and propane-air flamelets. *Combustion and Flame*, 85:285–299, 06 1991.
- [103] C. Steinberger, T. Vidoni, and P. Givi. The compositional structure and the effects of exothermicity in a nonpremixed planar jet flame. *Combustion and Flame*, 94(3):217 – 232, 1993.
- [104] C. Sung and H. Curran. Using rapid compression machines for chemical kinetics studies. *Progress in Energy and Combustion Science*, 44:1 – 18, 2014.
- [105] E. Toulson, H. Schock, and W. Attard. A review of pre-chamber initiated jet ignition combustion systems. In *SAE Technical Paper*. SAE International, 10 2010.
- [106] Y. Tseng and J. Ferziger. A ghost-cell immersed boundary method for flow in complex geometry. *Journal of Computational Physics*, 192(2):593 – 623, 2003.
- [107] M. Turkish. 3 - valve stratified charge engines: Evolvement, analysis and progression. In *SAE Technical Paper*. SAE International, 02 1974.
- [108] C. Vagelopoulos, F. Egolfopoulos, and C. Law. Further considerations on the determination of laminar flame speeds with the counterflow twin-flame technique. *Symposium (International) on Combustion*, 25(1):1341 – 1347, 1994.

- [109] A. Validi. *High Fidelity simulations of Turbulent Jet Ignition and Combustion*. PhD thesis, Michigan State University, 2016.
- [110] A. Validi, H. Schock, E. Toulson, and F. Jaber. LES/FMDF of turbulent jet ignition in a rapid compression machine. *Bulletin of the American Physical Society*, 60, 2015.
- [111] H. Wang, K. Luo, S. Lu, and J. Fan. Direct numerical simulation and analysis of a hydrogen/air swirling premixed flame in a micro combustor. *International Journal of Hydrogen Energy*, 36(21):13838 – 13849, 2011.
- [112] J. Wang, S. Yu, M. Zhang, W. Jin, Z. Huang, S. Chen, and H. Kobayashi. Burning velocity and statistical flame front structure of turbulent premixed flames at high pressure up to 1.0 {MPa}. *Experimental Thermal and Fluid Science*, 68:196 – 204, 2015.
- [113] K. Wassim, Kamel Abderrazak, Hatem Mhiri, Georges Le Palec, and Philippe Bournot. A numerical study of non-isothermal turbulent coaxial jets. *Heat and Mass Transfer*, 44(9):1051–1063, 2007.
- [114] J. Westerweel, A. Petracci, R. Delfos, and J. Hunt. Characteristics of the turbulent/non-turbulent interface of a non-isothermal jet. *Philosophical Transactions of the Royal Society of London A: Mathematical, Physical and Engineering Sciences*, 369(1937):723–737, 2011.
- [115] F. Williams. *Combustion Theory*. Benjamin/Cummings, Menlo Park, CA, 1985.
- [116] M. Yaldizli, K. Mehravaran, H. Mohammad, and F. Jaber. The structure of partially premixed methane flames in high-intensity turbulent flows. *Combustion and Flame*, 154(4):692 – 714, 2008.
- [117] T. Ye, R. Mittal, H. Udaykumar, and W. Shyy. An accurate cartesian grid method for viscous incompressible flows with complex immersed boundaries. *Journal of Computational Physics*, 156(2):209 – 240, 1999.
- [118] S. Yilmaz, M. Nik, P. Givi, and P. Strakey. Scalar filtered density function for large eddy simulation of a bunsen burner. *Journal of Propulsion and Power*, 26(1):84–93, 2010.
- [119] M. Zabetakis. Flammability characteristics of combustible gases and vapors. *U.S. Bureau of Mines. Bulletin 627*, 1965.